Spatial transcriptomics reveals microglial mechanisms driving amyloid-β clearance in immunized Alzheimer's disease patients

Lynn van Olst[1,2], Brooke Simonton[1,2], Alex J Edwards[1,2], Anne V Forsyth[1,2], Jake Boles[1,2], Pouya Jamshidi[3], Thomas Watson[1,2], Nate Shepard[2], Talia Krainc[2], Benney MR Argue[1,2], Ziyang Zhang[1,2], Joshua Kuruvilla[1,2], Lily Camp[1,2], Mengwei Li[4], Hang Xu[4], Jeanette L Norman[5], Joshua Cahan[1,2], Robert Vassar[2,6], Jinmiao Chen[4], Rudolph J Castellani[3], James AR Nicoll[5], Delphine Boche[5] and *David Gate[1,2]

[1]Abrams Research Center on Neurogenomics, Northwestern University Feinberg School of Medicine, Chicago, IL, USA.

[2]The Ken & Ruth Davee Department of Neurology, Northwestern University Feinberg School of Medicine, Chicago, IL, USA.

[3]Department of Pathology, Northwestern University Feinberg School of Medicine, Chicago, IL, USA.

[4]Singapore Immunology Network (SIgN), Agency for Science, Technology and Research (A*STAR), Singapore.

[5]Clinical Neurosciences, School of Clinical and Experimental Sciences School, Faculty of Medicine, University of Southampton, Southampton, UK.

[6]Mesulam Center for Cognitive Neurology and Alzheimer's Disease, Northwestern University Feinberg School of Medicine, Chicago, IL, USA.

*Correspondence to: dgate@northwestern.edu

Abstract

Alzheimer's disease (AD) therapies utilizing amyloid-β (Aβ) immunization have shown potential in clinical trials. Yet, the underlying mechanisms driving Aβ clearance in the immunized AD brain remain unclear. Here, we employ spatial transcriptomics (ST) to explore the effects of both active and passive Aβ immunization on the AD brain. Comparing actively immunized AD patients with non-immunized AD subjects and neurologically healthy controls, we identify distinct microglial states associated with Aβ clearance. Using high-resolution ST alongside single-cell RNA sequencing (scRNA-seq), we delve deeper into the transcriptional pathways involved in Aβ removal following treatment with lecanemab, uncovering spatially distinct microglial responses that vary by brain region. Our analysis reveals upregulation of *Triggering Receptor Expressed On Myeloid Cells 2* (*TREM2*) and *Apolipoprotein E* (*APOE*) in microglia across both active and passive immunization approaches, which correlate positively with Aβ clearance. These findings provide novel insights into the transcriptional mechanisms orchestrating Aβ clearance and shed light on the role of microglia in immune-mediated clearance. Importantly, our work uncovers potential molecular targets that could enhance Aβ-targeted immunotherapies, offering new avenues for developing more effective therapeutic strategies to combat AD. This study paves the way for future research into microglial modulation and its therapeutic potential in AD.

36 **Introduction**

37 For nearly three decades, clinical trials have focused on targeting Aβ accumulation in the Alzheimer's
38 disease (AD) brain[1]. One strategy has been an immunotherapeutic approach that uses immunization against
39 Aβ. The AN1792 clinical trial, conducted from 2000 to 2002, was the first immunotherapeutic approach in which
40 AD patients received active immunization against the synthetic $A\beta_{1-42}$ peptide[2]. The AN1792 trial was based on
41 extensive preclinical evidence showing that immunization against the $A\beta_{1-42}$ peptide could prevent or reverse
42 key AD neuropathological features in mouse models of cerebral amyloidosis[3-6]. However, the AN1792 trial was
43 suspended after a small number of treated patients developed aseptic meningoencephalitis[7-9], characterized
44 by inflammation related to cerebral amyloid angiopathy (CAA)[10, 11]. Notably, our post-mortem analyses of brains
45 of patients from the AN1792 trial demonstrated Aβ clearance in some immunized patients[2, 10, 12, 13]. Aβ has been
46 detected within microglia, likely through phagocytosis. However, the cellular mechanisms responsible for Aβ
47 clearance in the brains of AN1792-immunized patients remain unknown[10, 13, 14].

48 The inflammatory side effects observed in the AN1792 trial led to a shift in Aβ immunotherapy strategies
49 toward passive immunization. In this approach, AD patients are treated with antibodies targeting various Aβ
50 species. One such antibody, lecanemab, specifically binds to large, soluble Aβ protofibrils[15]. In clinical trials,
51 lecanemab reduced markers of Aβ in early AD and resulted in moderately less decline on measures of cognition
52 and function than placebo[16]. We recently described a case study in which a 65-year-old woman who received
53 three doses of lecanemab died after being treated with tissue plasminogen activator for acute stroke-like
54 symptoms[17]. Intriguingly, this patient's brain autopsy revealed inflammation in blood vessels with CAA[17]. Further
55 examination of this patient's brain also showed evidence of phagocytes clearing vascular Aβ as well as
56 parenchymal Aβ in select brain regions[18].

57 In this study, we utilized spatial transcriptomics (ST) to examine the neuroimmune response in the AD
58 brain following Aβ immunization. We compared AN1792 actively immunized AD (iAD) brains to non-immunized
59 AD (nAD) brains and non-neurologic disease (NND) control brains. Furthermore, in the patient treated with
60 lecanemab, we employed high-definition ST, spatial proteogenomics and single-cell RNA sequencing
61 (scRNAseq) to investigate the immune response to Aβ following passive immunization. Our analysis reveals a
62 transcriptomic microglial response to Aβ shared between actively and passively immunized AD patient brains.
63 This response is defined by upregulated expression of *Apolipoprotein E (APOE)* and *Triggering Receptor*

64 *Expressed On Myeloid Cells 2 (TREM2)*. Altogether, our work highlights several candidate genes to modulate
65 the microglial response to Aβ following Aβ immunotherapy.
66
67 **Results**
68 **Active Aβ immunization drives a microglial response to Aβ**
69 We first utilized ST (10x Genomics Visium) to analyze brain frontal cortex sections of AD patients from
70 the AN1792 trial (**Fig. 1a**). This cohort included 13 iAD brains, as well as 6 nAD and 6 NND control brains (**Fig.**
71 **1b**). The clinical and pathologic profiles of these subjects are detailed in **Extended Data Table 1**. Groups were
72 age- (**Fig. 1c)** and sex-matched (**Extended Data Fig. 1a**). We manually annotated ST spots according to their
73 location within cortical layers, meninges, or white matter using hematoxylin and eosin staining (**Fig. 1d** and
74 **Extended Data Fig. 1b**). We then utilized a pseudobulk method (DESeq2) to identify differentially expressed
75 genes (DEGs) per cortical layer (**Extended Data Fig. 1c and Extended Data Table 2**). Importantly, we did not
76 detect significant differences in the number of ST spots per region or number of features per region (**Extended**
77 **Data Fig. 1b-c**). Only cortical layer I of iAD samples showed a significantly lower percentage of mitochondrial
78 gene expression (**Extended Data Fig. 1d**), potentially reflecting alterations in mitochondrial metabolism. We
79 also validated our manual annotations by spatially plotting the expression of meningeal, white matter, and layer-
80 specific gray matter genes. (**Extended Data Fig. 1e**). Interestingly, we found that deeper cortical layers
81 contained the most DEGs when comparing nAD to NND controls, while superficial layers were predominantly
82 affected in iAD compared to NND controls (**Fig. 1e** and **Extended Data Table 2**). Cortical layer III had a high
83 number of DEGs comparing iAD to nAD and contained the most DEGs comparing nAD to NND controls (**Fig.**
84 **1e**). This high level of genomic dysregulation led us to further examine this cortical layer. Remarkably, nearly
85 all cortical layer III DEGs were unique to either iAD or nAD when compared to NND controls, with only 7.1% of
86 DEGs shared between groups (**Fig. 1f** and **Extended Data Table 2**). Altogether, these results indicate
87 transcriptomic alterations in the actively immunized AD cortex.
88 Notably, *APOE* and *TREM2* were among the genes upregulated in cortical layer III of the iAD cortex
89 compared to nAD controls (**Fig. 1g-h** and **Extended Data Table 2**). *APOE*[19, 20] and *TREM2*[21, 22] are both
90 established genetic risk factors for AD. Moreover, both genes are associated with the microglial response to
91 Aβ[23-26]. Additional cortical layer III genes upregulated in iAD vs. nAD are those involved in inflammation and

92 lysosomal function, such as *Alpha-2-Macroglobulin* (*A2M*) and *Caveolae Associated Protein 1* (*CAVIN1*). In
93 contrast, genes downregulated in iAD compared to nAD controls included genes encoding heat-shock proteins
94 (HSPs), such as *Heat Shock Protein Family A (Hsp70) Member 1A* (*HSPA1A*) and *Heat Shock Protein Family*
95 *H (Hsp110) Member 1* (*HSPH1*) (**Fig. 1g-h** and **Extended Data Table 2**). HSPs are involved in protein folding[27]
96 and their expression can be indicative of cellular stress[27, 28]. When comparing nAD to NND controls in cortical
97 layer III, we observed increased expression of several heat-shock proteins (HSPs) that have been previously
98 implicated in AD (**Fig. 1h**, **Extended Data Fig. 1f** and **Extended Data Table 2**). Finally, we examined the most
99 divergent DEGs between iAD vs. nAD and nAD vs. NND comparisons to identify genes most altered by
100 immunization (**Extended Data Fig. 1g** and **Extended Data Table 2**). Among the top 10 divergent DEGs,
101 several genes upregulated in nAD but significantly downregulated after immunization encoded HSPs (*HSPA1B*,
102 *DNAJB1*). Conversely, genes downregulated in nAD but upregulated in iAD were involved in synaptic plasticity,
103 including *Semaphorin 3G* (*SEMA3G*) and *Hes Family BHLH Transcription Factor 5* (*HES5*). Both SEMAG3[29]
104 and HES5[29] have been shown to be decreased in the cerebrospinal fluid of AD patients. Additionally, *C-Type*
105 *Lectin Domain Family 3 Member B* (*CLEC3B*) was upregulated in iAD but downregulated in nAD. Decreased
106 expression of CLEC3B has been suggested as a biomarker for neurologic diseases[30, 31], and a missense variant
107 of this gene has been associated with longevity[32, 33]. Altogether, these results indicate distinct transcriptomic
108 alterations in cortical layer III of iAD brains, characterized by a decrease in genes involved in protein folding
109 and cellular stress, alongside an increase in AD-associated immune response genes, such as *APOE* and
110 *TREM2*.

111 We previously demonstrated Aβ clearance in a subset of AN1792 subjects[2, 10, 12, 13]. To investigate
112 mechanisms distinguishing AN1792 subjects with and without extensive Aβ clearance, we quantified Aβ
113 pathology on sequential slides to the ST tissue using immunohistochemistry (IHC). For this purpose, a pan-Aβ
114 antibody (D54D2) was used to stain tissue sections for Aβ (**Fig. 1i** and **Extended Data Fig. 1h**). Aβ clearance
115 was most prominent in the superficial layers of the cortex (**Extended Data Fig. 1i**), consistent with our previous
116 findings[10]. Based on the amount Aβ deposits (**Fig. 1j**), we categorized the iAD cohort into two groups: those
117 with limited Aβ clearance (iAD-lim, *N*=6) and those with extensive Aβ clearance (iAD-ext, *N*=7) (**Fig. 1k**). We
118 also quantified phosphorylated tau (pTau) by measuring AT8 load in the gray matter across these groups, but
119 found no significant differences (**Extended Data Fig. 1j-k**). This finding is in unison with our prior results

120 showing that tau pathology persisted in iAD brains even in cortical areas cleared of Aβ[12]. Next, we overlaid Aβ
121 IHC from consecutive slides (separated by 5-10 μm) with our ST data. Given that the average Aβ plaque
122 occupies 250-350 μm[2(34)], we assumed minimal variance in Aβ plaque environments between consecutive
123 tissue sections. To capture transcriptomic alterations around Aβ deposits, we extended the binary Aβ signal by
124 100 μm beyond its actual size, with a gradual decrease in signal intensity every 20 μm (**Fig. 1l**). This approach
125 enabled the direct examination of the Aβ niche (Aβ density), and evaluation of genes associated with this niche
126 (**Fig. 1l**). Note that vascular Aβ–rich ST spots were excluded from the following analyses.

127 We investigated transcriptomic alterations occurring at the Aβ niche by performing differential
128 expression analysis on Aβ-rich ST spots in the gray matter, utilizing model-based analysis of single-cell
129 transcriptomics[35] (MAST), to leverage the full resolution of the ST data. To account for sample variability, we
130 included a random effect and incorporated covariates such as the fraction of genes detected per ST spot, sex,
131 age, and genomic DNA percentage, as justified in the methods. Our analysis revealed increased expression of
132 *APOE* and *Myristoylated Alanine-Rich C-Kinase Substrate* (*MARCKS)* (**Fig. 1m** and **Extended Data Table 2**).
133 *MARCKS* is expressed in activated microglia that surround Aβ plaques[36]. Interestingly, the most upregulated
134 gene at the Aβ niche was *Family With Sequence Similarity 107 Member A* (*FAM107A*)—a stress-responsive
135 actin-bundling factor that influences synaptic efficiency and cognition[37]. We then compared the Aβ niche
136 between iAD-lim and extensive iAD-ext brains. In subjects with more residual Aβ pathology, inflammatory genes
137 such as *Beta-2-Microglobulin* (*B2M*), *A2M*, *CD74 Molecule* (*CD74*), *APOE* and *MARCKS*, were upregulated,
138 while these genes were not elevated in iAD-ext subjects (**Fig. 1n** and **Extended Data Table 2**). Pathway
139 analyses using the Molecular Signatures Database (MSigDB) revealed enrichment of interferon-alpha
140 response and IL-2/STAT5 signaling based on unique DEGs in the iAD-lim Aβ niche (**Extended Data Fig. 1l**
141 and **Extended Data Table 2**). Collectively, genes altered in Aβ-rich spots highlight a more pronounced
142 inflammatory signature within the Aβ niche of iAD-lim vs. iAD-ext.

143 To further understand transcriptomic changes in the Aβ niche distinguishing those with limited vs.
144 extensive Aβ clearance, we visualized nonlinear relationships between gene expression and Aβ density within
145 Aβ-rich ST spots with a 200 μm radius. We first used locally estimated scatterplot smoothing (LOESS)
146 (**Extended Data Fig. 1m-n**). We employed hierarchical clustering to delineate distinct expression patterns with
147 increasing Aβ density within the iAD group (**Fig. 1o** and **Extended Data Table 2**). Pathway analysis of genes

148 in each cluster subsequently revealed that cluster 4, which showed a gradual increase peaking in the Aβ-rich
149 spots, was enriched for immune-related pathways, including complement signaling, inflammatory response,
150 and IL-2/STAT5 signaling (**Fig. 1p** and **Extended Data Table 2**). Notably, this gene cluster showed the highest
151 upregulation in iAD-lim Aβ niches, with a lesser increase in iAD-ext and no upregulation in nAD (**Fig. 1q** and
152 **Extended Data Table 2**). This cluster contained many immune-associated, including *A2M*, *APOE*, *Complement*
153 *C3* (*C3*), *RAB13, Member RAS Oncogene Family* (*RAB13*), and *Secreted Phosphoprotein 1* (*SPP1*) (**Fig. 1r**
154 and **Extended Data Table 2**). These findings together highlight an inflammatory immune response toward Aβ
155 in AN1792-immunized brains with limited Aβ clearance, marked by IL-2/STAT5 and complement signaling,
156 along with upregulation of genes associated with the microglial response in AD.
157

158 **Inflammatory and neuroprotective microglial responses distinguish levels of Aβ clearance in actively**
159 **immunized AD patient brains**

160 Since Visium ST spots are large enough to encompass approximately 1-10 cells each, we next aimed
161 to understand their cellular composition. To do so, we used the deconvolution method Cell2Location[38] to
162 computationally integrate ST data with a single-nucleus RNA sequencing (snRNAseq) dataset to resolve fine-
163 grained cell-types. We constructed a reference atlas using a snRNA dataset from 424 dorsolateral prefrontal
164 cortex (DLPFC) tissues derived from AD and NND controls[39, 40] (**Fig. 2a** and **Extended Data Fig. 2a**). We
165 randomly down-sampled this atlas to 34,695 cells to achieve nearly equal representation of each cell-type. We
166 then utilized Cell2Location to analyze the estimated abundances and spatial location of cell-types in our ST
167 dataset. Cell-types mapped to their expected locations within tissues [e.g. oligodendrocytes to white matter,
168 layer II/III excitatory neurons (L2/3 ENs) to cortical layers II/III and smooth muscle cells to the meninges] (**Fig.**
169 **2b** and **Extended Data Fig. 2b**). Using the C2L predicted abundance of each cell type per ST spot, we
170 calculated the overall cellular proportions in the gray matter. We excluded layer I from this analysis due to
171 variable, non-specific results associated with its lower cell density. Although we observed no significant
172 differences, we noted a trend of increased astrocyte proportions in iAD-ext and increased microglia in iAD-lim,
173 along with a reduction in L2/3 ENs in nAD, which became more pronounced following AN1792 immunization
174 (**Extended Data Fig. 2c**). We then applied the constraints of manually annotated ST spots (**Fig. 1d**) to inform
175 predictions of cell-types enriched in each spot. To achieve robust results, we then annotated the most highly

176 enriched ST spots for a specific cell-type within the relevant spatial area (**Fig. 2c**). For example, ST spots
177 enriched for layer IV excitatory neurons (L4 EN) were identified by their highest predicted abundances of L4
178 ENs and were annotated exclusively within the manually defined cortical layer IV. For microglia, we annotated
179 the top ST spots across both gray and white matter. Layer I ST spots were excluded from this analysis.

180 When we compared iAD versus nAD gene expression across cell-type-enriched ST spots, we found
181 that L2/3 EN-enriched spots had the highest number of DEGs, followed by microglia and astrocytes (**Fig. 2d**,
182 **Extended Data Fig. 2d**, and **Extended Data Table 2**). In contrast, in NND samples compared to nAD, the top
183 three cell type-enriched ST spots with the most DEGs were enriched for layer IV/V excitatory neurons (L4/5
184 ENs), interneurons, and L2/3 ENs, respectively (**Fig. 2d** and **Extended Data Fig. 2e**, and **Extended Data**
185 **Table 2**). Genes upregulated in microglia-enriched ST spots in iAD vs. nAD included *APOE*, *TREM2*, *A2M*,
186 *RAB13*, *FAM107A*, and others associated with microglial responses to amyloid, such as *LAMP1*, *CD163*
187 *Molecule* (*CD163*), *PYD And CARD Domain Containing* (*PYCARD*), *Integrin Subunit Alpha X* (*ITGAX*), and
188 *Apolipoprotein C1* (*APOC1*) (**Fig. 2e**, and **Extended Data Table 2**). *PYCARD* activates the inflammasome and
189 forms apoptosis-associated speck-like protein containing a CARD (ASC) specks, which can act as
190 inflammation-driven cross-seeds for Aβ pathology[41]. Similarly, *ITGAX* is associated with phagocytic/activated
191 microglia in AD mouse models[23, 24], and *CD163* is a key marker of amyloid-responsive microglia[25, 26]. Among
192 the downregulated genes were several HSP coding genes. We then examined the top divergent DEGs in iAD
193 vs. nAD and nAD vs. NND by their probability fold change (PFC) score—defined as the product of the negative
194 logarithm of the adjusted p-value and the absolute logarithm of the fold change (**Fig. 2f**, and **Extended Data**
195 **Table 2**). Notably, *DNAJA1* was one of the most divergent DEGs in microglia-enriched ST spots and was
196 downregulated after immunization. Another highly divergent gene downregulated post-immunization was *Fas*
197 *Apoptotic Inhibitory Molecule 2* (*FAIM2*). *FAIM2* primarily functions to inhibit Fas-mediated apoptosis, promoting
198 cell survival and protecting against programmed cell death[42]. Reduced inhibition of Fas-mediated apoptosis
199 may explain the loss of tau-associated neurite clusters and neuronal cell bodies in areas devoid of plaques
200 after AN1792 immunization[12].

201 Next, we conducted differential expression analysis of microglia-enriched ST spots within the gray
202 matter, comparing iAD-lim and iAD-ext groups to nAD. Microglia-enriched ST spots in the iAD-ext group
203 exhibited a higher number of DEGs compared to nAD than iAD-lim or NND controls (**Fig. 2g** and **Extended**

204 **Data Fig. 2f-g** and **Extended Data Table 2**). Unique genes upregulated in iAD-ext included aforementioned
205 *APOE* and *MARCKS*, as well as *Fibroblast Growth Factor Receptor 3* (*FGFR3*) (**Fig. 2h** and **Extended Data**
206 **Table 2**). *FGFR3* acts as a receptor for *Fibroblast Growth Factor 2* (*FGF2*), a factor released by neurons in
207 response to damage caused by oligomeric $A\beta_{1-42}$. This *FGF2-FGFR3* interaction promotes microglial migration
208 and phagocytosis of neuronal debris, contributing to neuroprotection[43]. In the iAD-lim group, we found
209 upregulation of previously mentioned *TREM2*, *A2M*, *LAMP1*, and *Transmembrane Immune Signaling Adaptor*
210 *TYROBP* (*TYROBP*) (**Fig. 2h** and **Extended Data Table 2)**. Interestingly, TYROBP forms a critical link between
211 TREM2 at the microglial surface and *APOE* transcription in microglia[44]. Both groups shared upregulation of
212 *PYCARD* and *Toll-Like Receptor 7* (*TLR7*) (**Fig. 2h** and **Extended Data Fig. 2f-g** and **Extended Data Table**
213 **3**). Although most group-specific genes showed similar trends in the other group, they did not reach significance
214 (**Fig. 2i** and **Extended Data Table 2**). We confirmed protein localization of *TMS1/ASC* (encoded by *PYCARD*),
215 *A2M*, and *APOE* in $Iba1^+$ microglia around Aβ plaque pathology in the frontal cortex of AN1792 immunized
216 subjects (**Fig. 2j-l).** Given the similar gene expression patterns across the two groups, we focused on the most
217 divergent genes in microglia-enriched spots between groups with varying levels of Aβ clearance (**Extended**
218 **Data Fig. 2h**, **Extended Data Table 2**). In iAD-lim, the most divergent genes were *Leukocyte-Specific Protein*
219 *1 (LSP1)* and *GTPase Of Immunity-Associated Proteins (GIMAPs)*, both of which were upregulated. Notably,
220 *LSP1* localizes to nascent phagocytic cups during Fcγ receptor-mediated phagocytosis[45]. In iAD-ext, the most
221 divergent genes were the earlier mentioned *FGFR3*, which was upregulated, and *HSPA1A*, which was
222 downregulated. Pathway enrichment analysis of unique and shared DEGs in microglia-enriched spots revealed
223 a common upregulation of IL-2/STAT5 signaling and a specific upregulation of oxidative phosphorylation
224 (OXPHOS) and adipogenesis in extensively cleared brains (**Fig. 2m**, **Extended Data Table 2**). Conversely,
225 complement signaling and the unfolded protein response were downregulated in iAD-lim.

226 We then directly compared genes shared between iAD-ext vs. nAD and NND vs. nAD comparisons in
227 microglia-enriched spots. We reasoned that this approach might identify transcriptomic changes that reflect a
228 return to homeostasis in iAD-ext brains. Shared upregulated genes included previously mentioned
229 neuroprotective *FGFR3*, *Cold-Inducible RNA Binding Protein* (*CIRBP*), and *Sorbin And SH3 Domain Containing*
230 *3* (*SORBS3*), while downregulated genes included *FAIM2*, *DNAJA1*, and *HSP90AA1* (**Fig. 2n-o**, **Extended**
231 **Data Table 2**). *CIRBP* is a stress-responsive gene that ameliorates neuronal amyloid toxicity via antioxidative

232 and antiapoptotic pathways[46] and modulates inflammation[47]. Overall, these findings suggest that dysregulated
233 genes in microglia-enriched ST spots of iAD-ext brains reflect a shift in microglial gene expression towards a
234 profile more like that of non-demented controls.

235 To investigate the functional state of microglia after AN1792 immunization, we compared microglia-
236 enriched ST spot signatures of iAD brains to previously published human AD microglial states[40, 48]. Using gene
237 set enrichment analysis (GSEA) on one set of microglial states[48], we observed significant decreases in stress-
238 signature microglia (MG6) across comparisons, including NND vs. nAD, iAD vs. nAD, iAD-lim vs. nAD, and
239 iAD-ext vs. nAD (**Fig. 2p** and **Extended Data Table 2**). In iAD-ext specifically, there was a reduction in
240 inflammatory microglia states (MG2, MG8, MG10), glycolytic microglia (MG7), and an increase in ribosome
241 biogenesis microglia (MG3). This reduction in inflammatory microglia was also observed in NND vs. nAD
242 comparisons. NND samples also had a decrease in phagocytic microglia (MG5), though this was not seen in
243 iAD groups. Using a separate microglial classification[40], we noted significant reductions in stress-responsive
244 microglia (Mic.11) across NND vs. nAD, iAD vs. nAD, iAD-lim vs. nAD, and iAD-ext vs. nAD (**Fig. 2q** and
245 **Extended Data Table 2**). In iAD-ext specifically, there was a reduction in surveilling microglia (Mic.2, 4),
246 reactive microglia (Mic.6-8), interferon-responsive microglia (Mic.14), and SERPINE1-expressing microglia
247 (Mic.16). In summary, pathway analyses of published human microglia functional states indicate a reduction in
248 stress-responsive microglia after AN1792 immunization, resembling patterns seen in NND samples. In
249 microglia-enriched ST spots in brains with extensive Aβ clearance, we observed a metabolic shift from
250 glycolysis to oxidative phosphorylation, accompanied by a decrease in inflammatory states.

251 Overall, our data shows that active Aβ immunization reduces the prevalence of stress-responsive
252 microglia, regardless of residual Aβ levels. In iAD brains with extensive Aβ clearance, microglia exhibit a
253 metabolic shift accompanied by a reduced inflammatory profile, which may facilitate sustained Aβ clearance
254 activity. In contrast, iAD brains with limited clearance demonstrate downregulation of pathways like the unfolded
255 protein response and complement, along with elevated expression of disease-associated microglia (DAM)
256 associated genes *TREM2* and *TYROBP*, indicating an active response to Aβ. Notably, complement activation
257 products may protect against Aβ-induced neurotoxicity, and contribute to the clearance of amyloid and the
258 degeneration of neurons[49]. Altogether, these findings imply that effective amyloid clearance may hinge on
259 microglia sustaining a balanced metabolic state to support energy production and cellular repair.

260

261 **Microglial transcriptomic alterations associated with Aβ clearance in an AD patient treated with**
262 **lecanemab**

263 Intrigued by the altered microglial response to Aβ in actively immunized AD brains, we next explored
264 the immune response to Aβ following passive immunization with lecanemab (**Fig. 3a**). We studied a unique
265 case of a 65-year-old female AD patient who participated in a phase III trial of lecanemab[17, 18]. This patient
266 received three lecanemab infusions over the course of five weeks. The patient then developed acute ischemic
267 stroke-like symptoms shortly after the final lecanemab dose and passed away days later[17]. Our post-mortem
268 analysis of this patient's brain revealed histiocytic vasculitis in vessels affected by CAA, with evidence of
269 vascular Aβ fragmentation and phagocytosis across the cerebral cortex[18]. This was in addition to a "high"
270 burden of AD pathology according to National Institute on Aging and Alzheimer's Association consensus
271 guidelines[50]. Notably, we also observed parenchymal Aβ plaque phagocytosis[18]. We compared this patient's
272 brain to three *APOE* ε4/ε4 genotype-matched pathological controls with a high burden of AD pathology (**Fig.**
273 **3b** and **Extended Data Table 1**). Importantly, these control patients had not received any form of anti-Aβ
274 treatment yet had vascular AD pathology in addition to advanced AD. Of these, one donor had CAA-related
275 microbleeds in antemortem magnetic resonance imaging, indicative of severe CAA. We assessed cortical
276 tissues of all subjects from the left middle frontal gyrus (FCX), left superior temporal gyrus (TCX), left inferior
277 parietal lobule (PCX), as well as the posterior hippocampus (HIPP) (**Fig. 3b**). We chose these brain regions
278 because we previously demonstrated their variable levels of Aβ clearance[18]. We then performed single-cell
279 fixed RNA profiling (scRNAseq) and spatial proteogenomics—an approach that simultaneously captures spatial
280 mRNA and protein changes using barcoded probes and antibodies—to identify cell-type-specific immune
281 responses to passive Aβ immunization in these brain regions (**Fig. 3c**).

282 Tissue sections from each brain region were stained for Iba1 and pan-Aβ (with the 4G8 antibody) (**Fig.**
283 **3d** and **Extended Data Fig. 3a**). We used the 4G8 antibody since we previously employed it to delineate Aβ
284 pathology and clearance in this case[18]. We differentiated cortical and vascular Aβ pathology by both manual
285 annotation and LABKIT, a random forest ensemble learning algorithm[51] (**Fig. 3d** and **Extended Data Fig. 3a**).
286 Quantification of gray matter Aβ coverage revealed reduced cortical Aβ deposits in the TCX and PCX of the
287 lecanemab-treated patient compared to the nAD controls (**Fig. 3e**). Moreover, a higher fraction of cortical Aβ

288 deposits in the lecanemab case were covered by Iba1^{+} cells, increasing from an average of ~15% in the nAD
289 controls to ~44% in the lecanemab case (**Fig. 3f**). These results recapitulate our previous finding that there are
290 varying levels of Aβ clearance among different brain regions of the lecanemab case[18].

291 To further investigate the immune response to Aβ following passive immunization, we performed
292 scRNAseq on cells isolated from FFPE tissues of each brain region. We used SoupX[52] to minimize ambient
293 RNA contamination (**Extended Data Fig. 3b**). Quality control metrics showed variability in the number of
294 expressed genes (**Extended Data Fig. 3c**) and in the percentages of mitochondrial reads across brain regions
295 (**Extended Data Fig. 3d**). However, we did not detect statistically significant differences between nAD and the
296 lecanemab-treated case across brain regions (**Extended Data Fig. 3c-d**). We integrated cells from all tissues
297 (**Extended Data Fig. 3e**) and annotated cell clusters using their highly expressed genes (**Fig. 3g** and **Extended**
298 **Data Fig. 3f** and **Extended Data Table 3**). In the lecanemab case, we observed a relative increase in
299 GABAergic interneurons (GINs) and a decrease in endothelial cells, fibroblasts, and smooth muscle cells
300 across all brain regions compared to the nAD controls (**Fig. 3h** and **Extended Data Fig. 3g**). Notably, T cells
301 were enriched in all regions except the hippocampus; monocytes and macrophages were enriched in the PCX
302 and TCX of the lecanemab case, and microglia were increased in the TCX, PCX, and HIPP (**Fig. 3h** and
303 **Extended Data Fig. 3g**).

304 We then performed MAST differential expression analysis on microglia and macrophages from all brain
305 regions combined (**Fig. 3i-j** and **Extended Data Table 3**). Upregulated genes in microglia of the lecanemab
306 case were associated with microglial activation and inflammation (*SPP1*, *Chitinase 3 Like 1* (*CHI3L1*), and
307 *Folate Receptor Beta* (*FOLR2*)), lysosomal function and protein degradation (*Cathepsin B* (*CTSB*), *Granulin*
308 (*GRN*)), interferon responses (*Interferon Alpha Inducible Protein 6* (*IFI6*)). Additional upregulated genes
309 included those involved in iron storage and regulation (*Ferritin Heavy Chain 1* (*FTH1*), *Ferritin Light Chain*
310 (*FTL*)), lipid metabolism processes (*Apolipoprotein C1* (*APOC1*)) and extracellular matrix and tissue remodeling
311 (*Transforming Growth Factor Beta Induced* (*TGFBI*), *Olfactomedin Like 3* (*OLFML3*)). Notably, *SPP1* and
312 *APOC1* were the most upregulated, microglia-specific DEGs (**Fig. 3j**). Intriguingly, *SPP1* is expressed by
313 activated-response microglia[53] and contributes to tissue repair[54]. We confirmed protein expression of both
314 SPP1 and APOC1 in plaque-associated microglia within the hippocampus following lecanemab treatment
315 (**Extended Data Fig. 3h-i**). Upregulated genes in macrophages were involved in activation and inflammation

316 (*TREM2*, *Macrophage Receptor With Collagenous Structure* (*MARCO*), *MAF BZIP Transcription Factor B*
317 (*MAFB*)), lysosomal function and protein degradation (*Cathepsin Z* (*CTSZ*), *CTSB*, *Cathepsin L* (*CTSL*),
318 *Cathepsin H* (*CTSH*), *Granulin* (*GRN*)). Additional upregulated genes included those involved in lipid
319 metabolism (*APOE*, *A2M*), cytoskeletal dynamics (*Fascin Actin-Bundling Protein 1* (*FSCN1*), *MARCKS*); and
320 phagocytosis (*CD68 Molecule* (*CD68*), *Fc Fragment Of IgG Binding Protein* (*FCGBP*)). Both microglia and
321 macrophages showed decreased expression of HSP-coding genes, such as *HSPA1B* in microglia, and *HSPH1*
322 and *Heat Shock Protein Family A (Hsp70) Member 8* (*HSPA8*) in macrophages. *Heme Oxygenase 1* (*HMOX1*)
323 was the most upregulated gene shared among microglia and macrophages. *HMOX1* is involved in heme
324 metabolism, possibly indicating an immune response to hemorrhages that occurred lecanemab case. To study
325 microglia and macrophage functions after immunization, we performed enrichment analysis. Interestingly,
326 pathways regulating vascular functions such as apical junctions, coagulation, and angiogenesis were
327 upregulated in both macrophages and microglia (**Fig. 3k** and **Extended Data Table 3**). Additionally, we found
328 dysregulation of complement signaling in macrophages and increased complement signaling in microglia (**Fig.
329 3k** and **Extended Data Table 3**). We also observed dysregulated IL-2/STAT5 signaling in microglia, with both
330 downregulated and upregulated DEGs associated with this pathway (**Fig. 3k** and **Extended Data Table 3**).
331 These data highlight distinct alterations to the brain myeloid compartment following passive Aβ immunization.
332 Notably, disparate microglial transcriptomic signatures were observed across different brain regions in
333 the lecanemab case (**Extended Data Fig. 3j** and **Extended Data Table 3**). Most changes in microglial gene
334 expression were observed in the TCX and PCX, the two regions with the least residual Aβ (i.e., more Aβ
335 clearance, as noted in **Fig. 3e**). Microglia from these regions exhibited increased expression of genes involved
336 in complement signaling (*Complement Component 3* (*C3*)), lysosomal function and protein degradation (*CTSZ*,
337 *CTSB*), iron storage and regulation (*FTH1*, *FTL*); and an increase in microglial *SPP1* (**Extended Data Fig. 3j**
338 and **Extended Data Table 3**). Regional DEGs were associated with various signaling pathways. In the FCX,
339 DEGs indicated increased reactive oxygen species (ROS) signaling (**Fig. 3l** and **Extended Data Table 3**). The
340 TCX and PCX showed increased complement signaling, while the PCX also exhibited decreased interferon
341 responses, among other changes (**Fig. 3l** and **Extended Data Table 3**). The HIPP demonstrated decreased
342 cholesterol homeostasis (**Fig. 3l** and **Extended Data Table 3**). Additionally, microglial DEGs were linked to
343 angiogenesis and coagulation pathways, but this association was present only in the TCX and PCX, areas with

344 extensive Aβ clearance (**Fig. 3l** and **Extended Data Table 3**). These distinct microglial phenotypes may
345 underlie the variability in Aβ clearance between brain regions of the lecanemab case.

346 We also identified a notable shift in microglial states[48] across brain regions, with a decrease in
347 inflammatory state II microglia (MG8) and an increase in ribosome biogenesis (MG3) across all regions
348 combined (**Extended Data Fig. 3k** and **Extended Data Table 3**). Intriguingly, the MG3 microglia state also
349 exhibits strong enrichment of DAM signature genes[48]. Specifically, in the FCX, where the amount of residual
350 amyloid was highest, there were reductions in inflammatory states I, II, and III (MG2, MG8, MG10), as well as
351 in phagocytic (MG5), stress-signature (MG6), and glycolytic microglia (MG7). Notably, MG8 microglia are
352 typically elevated in AD and positively correlated with plaques[48]. Interestingly, despite increased microglial
353 clustering around plaques, the phagocytic microglia state (MG5) was decreased in the HIPP. In the PCX,
354 inflammatory state III microglia (MG10) were increased. Applying separate microglial classifications[40] showed
355 a similar pattern with several microglial states downregulated in the FCX, that were upregulated in the TCX,
356 PCX, and HIPP regions (**Extended Data Fig. 3l** and **Extended Data Table 3**). These included surveilling
357 (Mic.2, 3, 4), reacting (Mic.7), enhanced redox (Mic.10), lipid-associated (Mic.12), inflammatory (Mic.15), and
358 SERPINE1-expressing microglia (Mic.16). Enhanced redox (Mic.9) was upregulated in the TCX and HIPP
359 microglia, while proliferative (Mic.1), reacting (Mic.6), and stress-responsive microglia (Mic.11) states were
360 downregulated specifically in the FCX. Despite *SPP1* being the most upregulated gene in microglia, there was
361 no enrichment in Mic.13 (characterized as *PTPRG*$^{+}$*SPP1*$^{+}$*TREM2*$^{+}$); rather, the Mic.13 state was
362 downregulated in FCX microglia. Together, these findings demonstrate a reduction in inflammatory MG8
363 microglia and an increase in ribosome biogenesis and DAM-expressing MG3 microglia across all regions
364 following lecanemab immunization. Notably, we identified a distinct microglial profile in the FCX compared to
365 other brain regions within the lecanemab case.

366 We then sub-clustered immune cells from the lecanemab case and nAD controls into five microglial
367 clusters, two macrophage clusters, one monocyte cluster, and one T cell cluster (**Fig. 3m** and **Extended Data**
368 **Fig. 3m-n**). One macrophage cluster (*Mac-1*) expressed markers of border-associated macrophages, such as
369 *Lymphatic Vessel Endothelial Hyaluronan Receptor 1* (*LYVE1*) and *Sialic Acid Binding Ig Like Lectin 1*
370 (*SIGLEC1*) (**Extended Data Fig. 3n**). *Mac-2*, which was less abundant in the lecanemab-treated case, shared
371 gene expression profiles with both *Mac-1* and monocytes and exhibited a stress-response signature, including

372 elevated expression of *DNAJB1*, *HSPA6*, and *HSPB1* (**Extended Data Fig. 3n-o**). Two microglial clusters, *Mg-*
373 *2* and *Mg-4*, had increased prevalence in the TCX, PCX, and HIPP of the lecanemab case (**Fig. 3n-o**). Since
374 these regions showed evidence of Aβ phagocytosis, we further explored the phenotypes of *Mg-2* and *Mg-4*.
375 *Mg-2* expressed a mixed profile of DAM markers such as *TREM2*, *APOE*, and *TYROBP*, along with homeostatic
376 markers like *Purinergic Receptor P2Y12* (*P2RY12*) and *Transmembrane Protein 119* (*TMEM119*) (**Fig. 3p**). Of
377 all microglia clusters, *Mg-2* expressed the highest levels of co-stimulatory *CD80 Molecule* (*CD80*), *AXL*
378 *Receptor Tyrosine Kinase* (*AXL*), *FCGBP*, and *SPP1*. Notably, TAM receptors like AXL detect and engulf Aβ
379 plaques[55]. *Mg-2* also expressed higher levels of *CD74* and *C3* compared to *Mg-4*. *Mg-4* expressed a typical
380 DAM signature, with high levels of *Integrin Subunit Alpha X* (*ITGAX*), *Lipoprotein Lipase* (*LPL*), *Matrix*
381 *Metallopeptidase 9* (*MMP9*), and *CHI3L1*. Notably, both *Mg-2* and *Mg-4* microglial clusters exhibited
382 upregulation of complement pathway signaling (**Fig. 3q** and **Extended Data Table 3**). The FCX, the region
383 with the most residual Aβ, exhibited higher levels of *Mg-0*, characterized by elevated expression of *FAM107A*
384 and Clusterin (*CLU*), along with decreased complement signaling among other immune pathways.

385 In summary, we found that lecanemab treatment induces two distinct Aβ-associated microglial
386 phenotypes, both expressing DAM markers such as *APOE* and *TREM2* and exhibiting increased complement
387 signaling in an AD patient. Yet, these lecanemab-associated microglia are unique from classic DAM microglia
388 by their altered expression of signaling molecules like *CD80*, *AXL*, *C3*, and *CD74*. Notably, microglia in the
389 lecanemab-treated case showed a decrease in the inflammatory MG8 state[48]—regardless of Aβ clearance
390 levels—and an increase in the ribosomal biogenesis MG3 state[48]. Altogether, these findings characterize
391 distinct microglial states responsive to passive Aβ immunization in an AD patient treated with lecanemab.
392

393 **Microglia recruited to the Aβ niche upregulate *SPP1* following lecanemab treatment**

394 Having established the microglial response to lecanemab treatment using single-cell analysis, we next
395 sought to elucidate immune dynamics of the Aβ niche within tissues. To do so, we performed spatial
396 proteogenomics on tissue sections from the same FFPE blocks using a larger ST capture area of 11 x 11 mm
397 comprising 14,336 ST spots (**Fig. 4a**). ST spots were annotated based on DAPI staining to demarcate
398 meninges, cortical layers, white matter and areas with hemorrhage (**Fig. 4b** and **Extended Data Fig. 4a**).
399 Quality control metrics revealed variability in the number of expressed genes across nAD donors (**Extended**

400 **Data Fig. 4b**) and in mitochondrial read percentages (**Extended Data Fig. 4c**). However, regional comparisons
401 showed no significant differences in these metrics between nAD group and the lecanemab sample. We then
402 used binary masks to distinguish cortical and vascular Aβ, construct expanded Aβ niches and define Aβ-rich
403 ST spots (**Fig. 4c**). Consistent with findings from AN1792, we observed that cortical Aβ was predominantly
404 reduced in the superficial cortical layers (I and II) (**Extended Data Fig. 4d**). We performed differential
405 expression analysis across these cortical regions and, unlike AN1792, observed that the deeper cortical layers
406 (III, IV, and V/VI) exhibited the most DEGs (**Fig. 4d** and **Extended Data Table 4**).

407 Transcriptomic analysis of cortical Aβ-positive ST spots revealed that residual Aβ-rich ST spots in brain
408 regions with the most clearance (TCX and PCX) were the most transcriptionally dysregulated (**Extended Data**
409 **Fig. 4e and Extended Data Table 4**). In line with the single-cell analysis findings in microglia in Figure 3, Aβ-
410 rich ST spots in the TCX exhibited higher expression of genes related to complement signaling (*C3*,
411 *Complement C1q C Chain* (*C1QC*) and lipid metabolism (*APOE*, *LIPA*) (**Fig. 4e** and **Extended Data Fig. 4f**
412 and **Extended Data Table 4**). We observed ApoE localized to Aβ plaques surrounded by Iba1$^+$ myeloid cells
413 in the lecanemab-treated brain (**Extended Data Fig. 4g**). Additionally, all regions except the uncleared FCX
414 shared upregulated genes involved in lysosomal function and protein degradation (*A2M, CTSB*, *CTSZ*), iron
415 storage (*FTH1*, *FTL*), and extracellular matrix remodeling during inflammation (*CHI3L1*). We also observed
416 A2M localized to Iba1$^+$ myeloid cells around Aβ deposits (**Extended Data Fig. 4h**). Notably, we found
417 upregulation of *SPP1* and *FTH1* across all regions. Pathway analysis of Aβ-rich ST spots in the TCX revealed
418 upregulation of complement signaling pathways (**Fig. 4f** and **Extended Data Table 4**). Intriguingly,
419 adipogenesis pathways increased across all regions, suggesting involvement in lipid metabolism processes
420 (**Fig. 4f** and **Extended Data Table 4**).

421 We next evaluated immune responses at the protein level within cortical Aβ niches. Notably, many
422 immune-related genes are either expressed at low levels or undergo post-translational modifications. This
423 sometimes results in the exclusion of their corresponding transcripts from differential gene expression analysis,
424 or the absence of such transcripts altogether. To overcome this, we adapted our ST method to incorporate a
425 panel of 31 barcoded antibodies targeting immune proteins (**Extended Data Table 4)**. These barcoded
426 antibodies were transferred simultaneously with RNA probes to generate spatial proteogenomics data. We
427 assessed differentially expressed proteins (DEPs) with or without a corresponding DEG transcript (**Fig. 4g and**

428 **Extended Data Table 4**). Among the DEPs, HLA-DRA, a component of class II antigen presentation, was
429 upregulated in Aβ-rich ST spots across all brain regions (**Fig. 4g and Extended Data Table 4**). Proteins linked
430 to the microglial phagocytic response to amyloid, such as CD11c and CD68, were upregulated in both the TCX
431 and HIPP. Given that CD68 is a key component of the lysosomal/endosomal-associated membrane, we
432 confirmed this finding with IHC, which revealed numerous $CD68^+$ lysosomal structures within $Iba1^+$ microglia
433 surrounding Aβ deposits in the HIPP (**Fig. 4h** and **Extended Data Fig. 4i**). Interestingly, the immune-inhibitory
434 receptor ligand Programmed Cell Death 1 Ligand 1 (PDL1) was reduced in regions with the highest Aβ
435 clearance (TCX, PCX). We further employed LOESS to assess non-linear mRNA expression changes within
436 Aβ-rich spots and a 200 μm radius in the lecanemab-treated brain (**Extended Data Fig. 4j-k**). We identified 11
437 clusters (**Extended Data Fig. 4l** and **Extended Data Table 4**), with cluster 3 being most associated with
438 immune pathways, including complement and IL2/STAT5 signaling (**Extended Data Fig. 4m**). Cluster 3 was
439 notably upregulated in ST spots with the highest Aβ content, and included previously identified genes such as
440 *A2M*, *APOE, APOC1, CTSB*, *CD68, FCGBP*, *ITGAX*, *SPP1*, and *TREM2* (**Fig. 4i-j** and **Extended Data Fig.**
441 **4n)**. In summary, proteogenomic analysis of the Aβ niche revealed microglial states associated with Aβ
442 clearance in an AD patient treated with lecanemab.
443

444 **Transcriptomics reveals a shared microglial gene signature between active and passive Aβ**
445 **immunization**

446 To identify common and distinct microglial responses to Aβ following active and passive immunization
447 strategies, we performed integrated analyses of all tissues. Initially, we quantified general Aβ coverage in the
448 gray matter, confirming a decrease in Aβ coverage associated with AN1792 and lecanemab treatment (**Fig. 5a-**
449 **b**). We also observed increased myeloid recruitment associated with AN1792 and lecanemab treatment (**Fig.**
450 **5c**). To examine differences in the cellular response to Aβ following immunization, we integrated and clustered
451 cortical gray matter Aβ-rich ST spots (**Fig. 5d** and **Extended Data Fig. 5a-b**). This analysis yielded nine distinct
452 Aβ niches based on their gene expression profiles (**Fig. 5d** and **Extended Data Fig. 5c** and **Extended Data**
453 **Table 5**). We hypothesized that these differences were driven by distinct cellular microenvironments. To test
454 this, we employed Cell2Location to predict the abundances of cell types defined in our integrated scRNAseq
455 atlas consisting of nAD, lecanemab, and AN1792 samples (**Extended Data Fig. 5d**). We then plotted the

456 distribution of cell types per plaque type across all samples. We found that different cellular microenvironments
457 were associated with different Aβ plaque clusters (**Fig. 5e**). Notably, the cortical Aβ-6 cluster exhibited the
458 highest enrichment of microglia and was increased in lecanemab samples, and to a lesser extent in AN1792
459 samples (**Fig. 5f**). Among the markers defining this cluster were *A2M, APOE, C1QC, C3, CD74, CHI3L1, CTSB,*
460 *FTL,* and *SPP1* (**Extended Data Fig. 5e** and **Extended Data Table 5**). This suggests that the cortical Aβ-6
461 cluster represents Aβ-rich ST spots with recruited myeloid cells. We next sought to resolve the specific myeloid
462 population driving this innate immune response to Aβ. In AN1792 samples with limited Aβ clearance, as well
463 as in lecanemab-treated brain regions, this cluster showed an increased relative abundance of microglia
464 clusters *Mg-2* and *Mg-4* compared to nAD controls (**Extended Data Fig. 5f**).

465 Through differential expression analysis of cortical Aβ-6 ST spots, we identified upregulation of
466 *FAM107A*, *RAB13*, *S100A4*, *Translocator Protein (TSPO)*, and *TREM2* in AN1792 samples compared to their
467 corresponding nAD controls (**Fig. 5g**, **Extended Data Fig. 5g** and **Extended Data Table 5**). In ST spots from
468 the lecanemab-treated brain, we observed upregulation of *A2M*, *Actin Beta (ACTB)*, *APOE*, *CHI3L1*,
469 *Coagulation Factor III (F3)*, *CTSB*, *FTH1*, and *FTL*, among other genes (**Fig. 5h**, **Extended Data Fig. 5g** and
470 **Extended Data Table 5**). Because *SPP1* had no zero counts, the MAST hurdle model—which relies on
471 modeling excess zeros—was inappropriate for this gene. Therefore, we used DESeq2 to analyze *SPP1*
472 expression, finding that *SPP1* was highly upregulated in cortical Aβ-6 ST spots of the lecanemab-treated brain
473 (**Fig. 5i**). We then investigated whether any of the previously identified microglial subtypes were mediating this
474 effect or were spatially associated with the Aβ plaque niche. Using Cell2Location data (**Fig. 5j**), we plotted the
475 $\log_2$ fold change of predicted microglial abundance per donor in cortical Aβ-rich spots vs. other gray matter
476 spots (**Fig. 5k** and **Extended Data Fig. 5h**). This analysis revealed enrichment of microglial clusters *Mg-2* and
477 *Mg-4* in Aβ-rich spots, most notably in the lecanemab-treated brain, and to a lesser extent in AN1792 subjects
478 with limited clearance.

479 We defined *Mg-2* and *Mg-4* enriched ST spots in the gray matter of our cohorts and filtered those spots
480 to include only those that were Aβ-rich or within a 200 μm proximity of an Aβ-rich spot. In Aβ-associated *Mg-2*-
481 enriched spots, we found increased expression of *APOE* in AN1792 samples (**Fig. 5l** and **Extended Data Table**
482 **5**). Note that these samples all had limited clearance, as there was an insufficient number of Aβ spots in iAD-
483 ext AN1792 samples. In Aβ-associated *Mg-4*-enriched spots, we observed increased expression of *APOE* and

484 *FAM107A*. Following lecanemab treatment, Aβ-associated *Mg-2* and *Mg-4* enriched spots exhibited very similar
485 gene expression profiles, including increased expression of *SPP1* and other genes associated with DAM
486 microglia (*TREM2*, *APOE*), lysosomal function and protein degradation (*A2M*, *CTSB, Lipase A, Lysosomal Acid*
487 *Type* (*LIPA*)), and iron storage and regulation (*FTH1, FTL*) (**Fig. 5m** and **Extended Data Table 5**). We
488 visualized fold changes of these genes on a pseudobulk level, demonstrating that *FAM107A* is uniquely
489 increased in both *Mg-2* and *Mg-4* Aβ-associated ST spots in AN1792 samples, whereas *SPP1* and *LIPA* are
490 associated only with lecanemab treatment (**Extended Data Fig. 5i**). Notably, *APOE* and *TREM2* were
491 increased after both treatments, with *TREM2* showing slightly higher expression in Aβ-associated *Mg-2*-
492 enriched spots (**Extended Data Fig. 5i**).

493 We next employed CellChat[56] to map cell-to-cell signaling of the most dysregulated pathways
494 associated with Aβ immunization. We assessed cell communication networks associated with ApoE,
495 Complement, and SPP1 pathways in five FCX AN1792 samples, as well as in the FCX, TCX, PCX, and HIPP
496 regions of nAD and the lecanemab-treated brain (**Extended Data Fig. 5j** and **Extended Data Table 5**).
497 CellChat identified increased microglial signaling of all three pathways in the lecanemab-treated brain and
498 elevated ApoE pathway signaling in AN1792 samples (**Extended Data Fig. 5j**). These data also reveal a
499 network of signaling by microglia to other cell-types via these pathways, suggesting that microglia have a broad
500 impact of cellular communication in response to Aβ immunization.

501 To achieve single-cell resolution of ST data from immunized AD patient brains, we applied a platform
502 for high-definition spatial transcriptomics (HDST; Visium HD). We applied HDST to the hippocampus of the
503 lecanemab-treated brain and two nAD controls (**Extended Data Table 1**). We performed nuclei segmentation
504 using Stardist[57] and binned transcripts to nuclei. Nuclei were then integrated and clustered (**Fig. 5n** and
505 **Extended Data Fig. 5k-o**), with clusters annotated based on their top markers (**Extended Data Fig. 5o** and
506 **Extended Data Table 5).** We mapped cortical Aβ plaques based on immunofluorescent staining using the
507 monoclonal Aβ antibody D54D2 and then calculated the distance of each annotated nucleus to the nearest
508 plaque (**Fig. 5o**). Interestingly, myeloid cells (putative microglia) were overrepresented within a 20 μm radius
509 of plaques in the lecanemab case but not in nAD controls, indicating increased microglial recruitment to Aβ
510 plaques (**Fig. 5p**). Differential expression analysis of microglia within 20 μm of Aβ plaques post-lecanemab
511 treatment confirmed increased expression of *SPP1*, *FTH1*, *CHI3L1*, and *APOE* (**Fig. 5q** and **Extended Data**

512 **Table 5)**. SPP1 expression was visibly localized to nuclei around Aβ pathology (**Fig. 5r**). Importantly, these
513 data validate many of the lower resolution ST findings throughout the study.

514 Finally, to identify common and distinct gene expression changes in microglia and at the Aβ plaque
515 niche post-immunization, we compared DEGs from microglia and Aβ-niche datasets from AN1792- (**Fig. 1l, 2e,**
516 **5g, 5l**) and lecanemab-treated brains (**Extended Data Fig. 4f, Fig. 3i, 5f, 5m**). For each analysis, we ranked
517 genes by PFC. We then assigned percentile ranks based on these PFC scores. These percentiles were
518 averaged across all DE analyses for AN1792 (**Fig. 5s, Extended Data Fig. 5p, Extended Data Table 5**) and
519 lecanemab (**Fig. 5t, Extended Data Fig. 5q, Extended Data Table 5**). In AN1792-treated samples, *FAM107A*
520 was the top response gene, followed by metabolic regulator *ATP synthase inhibitory factor subunit 1 (ATP5IF1)*,
521 *TREM2*, and *APOE*. In contrast, lecanemab-treated samples showed *CHI3L1*, *F3*, *HMOX1*, and *SPP1* as the
522 top genes. Notably, when combining scores from both treatments, *TREM2* and *APOE* emerged as the top
523 responsive genes common to both AN1792 and lecanemab in microglia and Aβ-plaque niches (**Fig. 5u,**
524 **Extended Data Table 5**).

525 We then correlated the expression of *TREM2* and *APOE* in microglia-enriched spots within the gray
526 matter with available clinical data for AN1792-treated patients. This included peripheral blood anti-AN1792
527 antibody titers from the trial period and Aβ plaque scores assessed throughout the neocortex using a CERAD-
528 adapted method[12]. Notably, we found a significant, positive correlation between AN1792 antibody titer after
529 immunization and the expression of both *TREM2* and *APOE* (**Fig. 5v, Extended Data Table 5**). Additionally,
530 there was a trend toward a negative correlation between *APOE* expression and Aβ plaque score.

531 In conclusion, our analysis highlights both distinct (*FAM107A*, *SPP1*) and common (*APOE*, *TREM2*)
532 genes related to active and passive Aβ immunization. The expression levels of *APOE* and *TREM2* were directly
533 associated with the immunization response (i.e. antibody titer) and Aβ clearance (i.e. amyloid score). Altogether,
534 our findings delineate the microglial response mediating Aβ clearance in AD brains immunized against Aβ.

535

536 **Discussion**

537 The mechanisms by which immunization promotes Aβ clearance have long been posited to involve
538 phagocytosis by microglia[3]. Yet, the molecular mechanisms regulating microglial Aβ clearance in the human

539 AD brain have never been discerned. This study defines the microglial response to Aβ immunization in the AD
540 brain.

541 We detected upregulation of *APOE* and *TREM2* in microglia of actively and passively immunized AD
542 brains. Notably, side effects from passive immunization are more commonly observed in homozygous *APOE*
543 ε4 carriers[16, 58, 59]. Further, antibodies against Trem2 have been explored as a therapeutic strategy for AD[60, 61].
544 Yet, these early trials have also been hindered by side effects, particularly in *APOE* ε4 homozygotes[62]. Thus,
545 ApoE and Trem2 likely play crucial roles in the microglial response to Aβ following immunization, potentially
546 influencing both therapeutic efficacy and the risk of adverse effects.

547 The decreased expression of genes related to HSPs, protein folding and cellular stress in immunized
548 AD samples is in favor of an improved cerebral environment after active immunization. Additionally, we
549 observed a loss of stress-signature and stress-responsive microglia in immunized AD brains. We also observed
550 a reduction in inflammatory microglia in brains with extensive Aβ clearance. These changes collectively point
551 to a mitigation of the chronic inflammatory state often associated AD that is accompanied by a return to
552 homeostasis for extensively cleared brains. Interestingly, we found elevated expression of genes linked to
553 neuroprotection in microglia-enriched ST spots of iAD-ext brains. Among these upregulated genes was *FGFR3*,
554 which encodes a receptor that binds FGF2 secreted by degenerating neurons[43]. The FGF2-FGRR3 interaction
555 provides neuroprotection by facilitating microglial migration and phagocytosis of neuronal debris[43]. Thus,
556 FGFR3-FGF2 signaling potentially underlies neuronal-microglial communication in brains extensively cleared
557 of Aβ.

558 Our data indicate that the response to Aβ immunization depends on microglia transitioning to a
559 metabolically homeostatic state once intense activity is complete. Glycolysis, though less efficient in ATP
560 generation than mitochondrial respiration, supports rapid energy demands for processes like phagocytosis.
561 Conversely, resting cells favor mitochondrial respiration due to its higher efficiency. Exposure to Aβ induces a
562 metabolic shift in microglia from oxidative phosphorylation to glycolysis[63]. In AN1792-treated brains with
563 extensive clearance (iAD-ext), we found increased oxidative phosphorylation and reduced glycolysis in
564 microglia, suggesting a metabolic state closer to homeostatic cells. Additionally, our data suggest a role for
565 complement signaling in Aβ clearance, with components like C3 facilitating Aβ recognition and phagocytosis

566 by microglia. Complement activation products may also guard against Aβ-induced neurotoxicity, potentially
567 reducing amyloid buildup and supporting neuronal health[49].

568 We further investigated the microglial response mechanisms underlying passive Aβ immunization. To
569 this end, we assessed a case study of an *APOE* ε4 homozygous AD patient with CAA treated with lecanemab.
570 We compared this patient's brain to control *APOE* ε4 homozygous AD patients with vascular AD pathology who
571 did not receive lecanemab. scRNAseq analyses revealed an increased presence of two microglial subtypes in
572 regions with the highest Aβ clearance, both spatially associated with residual Aβ deposits. Both subtypes
573 expressed DAM markers, such as *APOE* and *TREM2*, and exhibited elevated complement signaling, yet
574 differed in their expression of homeostatic markers, and the expression of signaling molecules *AXL*, *C3*, and
575 *CD74*. Following lecanemab treatment, DAM markers were upregulated in residual Aβ-rich regions, with
576 genomic alterations in those areas strongly associated with complement signaling in regions demonstrating
577 more pronounced Aβ clearance.

578 Finally, we examined shared and unique microglial Aβ response mechanisms between actively and
579 passively immunized AD brains. Comparative analysis revealed that *CHI3L1* and *SPP1* signaling was uniquely
580 upregulated in Aβ-associated microglia following lecanemab treatment. Meanwhile, *FAM107A* and *ATP5IF1*
581 were uniquely elevated in Aβ-associated microglia in AN1792-treated brains. Notably, lecanemab more
582 frequently showed enhanced signaling related to lysosomal function, protein degradation, and iron regulation
583 genes, possibly due to the acute response to the drug. Residual Aβ-niches and microglia in both lecanemab
584 and AN1792 samples displayed increased *APOE* and *TREM2* expression and dysregulated complement
585 signaling (increased with lecanemab, decreased in AN1792 subjects with limited Aβ clearance). Both
586 treatments were associated with reductions in HSP coding genes and stress-responsive microglia.

587 Importantly, we found that expression of *APOE* and *TREM2* in microglial-enriched ST spots positively
588 correlated with anti-AN1792 antibody titer and showed a trend toward a negative correlation with Aβ load
589 throughout the brain. This indicates that microglial *APOE* and *TREM2* expression was highest in AN1792
590 subjects who generated a beneficial vaccine response, despite the several years that often elapsed between
591 antibody assays and postmortem examination. We hypothesize that microglial *APOE* and *TREM2* are
592 instrumental in removing Aβ plaques following immunization. Notably, our previous findings demonstrated a
593 significant inverse correlation between Aβ plaque scores and both mean and peak anti-AN1792 antibody

594 titers[12], supporting the hypothesis that anti-Aβ antibodies play a crucial role in clearing Aβ plaques from the
595 brain.

596 Future studies with larger sample sizes and longitudinal designs will be essential to validate and extend
597 these findings, ultimately advancing our understanding of microglial contributions to AD therapies. In parallel,
598 animal models will be critical for dissecting candidate mechanisms, including those involving heat shock
599 proteins and the Fgf2-Fgfr3 signaling axis. Some observed alterations may be unrelated to Aβ clearance,
600 reflecting ongoing tau pathology, vascular Aβ, or immune responses to the antibodies. Inherent effects of APOE
601 genotype or sex likely influence microglial responses and warrant examination in larger cohorts. Limited sample
602 availability constrains our conclusions, although the use of carefully matched pathological controls mitigates
603 some potential biases. Presently, only a small number of lecanemab-treated post-mortem cases have been
604 described in the literature[18, 64], highlighting the rarity of these samples.

605 By applying ST, we have reveal how microglial gene expression varies across distinct anatomical and
606 pathological niches, offering novel insights that would be difficult to achieve with bulk or single-cell methods
607 alone. Leveraging rare human samples, our study provides a crucial step forward in understanding
608 transcriptomic changes induced by immunization in AD. These data offer valuable clues to the mechanisms
609 underlying Aβ clearance and serve as a foundation for interpreting microglial adaptation to therapeutic
610 interventions. Ultimately, defining how microglial states shift following immunization and identifying expression
611 signatures associated with enhanced Aβ clearance can guide the refinement of next-generation therapeutics.
612 With further validation and attention to patient heterogeneity, these insights may lead to more targeted,
613 personalized strategies to improve clinical outcomes in AD.

614 Our findings suggest that targeting microglial ApoE and Trem2 could improve Aβ clearance. In
615 preclinical models, interventions such as small molecules, gene therapies, or biologics that strengthen ApoE-
616 or Trem2-mediated clearance may enhance therapeutic efficacy. Clinical trials targeting Trem2 will clarify
617 whether boosting Trem2 function can slow AD progression. Although ApoE-targeted therapies are less
618 developed, research into gene-editing approaches, ApoE-lowering strategies, and protein-structure modifiers
619 is advancing[65]. As these interventions progress, incorporating insights from our study may help refine patient
620 selection and therapeutic design, driving more personalized and effective treatments. Other candidate genes

we identified, such as *PADI2*, *A2M*, and *RAB13*, were also linked to microglial responses following immunization, yet their function in amyloid clearance remains undetermined.

A key challenge for microglia-targeted therapies is minimizing amyloid-related imaging abnormalities (ARIA), such as edema and microhemorrhages. Avoiding an excessive immune response may require interventions engineered to engage microglia without broadly activating peripheral macrophages. Advanced brain-shuttle technologies could further improve drug delivery across the blood-brain barrier, ensuring precise modulation of ApoE and Trem2 while reducing off-target effects[66]. By combining targeted microglial engagement with controlled drug delivery, future strategies may achieve robust Aβ clearance while limiting ARIA and other adverse events, ultimately improving the safety and efficacy of immunotherapies for AD.

In conclusion, we reveal distinct microglial phenotypes associated with Aβ immunization. These results underscore the critical role of microglia in response to Aβ immunotherapy. Our findings offer novel insights into the underlying microglial mechanisms of Aβ clearance induced by immunization.

Online Methods

Human tissue samples

AN1792 study cohort

Clinical and neuropathological follow-up of AD patients enrolled in the Elan Pharmaceuticals phase I trial of AN1792 was previously reported[1-3]. Patients (or their caretakers) were invited to consent to post-mortem neuropathological examination. Frontal cortex tissue was available from 22 iAD patients, with 16 having a neuropathological diagnosis of AD. The remaining six had a different cause of dementia and were excluded from further analysis. One patient (case 1) required imaging in life, which demonstrated features of meningoencephalitis[4] and neuroradiological features consistent with the later defined ARIA-edema[5]. Notably, three of the 16 AD donors (case 2, 3, 9) were omitted due to low RNA quality scores, leaving a final cohort of 13 iAD samples. With inadequate numbers of post-mortem placebo treated samples from the original AN1792 trial, frontal cortices of 6 nAD cases and 6 NND cases were used as controls. Cases were matched as closely as possible for age at death. In total, post-mortem FFPE frontal cortical samples of 13 iAD (mean age of death = 79.97; range = 63 – 89), 6 nAD controls (mean age of death = 79.60; range = 65 – 89), and 6 NND controls (mean age of death = 74.93, range = 63 – 82) were included in the active immunization analysis. All nAD cases

and 4 NND frontal cortex samples were sourced from Stanford Alzheimer's Disease Research Center. Two additional NND samples were sourced from Northwestern Pathology. Collection of brain tissue was approved by the Institutional Review Board of each university. Relevant clinical and demographic information of iAD, nAD and NND cases are listed in **Extended Data Table 1**. Tissue blocks were cut into 5 µm sections and stored at 4ºC until further use. This study was conducted in compliance with all relevant ethical guidelines and was approved by BRAIN UK (UK Brain Archive Information Network) under REC reference 19/SC/0217 and the Northwestern University Institutional Review Board.

Lecanemab and nAD controls

Clinical[6] and neuropathological[7] findings of the patient who received lecanemab were previously reported. Consent was obtained to perform full-body post-mortem examination and subsequent reporting of the neuropathologic findings related to her receiving anti-Aβ. Multiple foci of cortical histiocytic vasculitis with fibrinoid necrosis in vessels with CAA were present in this patient's brain along with extensive, multi-focal intracerebral hemorrhage. The CAA and necrotizing vasculopathies closely paralleled the intraparenchymal hemorrhages. Multiple foci of histiocytic/microglial reaction to parenchymal amyloid plaques were noted. According to NIA-AA 2012 consensus guidelines[8], the AD neuropathologic changes would be categorized as 'high'. FFPE tissue blocks from the FCX, TCX, PCX, and HIPP of both donors were sectioned into 5 µm slices and stored at 4ºC until further use. The nAD control samples (mean age at death = 69.3 years; range = 62–82) were matched for CAA, AD pathology ('high'), and *APOE* ε4/ε4 genotype. Notably, one nAD donor also had magnetic resonance imaging-positive microbleeds on gradient echo sequences. Relevant clinical and demographic information of lecanemab and nAD cases are listed in **Extended Data Table 1**.

DNA collection and genotyping

Genomic DNA was extracted from residual brain material on glass slides following ST workflow, using the QIAamp DNA FFPE Tissue Kit (catalog #56404, Qiagen, Hilden, Germany), with deparaffinization steps omitted as they were completed during the ST protocol. DNA was isolated from all nAD and NND samples, as well as AN1792 samples 102-19 and 102-20, which lacked *APOE* genotype information. Positive controls were included to validate genotyping. Quality and concentration of extracted DNA were assessed to ensure suitability

for genotyping. *APOE* genotyping for the single nucleotide polymorphisms (SNPs) rs429358 and rs7412 was conducted at the University of Illinois at Chicago Genomics Research Core using the BioMark HD Real-Time PCR system (Fluidigm) and SNP Type assays (rs429358: C___3084793_20; rs7412: C____904973_10; ThermoFisher). Genotyping was performed according to the manufacturer's protocol, with each SNP assayed using TaqMan SNP Genotyping Assays (Applied Biosystems, Foster City, CA, USA). Genotype calling was conducted with the SNP Genotyping Analysis software (Fluidigm) using default analysis parameters: a confidence threshold of 65, global normalization, and K-means clustering. PCR cycle 35 was used for SNP calling, and each sample was analyzed in three technical replicates. No template controls were incorporated into vacant inlets as negative controls. Allele calls were determined based on fluorescence signals from FAM and VIC probes, and each *APOE* haplotype was assigned by combining the alleles of rs429358 and rs7412, resulting in the following classifications: ε2 (T/T), ε3 (T/C), and ε4 (C/C).

ST

FFPE samples were deparaffinized, stained with Hematoxylin & Eosin (H&E), and de-crosslinked according to the Visium CytAssist Spatial Gene Expression for FFPE protocol (CG000520 Rev B, 10x Genomics). H&E-stained tissues were imaged on a EVOS M7000 Imaging System (AMF7000, ThermoFisher Scientific) using a 20x-objective (0.45NA, AMEP4982, ThermoFisher Scientific). Immediately after decrosslinking, libraries were prepared according to the user guide for Visium CytAssist Spatial Gene Expression Reagent Kits (CG000495, Rev E, 10x Genomics). Final libraries were sequenced by the NUSeq Core at Northwestern University Feinberg School of Medicine using the Illumnia Novaseq 6000 or Illumnia NovaSeq X Plus platforms to the recommended depth of 25,000 reads per tissue-covered ST spot. The Space Ranger pipeline version 2.0.0., referencing the GRCh38 human genome (GENCODE v32/Ensembl 98), and Visium Transcriptome Probe Set v2.0 (10x Genomics) were used to process FASTQ files. For precise anatomical context, we conducted manual annotations of each spot of meninges, gray matter layers and white matter structures, utilizing the high-resolution images captured by the EVOS M7000 microscope within the Loupe Browser software (10x Genomics).

Spatial proteogenomics

FFPE samples were deparaffinized, decrosslinked and stained with a combination of DAPI (1:100; #62248; ThermoFisher), rabbit anti-Iba1 (1:250; #019-19741; WAKO) and mouse anti-pan-Aβ (1:250; clone 4G8; #800708; BioLegend). Notably, we used TrueBlack Plus Lipofuscin Autofluorescence Quencher (#23014; Biotum) according to the manufacturer's instructions. Tissues were imaged on a EVOS M7000 Imaging System (AMF7000, ThermoFisher Scientific) using a 20x-objective (0.45NA, AMEP4982, ThermoFisher Scientific, or Olympus Lucplanfl N 20x/0.45 Ph1 UIS2 Collar Fn22). Post imaging, spatial gene and protein expression libraries were immediately prepared according to the user guide for Visium CytAssist Spatial Gene and Protein Expression Reagent Kits (CG000494; Rev B; 10x Genomics). We employed the Visium Human Transcriptome Probe Set version 2.0 for RNA transcript detection, along with the Human FFPE Immune Profiling Panel, which includes a 35-plex CytAssist Panel of antibodies, both intracellular and extracellular, sourced from BioLegend and Abcam for protein detection. This panel also comprises four isotype controls. Final libraries were sequenced as detailed above for spatial transcriptomics. The targeted sequencing depth was 25,000 reads per tissue-covered ST spot for gene expression libraries, and 5,000 reads per tissue-covered spot for protein expression libraries, as recommended.

High-definition ST

FFPE samples were deparaffinized, decrosslinked, and stained with DAPI, rabbit anti-pan-Aβ (1:500, clone D54D2, #8243, Cell Signaling Technology), goat anti-IBA1 (1:100, #ab5076, Abcam), and mouse anti-phospho-Tau (1:250, MN1020, ThermoFisher) according to the Visium HD FFPE Tissue Preparation Handbook (CG000684 Rev A, 10x Genomics). Lipofuscin autofluorescence was quenched with TrueBlack Lipofuscin Quencher. Stained tissues were imaged on an EVOS M7000 Imaging System (AMF7000, ThermoFisher Scientific) using a 20x objective (Olympus Lucplanfl N 20x/0.45 Ph1 UIS2 Collar Fn22). Immediately following decrosslinking, libraries were prepared per the Visium HD Spatial Gene Expression Reagent Kits user guide (CG000685 Rev B, 10x Genomics). Final libraries were sequenced by the NUSeq Core at Northwestern University Feinberg School of Medicine on an Illumina NovaSeq X Plus platform to a target depth of 275 million reads per fully-covered capture area. FASTQ files were processed using the Space Ranger pipeline version 3.0.0, referencing the GRCh38 human genome (GENCODE v32/Ensembl 98) and Visium Transcriptome Probe

Set v2.0 (10x Genomics). For precise anatomical mapping, high-resolution images captured on the EVOS M7000 were annotated in Loupe Browser (10x Genomics) to delineate the hippocampus.

scRNAseq

For each sample, 1-2 consecutive FFPE scrolls of 25 µm were prepared and processed according to the Isolation of Cells from FFPE Tissue Sections for Chromium Fixed RNA Profiling protocol (CG000632, 10x Genomics). After deparaffinization and dissociation by pestle, single cells were hybridized with barcoded probes overnight. GEM generation and library construction were performed as outlined in the Chromium Fixed RNA Profiling Reagent Kits for Multiplexed Samples manual (CG000527; Rev E; 10x Genomics). The first batch included four brain regions—frontal cortex, temporal cortex, parietal cortex, and hippocampus—from one nAD control (NMA22-205) and one lecanemab-treated sample (NMA22-300). The second batch contained the same regions from two additional nAD controls (A14-193 and A11-170). The third batch contained frontal cortex samples from 10 AN1792 samples (102-1, 102-7, 102-8, 102-11, 102-15, 102-16, 102-17, 102-19, 102-21, and 102-22). To enhance cell yield per tissue, samples were split across two barcodes per pool, totaling 16 barcodes. Limited cell numbers in samples 102-7, 102-8, 102-11, and 102-21 restricted them to a single barcode each. We targeted approximately 8,000 cells per barcode, aiming for a total of 16,000 cells per tissue per pool. For batches one and three, two pools were generated, targeting 32,000 cells across both pools for samples with dual barcodes. Cell counts were taken at several stages of the protocol to ensure consistent pooling, using a DAPI stain (1:2000; #62248; ThermoFisher) and imaged with an EVOS M7000 Imaging System (AMF7000, ThermoFisher Scientific) using a 4x objective lens (0.13NA, AMEP4980, ThermoFisher Scientific). The final libraries were indexed and pooled, and then sequenced together by the NUSeq Core at Northwestern University Feinberg School of Medicine on an Illumina NovaSeq X Plus sequencer, aiming for approximately 25,000 reads per cell. Demultiplexed FASTQ files were processed using the Cell Ranger pipeline version 7.2.0, referencing the GRCh38 human genome (GENCODE v32/Ensembl 98), and the Visium Transcriptome Probe Set v2.0 (10x Genomics).

Immunohistochemistry

DAB (3,3'-diaminobenzidine) hematoxylin staining for pan-Aβ (D54D2)

Consecutive sections from the ST data, spaced 5-10 μm apart, were used to stain for pan-Aβ. FFPE sections were heated at 60 ºC for 1 hour, followed by incubation in xylenes and a graded ethanol series. Antigen retrieval was performed at 95ºC for 30 minutes in either citrate buffer pH 6.0 (#64142-08; Electron Microscopy Sciences) or Tris-EDTA pH 9.0 (#AB93684; Abcam). Slides were blocked using 10% normal goat serum (#ab7481; Abcam) in PBS with 0.03% Triton-X (#21568-2500, Acros Organics) for up to 4 hours. The sections were then incubated overnight at 4ºC with the primary antibody for pan-Aβ (1:100; clone D54D2; #8243; Cell Signaling) and subsequently with goat anti-rabbit HRP (1:200, #P0448, Agilent Technologies) for 1 hour at room temperature. Sections were then treated with diluted DAB Chromogen (#K3468, Dako) for 20 minutes at room temperature. Hematoxylin (#51275, Sigma-Aldrich) was used for counterstaining before the sections were dehydrated and mounted with Cytoseal (#8312-4, Epredia).

DAB (3,3'-diaminobenzidine) hematoxylin staining for phosphorylated Tau (AT8)

Non-adjacent serial sections were stained for phosphorylated tau using the AT8 antibody (1:500; Thermo Fisher Scientific #MN1020). FFPE sections were incubated overnight at room temperature with primary antibody, followed by incubation with a biotinylated anti-mouse secondary antibody (Vector Laboratories). Signal was visualized using an avidin-biotin-peroxidase complex (Vectastain Elite, Vector Laboratories) and a chromogenic reaction with DAB (Vector Laboratories). Slides were counterstained with hematoxylin and coverslipped using Expert XTF Mounting Media (CellPath).

Immunofluorescence

FFPE sections were placed in a stove for 1 hour at 60ºC before deparaffinization in xylenes and rehydration with a series of graded ethanol (100%, 100%, 95%, 70%, 50%, each for 10 minutes). Antigen retrieval was performed at 95ºC for 30 minutes in citrate buffer pH 6.0 (#64142-08, Electron Microscopy Sciences) or Tris-EDTA buffer (pH 9.0; #AB93684, Abcam). Slides were blocked using 10% of normal donkey serum (#017-000-121, Jackson ImmunoResearch; #AB7475, Abcam) in PBS with 0.03% Triton-X (#21568-2500, Acros Organics) for up to 4 hours. Sections were then incubated with primary antibodies (**Extended Data Table 1**) overnight at 4ºC, followed by a one-hour incubation in Alexa-fluorophore labeled secondary antibodies (1:400) at room temperature. Primary antibodies used included goat anti-Iba1 (1:150, #ab5076, Abcam), rabbit anti-Aβ (1:1000, clone D54D2, #8243, Cell Signaling), mouse anti-CD68 (1:400, clone KP1, #ab955, Abcam), rabbit

anti-Iba1 (1:400, #019-19741, WAKO), goat anti-APOE (1:500, #ab947, Sigma Aldrich), mouse anti-Aβ (1:1000, clone D3D2N, #15126, Cell Signaling), rabbit anti-TMS1/ASC (1:400, clone RM1049, #ab309497, Abcam), mouse anti-Aβ (1:250, clone 4G8, #800708, BioLegend), rabbit anti-A2M (1:500, clone EPR4432, #ab109422, Abcam), rabbit anti-APOC1 (1:300, clone EPR16813, #ab198288, Abcam), and rabbit anti-SPP1 (1:300, #ab8448, Abcam). Immunofluorescent-stained slides were counterstained for DNA using DAPI (1:5000, #62248, ThermoFisher), followed by quenching of auto-fluorescence with TruBlack Plus (1:40, #23014, Biotium) in PBS. Slides were mounted using ProLong Gold Antifade Mountant (#P36934; Fisher Scientific).

Imaging analysis

Imaging and processing of pan-Aβ DAB stains in consecutive ST images

Tissue imaging was performed with a TissueGnostics slide scanner at the Northwestern University Center for Advanced Microscopy. The acquired images were processed using FIJI software (NIH). Briefly, deconvolution was applied to the images for the hematoxylin and DAB staining. Manual thresholds were set for Aβ reactivity using the DAB stain by a researcher blinded to sample identification. The derived binary signal was further cleaned by removing small particles. Aβ coverage in the gray matter was determined by calculating the ratio of Aβ deposits in the gray matter to the total area of the gray matter per sample. This analysis was performed only in the tissue region that was used for spatial transcriptomics. To construct the expanded Aβ niches, the binary Aβ signal was artificially extended by 100 µm from its original boundary, with a gradual decrease in signal intensity noted every 20 µm. Subsequently, the images were aligned to the CytAssist image using the Loupe browser (version 7.0.1, 10x Genomics) and further integrated with the spatial RNA data using Space Ranger software version 2.1.1. Importantly, ST spots with unreliable Aβ staining, arising from technical issues or tissue anomalies such as folds or holes, were omitted from subsequent Aβ niche analyses.

Imaging and processing of phosphorylated Tau (AT8) DAB stains

Tissue imaging for AT8-stained slides was performed at ×20 magnification using an automated slide scanner microscope (Olympus VS110; Olympus America Inc.) at the Biomedical Imaging Unit, Faculty of Medicine, University of Southampton. The acquired images were processed using FIJI software (NIH). Briefly, deconvolution was applied to separate the hematoxylin and DAB signals. Manual thresholds were set for AT8 reactivity in the DAB channel by a researcher blinded to sample identification. The resulting binary signal was

refined by removing small particles to enhance clarity. AT8 coverage in the gray matter was quantified as the ratio of AT8-positive area to the total gray matter area per sample. This analysis was restricted to the tissue region used for spatial transcriptomics.

Processing of immunofluorescent images for spatial proteogenomics

High-resolution imaging in the spatial proteogenomic workflow was conducted using FIJI software. The DAPI channel was auto-thresholded using the Li vector, with subsequent removal of entities larger than ~1 cm and application of the watershed function to separate binary nuclear masks. The Iba1 channel processing involved dividing the image into a 25 x 25 grid, applying Bleach Correction via Histogram Matching to each segment, reassembling the image, and employing the RollingBall algorithm (radius: 2.8 µm) to reduce background noise. Both Iba1 and Aβ channels underwent manual thresholding, conducted by a researcher blinded to sample identification. Post-binarization, channels were subjected to two rounds of dilation and erosion, followed by a filtering step to remove oversized objects in Aβ and Iba1, targeting noise reduction. The binarized Iba1 masks were then utilized to refine the bleach-corrected Iba1 channel. This refinement was achieved by overlaying the binarized Iba1 mask onto the bleach-corrected Iba1 channel. In this process, only the regions within the confines of the binarized mask were retained, while areas outside the mask were cleared.

Vascular and cortical Aβ were identified in the high-resolution images from the spatial proteogenomic workflow using the LabKit machine learning tool[9] within FIJI. Each sample was analyzed with a unique classifier to generate a vascular Aβ probability map. This map was initially enhanced with despeckling and Gaussian Blur ($\sigma = 4$) to improve smoothness, followed by triple dilation and erosion and filtering to exclude small particles. The probability maps were then manually thresholded by a researcher blinded to sample identification. Observations of vascular Aβ missed by the automated process but detected upon visual inspection were carefully annotated and included. The vascular Aβ binary signal was dilated twice before being extracted from the processed Aβ channel, leaving the residual signal to be identified as cortical Aβ. Expanded Aβ niches were subsequently delineated as described above. For nAD controls A14-193 and A11-170, vascular Aβ was manually annotated instead of using LabKit. Importantly, ST spots exhibiting unreliable Aβ staining, whether due to technical complications or the presence of tissue folds or holes, were excluded from further analyses related to the Aβ niche.

Aβ coverage and Iba1 colocalization

The coverage of cortical or total Aβ within the gray matter was determined by calculating the percentage of the area covered by the binarized cortical or total Aβ mask in the gray matter to the total area of the gray matter for each brain region per donor. To evaluate the association between Iba1^{+} cells and cortical or total Aβ, the area where cortical Aβ and Iba1 colocalized was divided by the total area of cortical or total Aβ present in the gray matter.

Data preprocessing, quality-control and integration

AN1792 RNA for ST

Seurat objects were initialized for each sample with Space Ranger filtered feature barcode matrices using Load10X_Spatial, and raw counts were log-normalized. ST spots with extremely high or low UMI counts or extremely low feature counts were removed on a per-sample basis. Outermost ST slide spots, ST spots with at least 20% mitochondrial expression, and ST spots that were not covering tissue were removed. Raw counts were transformed using SCTransform.

scRNAseq

Background contamination was removed in each sample across all pools using SoupX[10], where the contamination fraction was determined by the autoEstCont function and counts were adjusted via the adjustCounts method, setting the roundToInt parameter to TRUE to return integer counts. Seurat objects for each sample within the pools were created using counts corrected by SoupX. Low-quality cells were removed prior to doublet identification, using a sample and pool-specific minimum UMI threshold of 3 median absolute deviations below the median and a minimum feature threshold of 2 median absolute deviations below the median. Additionally, cells exhibiting mitochondrial gene expression above 20% were removed. Doublet identification was performed with DoubletFinder utilizing 10 principal components, a pN setting of 0.25, and a pool-specific predicted doublet rate determined based on the average number of cells loaded per probe barcode, with a 0.4% undetectable multiplet rate for 825 cells loaded per barcode as per the Chromium Fixed RNA Profiling Reagent Kits for Multiplexed Samples manual (CG000527; Rev E; 10x Genomics). Doublets

were removed, and samples from AN1792 donors 102-1, 102-16, 102-17, 102-19, and 102-22 were retained, while donors 102-7, 102-8, 102-11, and 102-21 were excluded due to high contamination fractions, low UMI counts, or high mitochondrial expression. The remaining raw counts were further processed with SCTransform while adjusting for mitochondrial gene expression. Fifty principal components were derived from the SCTransform-processed data, which was then harmonized across both pools and samples using the IntegrateLayers function with the HarmonyIntegration approach. Lastly, UMAP visualization was constructed from 30 integrated features.

Lecanemab RNA for ST

Seurat objects were initialized for each sample with Space Ranger filtered feature barcode matrices using Load10X_Spatial, and raw counts were log-normalized. ST spots with extremely high or low UMI counts or extremely low feature counts were removed on a per-sample basis. ST spots with at least 20% mitochondrial expression were removed for FCX, TCX and PCX, and ST spots with at least 30% mitochondrial expression were removed for HIPP. ST spots not located on cortical or hippocampal tissue were excluded. Outermost ST slide spots, and ST spots with zero protein expression were removed. Raw counts were transformed using SCTransform.

Lecanemab spatial protein analysis

For each sample, Seurat objects were created from Space Ranger's filtered feature barcode matrices, which included isotype-normalized counts, via the Load10X_Spatial function. Isotype control antibodies were excluded for the further analysis. ST spots subjected to quality control exclusion were the same as those identified in the RNA assay, as previously detailed.

High-definition ST analysis

Nuclei segmentation was performed using StarDist[57], with expression data from Space Ranger 2x2 µm filtered feature barcode matrices assigned to segmented nuclei. Nuclei with fewer than 10 UMI counts or over 20% mitochondrial expression were excluded. Raw counts were transformed with SCTransform, producing 50 principal components based on the SCTransform data. Integration across samples was achieved with

IntegrateLayers using the HarmonyIntegration method, and a UMAP was generated using 30 integrated features.

snRNAseq integration and reference generation

A snRNAseq dataset[39, 40] from the Religious Orders Study and Rush Memory and Aging Project (ROSMAP)[67] was used to generate a reference atlas for ST data. We initially identified 5,000 feature genes using the 'FindVariableFeatures' function from the 'Seurat' package per batch. From this pool of genes, we selected 5,000 common feature genes across all datasets for anchor identification using the 'FastFindAnchors' function from the 'FastIntegration' package[12]. Notably, 'FastFindAnchors' employs a method similar to that of the 'Seurat' package but with enhanced efficiency and reduced memory usage. The identified anchors were then used for batch correction via the 'FastIntegration' function. The resulting batch-corrected values were subsequently employed for downstream analyses, including Principal Component Analysis, UMAP, and clustering. For annotation of broad cell types, we utilized the feature genes identified during the integration stage. Subsequently, within each broad cell type, we re-selected feature genes and conducted similar analyses to delineate detailed subtypes. Major cell-types used were astrocytes, endothelial cells, stromal cells, immune cells, oligodendrocytes, oligodendrocyte precursor cells, interneurons, and excitatory neurons. We then randomly down-sampled 2,000 cells per cell-type, or included all cells for categories with fewer than 2,000 cells, resulting in a reference dataset of 34,695 cells. For meningeal ST spots, we utilized a focused subset of this atlas, comprising stromal cells, peripheral immune cells, and endothelial cells.

Cell type annotation

scRNAseq

Clustering was conducted in Seurat by first applying the FindNeighbors function with 30 integrated features, followed by FindClusters at multiple resolutions, with a final resolution of 1 used to define initial clusters. To identify immune subtypes, the data was subsetted to clusters expressing immune markers. Data from different cohorts was merged, and raw counts were transformed using SCTransform with mitochondrial expression regressed out. Fifty principal components were generated from the SCTransform data, and integration across cohorts was performed using IntegrateLayers with the CCA integration method. Clustering was refined by

reapplying FindNeighbors and FindClusters with 30 integrated features, defining immune clusters at a resolution of 0.35. A UMAP was generated using the 30 integrated features.

Aβ-niches

Data from all cohorts was subsetted to include cortical Aβ-rich spots in gray matter. Raw counts were transformed using SCTransform, and 50 principal components were generated from SCTransform data. Integration across samples was conducted using IntegrateLayers with the HarmonyIntegration method. A UMAP was generated with 30 integrated features, followed by clustering with Seurat's FindNeighbors and FindClusters functions across various resolutions. Final clusters were defined at a resolution of 0.4.

High-definition ST

Clustering in Visium HD data was conducted in Seurat using FindNeighbors with 30 integrated features, followed by FindClusters across multiple resolutions, with final clusters defined at a resolution of 0.2.

ST deconvolution

For spatial deconvolution, we utilized the Cell2Location (v0.1.3) package[38]. Gene filtering on the reference data was conducted using the filter_genes function, with parameters set to cell_count_cutoff=5, cell_percentage_cutoff2=0.03, and nonz_mean_cutoff=1.12. The batch_key parameter was configured as sequencing batch for the snRNAseq atlas and sample ID for the scRNAseq atlas, with each sample ID corresponding to a specific brain region (e.g., the same donor had a distinct sample ID for each brain region). The reference regression model was trained for 500 epochs for the reference atlas and 750 epochs for our in-house-created scRNAseq immunization atlas to stabilize the evidence lower bound loss. The ROSMAP frontal cortex snRNAseq atlas was used to deconvolute ST spots across all regions, while our in-house-created scRNAseq immunization atlas was used to deconvolute ST spots in gray matter. The proportion of genes expressed per spot (CDR) was calculated from raw counts and standardized. ST spots were deconvoluted using the resulting reference signatures, with standardized CDR as a continuous covariate and sample ID as the batch key in the Cell2Location model. The model was trained in batches of 2500 ST spots over 1000 epochs to stabilize the evidence lower bound loss. To account for technical variability in RNA detection sensitivity, the detection_alpha parameter was set to 20, and the N_cells_per_location parameter was set to 7 based on

manual cell counts of several ST spots. The 5% quantile of the posterior distribution was computed directly and used for downstream analysis.

Defining cell-type-enriched ST spots

To identify ST spots enriched for specific cell types, we applied cell type-specific region restrictions and thresholds to Cell2Location predictions, with enrichment defined separately for each sample. For cell types from the snRNAseq reference atlas, ST spots enriched for fibroblasts, pericytes, peripheral immune cells, smooth muscle cells, and endothelial cells were annotated when enrichment scores for a given ST spot were in the top 1% of gray and white matter or the top 5% of meningeal spots. Microglia and astrocytes were considered enriched in the top 5% of gray and white matter. Interneuron enrichment was defined in the top 5% of gray matter, while MYO16 excitatory neurons were enriched in the top 1% of gray matter. Oligodendrocyte precursor cells were enriched in the top 5% of both gray and white matter, and oligodendrocytes were considered enriched in the top 30% of white matter. Enrichment for layer-specific neurons was determined within the relevant cortical layers:f L2/3 excitatory neurons in the top 10% of layers II-III, L4 excitatory neurons in the top 50% of layer IV, L4/5 excitatory neurons in the top 15% of layers IV-VI, and L5, L5/6, L5/6 CCa, and L5/6 CCb excitatory neurons in the top 5% of layers V-VI. Layer I was excluded from enrichment analysis for all cell types in the snRNAseq atlas.

For microglia clusters from our in-house scRNAseq immunization atlas, enrichment was defined by a sample-specific Cell2Location prediction threshold set at three standard deviations above the mean in gray matter ST spots.

Definition of Aβ enrichment groups

ST spots were classified as Aβ-rich if the coverage within the expanded Aβ niche, indicated by barcode fluorescence intensity, exceeded a threshold of 183. This threshold was visually confirmed using Loupe Browser software (10x Genomics). The Aβ niche was defined to include Aβ-rich ST spots along with their first- and second-order spatial neighbors, based on array coordinates, covering an approximate radius of 200 µm. ST spots containing CAA pathology, as well as spots immediately adjacent to those, were excluded from the cortical Aβ niche.

DEG analysis

To identify DEGs across various regions of interest within our datasets, we employed two distinct DE techniques: DESeq2[14] and MAST[15]. Each approach was adapted to suit the specific characteristics and requirements of the comparison, considering the nature of the data (pseudobulk for DESeq2 and single-cell for MAST) and the level at which covariates were standardized (sample-level for DESeq2 and spot-level for MAST). Covariate selection was guided by variance partition analysis, which identified gDNA as the primary driver of variance after the experimental group. Additionally, we accounted for the number of genes expressed in a subset of ST spots or cells to control for differences in quality and sequencing depth. Finally, sex and age were included due to their known effects on immune responses in AD.

DESeq2

DESeq2 was initiated by subsetting the data for ST spots within the region of interest. Continuous covariates at the sample level, including age, average nFeatures within subsampled ST spots, and gDNA percentage, were standardized within each ROI by subtracting the mean and dividing by the standard deviation. We then filtered out genes not expressed in at least 1% of either comparison group based on raw counts, excluding genes starting with RPS, RPL, MT, or HB. Pseudobulk data was created by summing raw counts by donor to facilitate a more robust differential expression analysis. The DESeq2 analysis was conducted with the inclusion of covariates such as sex, age, average features within subsampled ST spots, and gDNA percentage, all of which were standardized, if continuous. DEG significance thresholds were set at an adjusted *P*-value of 0.05 and a log2 fold change of ± log2(1.5).

MAST

For MAST, data was subsetted to include only the ST spots or cells of interest. Sample-specific downsampling was applied to ensure that no single sample contributed more than 50% of ST spots or cells within a comparison group, that the fold difference in total ST spots or cells between comparison groups did not exceed three, and that each group contained no more than 3,000 ST spots or cells. Continuous covariates at the spot level, including age, the CDR from recorrected SCT data, and gDNA percentage per sample, were standardized within each subset of ST spots or cells. We applied PrepSCTFindMarkers on the region of interest (ROI), which

re-corrects SCTransform counts to normalize sequencing depth across samples. SCT data (log1p-transformed SCT counts) was then extracted from the Seurat object. Genes prefixed with RPS, RPL, MT, or HB were excluded, and additional filtering was performed based on percent expression within comparison groups. Genes were tested if they were expressed in 1% of both groups and in 10% of either group using SCT expression data, except for Visium HD data, where genes were tested if expressed in 1% of either group. Log2 fold-change between comparison groups for the remaining genes was calculated using the Seurat FoldChange function. MAST was run with covariates such as sex, age, CDR, gDNA percentage, brain region, and manually annotated regions or cortical layers, all of which were standardized if continuous. Sample ID was included as a random effect for comparisons involving multiple samples. MAST hurdle *P*-values were adjusted using the Benjamini-Hochberg method. Log fold-change from the prior calculation was appended to the results, with significance thresholds for differential expression set at an adjusted *P*-value of 0.05 and a log fold-change (LFC) of ± log2(1.5).

DEP analysis

Data was first subset for the region of interest, and CDR (calculated based on isotype-normalized counts) was standardized within the region of interest by subtracting the mean and dividing by the standard deviation. A negative binomial generalized linear model was employed through Seurat's FindMarkers function for differential expression analysis on isotype-normalized counts, setting min.pct to 0.01, logfc.threshold to -Inf, and standardized CDR and manually annotated regions or cortical layers as latent variables. Raw *P*-values were adjusted using the Benjamini-Hochberg method, and proteins were considered significant DEPs with adjusted *P*-value less than 0.05 and magnitude of average log-fold change greater than log2(1.5).

Marker expression defining cell types or Aβ niche types

SCTransform-corrected counts were re-corrected using PrepSCTFindMarkers, with log-transformed (log1p) corrected counts utilized in analyses. To delineate general cluster markers, the FindMarkers function facilitated the identification of positive marker genes through a "one vs. many" comparative approach, testing genes expressed in more than 25% of the cluster of interest (set to 1% for Visium HD), setting only.pos to TRUE, employing the default Wilcoxon rank-sum test. Genes prefixed with RPS, RPL, MT, or HB were excluded from testing. Marker gene selection was based on Benjamini-Hochberg adjusted *P*-values below 0.05. For the

specific analysis of positive and negative markers within cortical Ab niche cluster 6, FindMarkers was used to compare cluster 6 against all others, allowing for both positive and negative marker detection (only.pos = FALSE), with min.pct set to 0.1 and logfc.threshold set to -Inf, using the default Wilcoxon test. Genes with prefixs RPS, RPL, MT, or HB were excluded. Marker genes were deemed significant if they presented an adjusted *P*-value under 0.05 and an average log fold-change exceeding log2(1.5).

Gene set enrichment analysis

Human Molecular Signatures Database

Gene lists were analyzed using the enrichR package[68] with the hallmark gene set collection from the Human Molecular Signatures Database. For lists containing specifically downregulated genes, combined scores were negated. A significance threshold was set at a Benjamini-Hochberg adjusted *P*-value of 0.05.

Microglia states

Signed probability fold change was calculated for each gene as the product of the negative logarithm of the adjusted *P*-value and the log2 fold-change. Enrichment for human microglial activation states[40, 48] was assessed using the fgsea package, with probability fold change as the ranking metric. Custom gene sets associated with various microglial activation states were compiled from the supplementary materials provided in the referenced studies. Normalized enrichment scores (NES) were calculated, and significance was determined through permutation testing, with *P*-values adjusted using the Benjamini-Hochberg method. A threshold of 0.05 was applied for adjusted *P*-values, with no specific cut-off for the magnitude of NES values.

LOESS trajectory analysis

LOESS was employed to identify non-linear patterns of gene expression across the Ab niche separately for each group. SCTransform counts were re-adjusted through PrepSCTFindMarkers, with the logarithm of one plus the corrected counts (log1p) serving as the basis for our analysis. Predictions were generated for all genes in the SCT assay. A LOESS regression of span 0.75 was fit to each gene within each group using the loess function of the R stats package. Predicted expression values were scaled and centered within each group. The predicted expression trajectories across the Ab niche were then subdivided into clusters, employing hierarchical clustering through the hclust function in the R stats package.

Quantification and statistical analysis

Statistical analyses were predominantly conducted using R version 4.2.3. Graphpad Prism version 10.2.1 was used for analyses specific to microscopy measurements and the comparison of relative abundances of scRNAseq-derived cell types and microglia clusters, and Aβ niche clusters. For quality-control metrics on the sample level, we first applied Shapiro–Wilk test and F tests to evaluate normality and variance equality, informing the selection of appropriate statistical tests. The chosen tests included the unpaired two-tailed Student's t-test, with or without Welch's correction for unequal variance, as needed, and the Mann–Whitney test for non-parametric data. For comparisons of relative abundances (scRNAseq-derived cell-types, microglia clusters, and Aβ niche clusters), a paired t-test was utilized. Across all analyses, a *P*-value threshold of less than 0.05 was set to denote statistical significance.

ShinyCell

ShinyCell is an R package designed to efficiently create interactive Shiny-based web applications for visualizing fundamental analyses of RNA sequencing data. Our adapted ShinyCell app enables users to explore spatial gene expression patterns on a UMAP, with spatial regions and the quantified degree of Aβ per ST spot linked as metadata. Additionally, users can conduct comparative analyses of gene and protein expression across different groups using violin/box plots and access supplementary built-in analytical tools.

Data availability

Spatial RNA and single-cell RNA-seq data have been deposited at GEO under accession numbers GSE263038, GSE263034, GSE263079, and GSE282928. Any additional information required to reanalyze the data reported in this work paper is available from the lead contact upon request. Data can be explored and requested through a central hub located at: https://sites.google.com/view/adimmunization/home.

Code availability

All code used to generate the figures in this study can be found at https://github.com/gatelabNW/AD_Immunization.

Acknowledgements

We thank David Bennett (Rush University) for early access to the ROSMAP snRNAseq dataset. We thank Sherry Hsiang-Yi Chou, Nicholas Reish, Diptaman Chatterjee and Dimitri Krainc (Northwestern University) for helpful discussion. We also thank Benton Veire (10x Genomics) for assistance with spatial proteogenomics. We also thank the staff members of the Stanford and Northwestern Alzheimer's Disease Research Centers for their assistance acquiring nAD and NND control brain tissues under National Institutes of Health P30AG066515 and P30AG072977, respectively. Finally, we thank David Kirchenbuechler and Ching Man Wai (Northwestern University) for their support. Some figures were created using BioRender.com. ROSMAP is supported by P30AG10161, P30AG72975, R01AG15819, R01AG17917, U01AG46152, and U01AG61356. ROSMAP resources can be requested at https://www.radc.rush.edu and www.synpase.org. Tissue samples from patients enrolled in the AN1792 clinical trial were provided by the University Hospital Southampton NHS Foundation Trust through BRAIN UK, with support from Brain Tumour Research, the British Neuropathological Society, and the Medical Research Council. This work was supported by Northwestern University's Center for Advanced Microscopy and a Cancer Center Support Grant (NCI CA060553) and NUSeq Core Facility, Alzheimer Nederland Impulssubsidie grant WE.06-2023-03 (L.v.O.), Alzheimer Nederland Early Career grant WE.03-2023-08 (L.v.O.), National Institute of Neurologic Disease and Stroke K99/R00 Pathway to Independence award NS112458 (D.G.), Bright Focus Foundation A2023003S (D.G.), Alzheimer's Association 23AARG-1026607 (D.G.) and a National Institutes of Aging R01AG078713 (D.G.).

Author information

L.v.O. conducted ST, scFRP, confocal imaging, led the study and wrote the manuscript. B.S., A.J.E., J.B., N.S., T.K., and J.K assisted with ST, histology and scFRP. A.V.F. led bioinformatics analysis under guidance from L.v.O. N.S., B.M.R.A., Z.Z., L.C., M.L. H.X. and T.W. assisted with bioinformatics analysis. J.L.N. assisted with histology. P.J. and R.J.C. contributed brain tissue samples from the lecanemab case. J.A.R.N. and D.B. provided brain samples from the AN1792 trial. P.J., J. Cahan, R.V., J. Chen, J.A.R.N. and D.B. assisted with study design. D.G. conceptualized, funded and led the study and edited the manuscript.

Ethics declarations

AN1792 tissue

This study was conducted in compliance with all relevant ethical guidelines and was approved by BRAIN UK (UK Brain Archive Information Network) under REC reference 19/SC/0217.

ROSMAP data

All ROSMAP participants enrolled without known dementia and agreed to detailed clinical evaluation and brain donation at death[67]. Both studies were approved by an Institutional Review Board of Rush University Medical Center (ROS IRB# L91020181, MAP IRB# L86121802). Both studies were conducted according to the principles expressed in the Declaration of Helsinki. Each participant signed an informed consent, Anatomic Gift Act, and an RADC Repository consent (IRB# L99032481) allowing their data and biospecimens to be repurposed.

Lecanemab tissue

The study of de-identified tissue was approved by Institutional Review Board of Northwestern University (exempt IRB #00219860).

Competing interests

J.A.R.N. has been a consultant/advisor relating to AD immunization programs for: Elan Pharmaceuticals, GlaxoSmithKline, Novartis, Roche, Janssen, Pfizer, Biogen and Eisai and D.B. for Elan Pharmaceuticals and Biogen. D.G. has been a consultant/advisor relating to AD therapies for Merck. They have no financial interest in relation to AD immunotherapy.

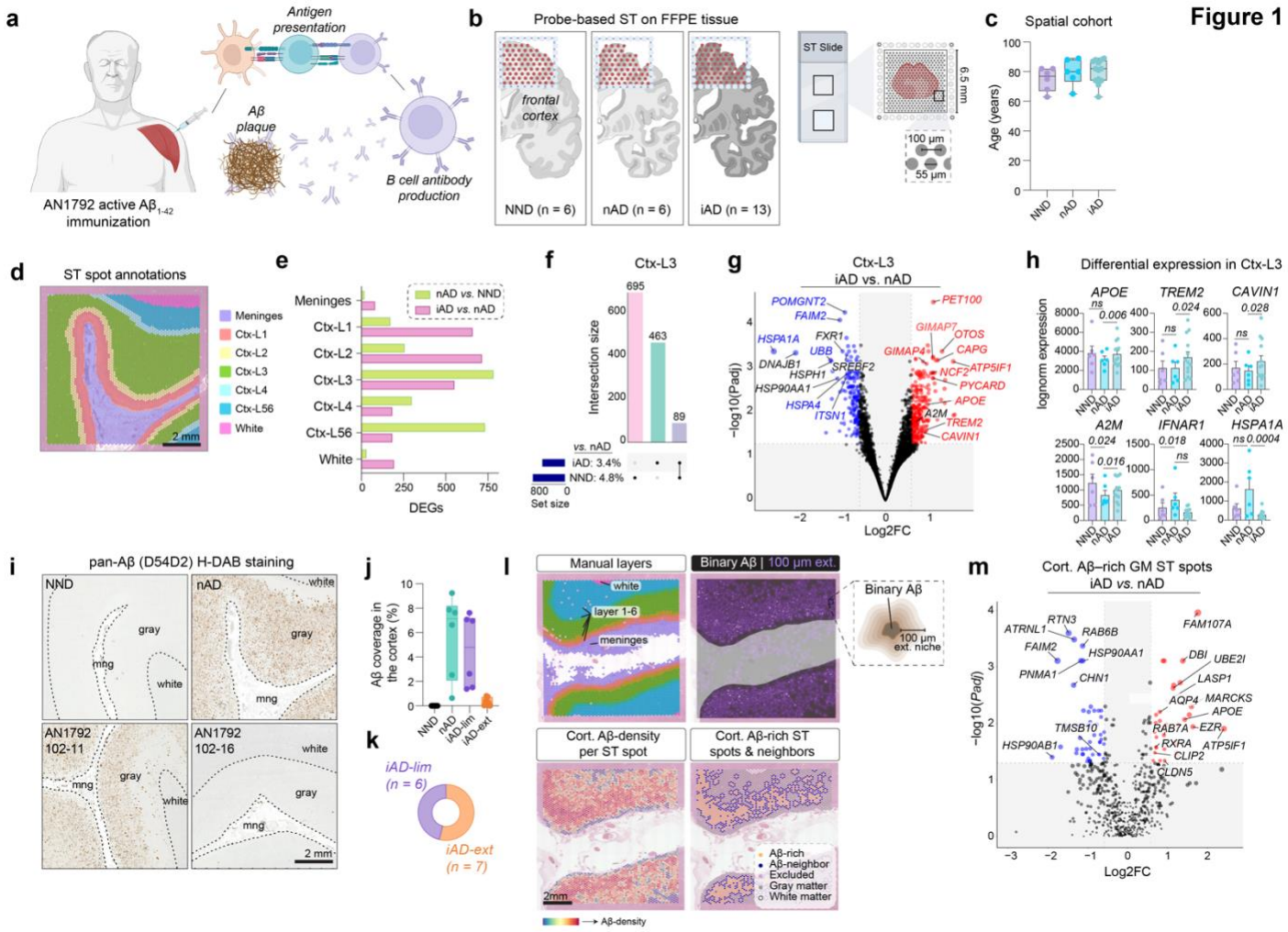
Figure 1
a
Antigen presentation
Aβ plaque
B cell antibody production
AN1792 active Aβ1-42 immunization
b
Probe-based ST on FFPE tissue
frontal cortex
NND (n = 6)
nAD (n = 6)
iAD (n = 13)
ST Slide
6.5 mm
100 µm
55 µm
c
Spatial cohort
Age (years)
NND
nAD
iAD
d
ST spot annotations
Meninges
Ctx-L1
Ctx-L2
Ctx-L3
Ctx-L4
Ctx-L56
White
2 mm
e
nAD vs. NND
iAD vs. nAD
DEGs
f
Ctx-L3
Intersection size
695
463
89
vs. nAD
iAD: 3.4%
NND: 4.8%
Set size
g
Ctx-L3
iAD vs. nAD
−log10(Padj)
Log2FC
POMGNT2
FAIM2
HSPA1A
FXR1
UBB
DNAJB1
HSPH1
SREBF2
HSP90AA1
HSPA4
ITSN1
PET100
GIMAP7
OTOS
GIMAP4
CAPG
NCF2
ATP5IF1
PYCARD
APOE
A2M
TREM2
CAVIN1
h
Differential expression in Ctx-L3
APOE
TREM2
CAVIN1
A2M
IFNAR1
HSPA1A
lognorm expression
ns
0.006
0.024
0.028
0.016
0.018
0.0004
i
pan-Aβ (D54D2) H-DAB staining
NND
nAD
AN1792 102-11
AN1792 102-16
gray
white
mng
2 mm
j
Aβ coverage in the cortex (%)
NND
nAD
iAD-lim
iAD-ext
k
iAD-lim (n = 6)
iAD-ext (n = 7)
l
Manual layers
Binary Aβ | 100 µm ext.
white
layer 1-6
meninges
Binary Aβ
100 µm ext. niche
Cort. Aβ-density per ST spot
Cort. Aβ-rich ST spots & neighbors
Aβ-rich
Aβ-neighbor
Excluded
Gray matter
White matter
2mm
Aβ-density
m
Cort. Aβ–rich GM ST spots
iAD vs. nAD
−log10(Padj)
Log2FC
ATRNL1
RTN3
RAB6B
FAIM2
HSP90AA1
PNMA1
CHN1
FAM107A
DBI
UBE2I
LASP1
AQP4
MARCKS
APOE
TMSB10
RAB7A
EZR
RXRA
ATP5IF1
HSP90AB1
CLIP2
CLDN5
n
Cort. Aβ–rich GM ST spots
iAD−lim vs. nAD LFC
iAD−ext vs. nAD LFC
Upregulated
ATP5IF1
FAM107A
PBXIP1
MARCKS
GLUL
APOE
EZR
RAB7A
CD74
LASP1
A2M
SNCB
B2M
GNAO1
NR2F1
HSP90AA1
RTN1
NELL2
ATRNL1
SREBF2
GRIA1
Padj < 0.05; LFC ± log2(1.5)
unique DEG iAD−lim vs. nAD
unique DEG iAD−ext vs. nAD
shared DEG
o
Nonlinear Gene Expression in Cort. Aβ–rich GM ST spots and 200 µm Radius in iAD
SCTransform Expression (Z-Score Standardization)
Cluster 1: 3466 Genes
Cluster 2: 1030 Genes
Cluster 3: 1645 Genes
Cluster 4: 1768 Genes
Cluster 5: 3111 Genes
Cluster 6: 1545 Genes
Cluster 7: 1494 Genes
Cluster 8: 771 Genes
Cluster 9: 788 Genes
Cluster 10: 424 Genes
Cluster 11: 1554 Genes
Cluster 12: 375 Genes
Aβ-density
Aβ-rich
p
enrichR MSigDB Analysis: LOESS Clusters
Complement
Epithelial Mesenchymal Transition
Angiogenesis
Coagulation
Myogenesis
KRAS Signaling Up
Androgen Response
p53 Pathway
TNF−alpha Signaling via NF−kB
Inflammatory Response
Adipogenesis
Hypoxia
IL−2/STAT5 Signaling
UV Response Up
mTORC1 Signaling
−log10(Padj)
Clusters with Padj < 0.05 pathways
Cluster 1
Cluster 3
Cluster 4
Combined Score
q
Cluster 4
SCTransform Expression (Z-scored LogNormalized)
nAD
iAD−lim
iAD−ext
Aβ-density
Aβ-rich
r
Cluster 4 Single Genes
A2M
APOE
C3
FAM107A
RAB13
SPP1
SCTransform Expression
nAD
iAD-lim
iAD-ext
Aβ-density
Aβ-rich

1151

1152 **Fig. 1: Active Aβ immunization drives a microglial response to Aβ. a**, AN1792 active Aβ-immunization. **b**,
1153 ST method and group sizes of NND, nAD and iAD frontal cortex tissues. **c**, Study demographics indicating age
1154 of each subject. **d**, Manually annotated ST spots in the frontal cortex. **e**, Barplots showing the number of DEGs
1155 for each comparison per manually-annotated area. **f**, UpSet plot showing unique and shared DEGs across
1156 group comparisons in cortical layer III. **g**, Volcano plot depicting DEGs in cortical layer III (iAD vs. nAD). Red
1157 and blue DEGs are uniquely identified in the iAD vs. nAD comparison and are not observed as DEGs in the
1158 nAD vs. NND comparison. **h**, Bar graphs of pseudobulked expression for *APOE*, *TREM2*, *CAVIN1*, *A2M*,
1159 *IFNAR1*, and *HSPA1A* in microglia-enriched ST spots in gray matter. Error bars indicate SEM. *P*-values are
1160 derived from DESeq2. **i**, Representative pan-Aβ H-DAB stains for each group. **j**, Quantification of cortical Aβ
1161 coverage per group. **k**, Numbers of iAD-lim and iAD-ext subjects among AN1792 actively immunized subjects.
1162 **l**, Images depicting processing of Aβ IHC images. The binary Aβ signal was extended by 100 μm beyond its
1163 actual size, with a gradual decrease in signal intensity every 20 μm. This allowed for dection of genes
1164 associated with Aβ density. **m**, Volcano plot showing DEGs from Aβ-rich gray matter ST spots (iAD vs. nAD).
1165 **n**, Plot showd DEGs (iAD-lim vs. nAD; iAD-ext vs. nAD) for Aβ-rich ST spots. **o**, LOESS plots showing clusters
1166 of non-linear gene expression patterns relative to Aβ density in iAD. **p**, Pathway enrichment analysis of genes
1167 in non-linear expression clusters associated with Aβ density in iAD. **q**, LOESS plot of cluster 4 predictions in
1168 nAD (top), iAD-lim (middle), and iAD-ext (bottom) relative to Aβ density. **r**, LOESS plots of selected genes in
1169 LOESS cluster 4. A2M, alpha-2-macroglobulin; APOE, apolipoprotein E; CAVIN1, caveolae-associated protein
1170 1; Ctx, cortex; DEGs, differentially expressed genes; GM, gray matter; HSPA1A, heat shock protein family A
1171 member 1A; H-DAB, Hematoxylin-3,3'-Diaminobenzidine; iAD, immunized Alzheimer's disease; iAD-ext,
1172 immunized with extensive Aβ clearance; iAD-lim, immunized with limited Aβ clearance; IFNAR1, interferon
1173 alpha and beta receptor subunit 1; IHC, immunohistochemistry; LFC, log fold-change; LOESS, locally
1174 estimated scatterplot smoothing; MSigDB, Molecular Signatures Database; NND, non-neurologic disease;
1175 nAD, non-immunized Alzheimer's disease; *P*-adj, *P*-value adjusted; SEM, standard error of the mean; ST,
1176 spatial transcriptomics; TREM2, triggering receptor expressed on myeloid cells 2.
1177
1178
1179

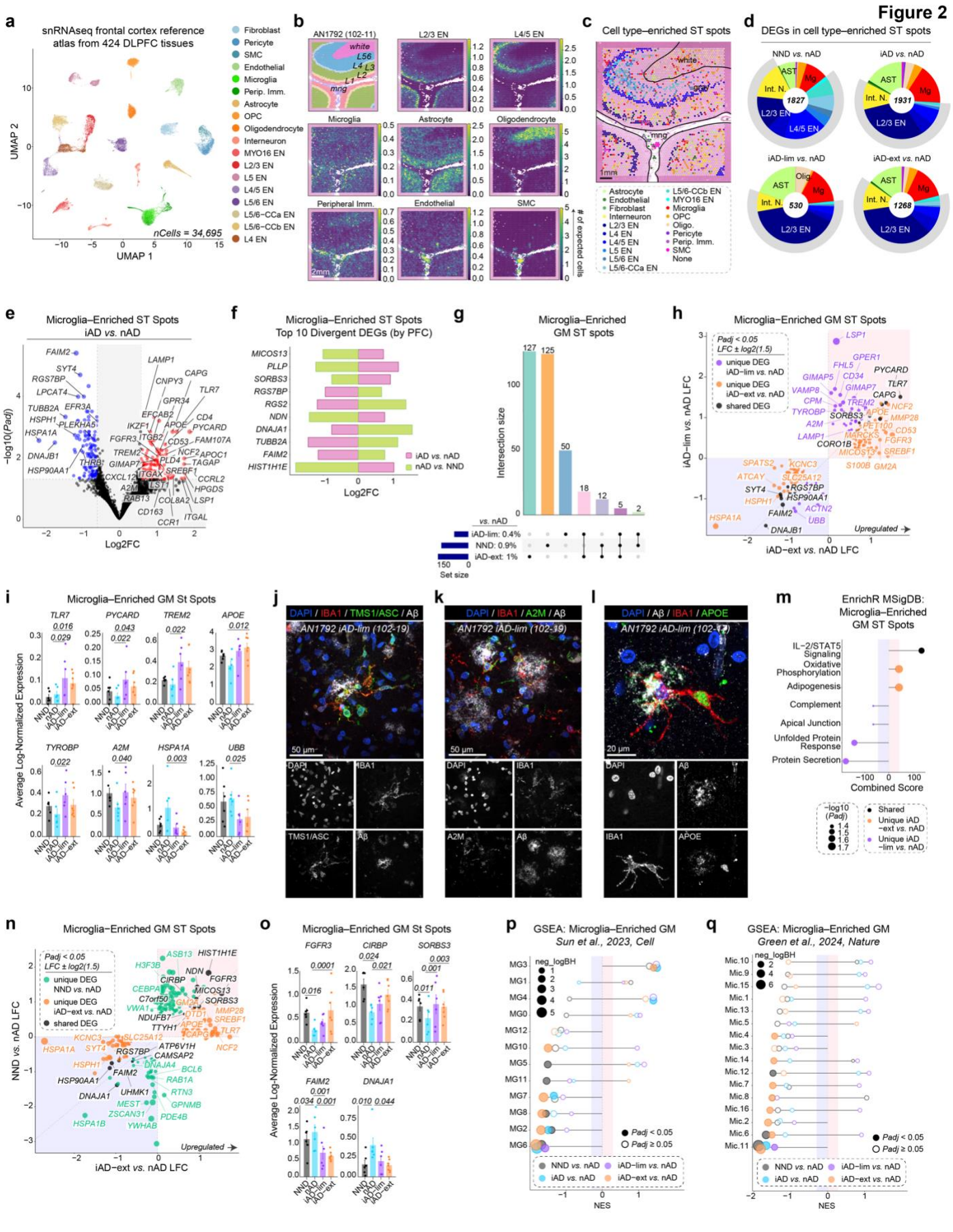

Fig. 2: Inflammatory and neuroprotective microglial responses distinguish levels of Aβ clearance in

1182 **actively immunized AD patient brains. a**, UMAP of the reference atlas using DLPFC snRNA-seq data[39, 40].
1183 **b**, Spatial plots showing the abundance of deconvoluted cell types. **c**, Spatial plots highlighting enriched ST
1184 spots for each deconvoluted cell type. **d**, Pie charts depicting the percentage of DEGs expressed in enriched
1185 ST spots per cell type: NND vs. nAD (top left), iAD vs. nAD (top right), iAD-lim vs. nAD (bottom left), and iAD-
1186 ext vs. nAD (bottom right). The number in the center of each pie chart represents the total number of DEGs for
1187 the respective comparison. **e**, Volcano plot of DEGs from microglia-enriched ST spots (iAD vs. nAD). **f**, Bar plot
1188 of the top 10 divergent DEGs in microglia-enriched ST spots based on PFC, comparing iAD vs. nAD and nAD
1189 vs. NND. **g**, UpSet plot showing unique and shared DEGs in microglia-enriched ST spots in gray matter across
1190 groups compared to nAD. **h**, LFC plots for microglia-enriched ST spots in gray matter (iAD-lim vs. nAD; iAD-
1191 ext vs. nAD). **i**, Bar graphs of pseudobulked expression for *TLR7*, *PYCARD*, *TREM2*, *APOE*, *TYROBP*, *A2M*,
1192 *HSPA1A*, and *UBB* in microglia-enriched ST spots in gray matter. Error bars show SEM. *P*-values are derived
1193 from DESeq2. **j-l**, Confocal images showing **j**, TMS1/ASC^{+}Iba1^{+} myeloid cells; **k**, A2M^{+}Iba1^{+} myeloid cells; and
1194 **l**, APOE^{+}Iba1^{+} myeloid cells around Aβ deposits in the frontal cortex of iAD. **m**, Pathway enrichment analysis
1195 of unique and shared DEGs in microglia-enriched gray matter ST spots (iAD-lim vs. nAD; iAD-ext vs. nAD). **n**,
1196 LFC plots for microglia-enriched ST spots in gray matter (NND vs. nAD; iAD-ext vs. nAD). **o**, Bar graphs of
1197 pseudobulked expression for *FGFR3*, *CIRBP*, *SORBS3*, *FAIM2*, and *DNAJA1* in microglia-enriched ST spots
1198 in gray matter. Error bars show SEM. *P*-values are from DESeq2. **p-q**, Pathway enrichment analysis of
1199 predefined microglial states from **p**, Sun et al., 2023, and **q**, Green et al., 2024, using genes ranked by PFC in
1200 iAD-lim vs. nAD and iAD-ext vs. nAD. A2M, alpha-2-macroglobulin; APOE, apolipoprotein E; Ast, astrocyte;
1201 CIRBP, cold-inducible RNA-binding protein; DEGs, differentially expressed genes; DLPFC, dorsolateral
1202 prefrontal cortex; EN, excitatory neuron; FAIM2, Fas apoptotic inhibitory molecule 2; FGFR3, fibroblast growth
1203 factor receptor 3; GM, gray matter; GSEA, gene set enrichment analysis; HSPA1A, heat shock protein family
1204 A member 1A; iAD, immunized Alzheimer's disease; iAD-ext, immunized with extensive Aβ clearance; iAD-lim,
1205 immunized with limited Aβ clearance; Iba1, ionized calcium-binding adapter molecule 1; Int. N., interneuron; L,
1206 Layer; LFC, log fold-change; Mg, microglia; nAD, non-immunized Alzheimer's disease; NND, non-neurologic
1207 disease; *P*-adj, *P*-value adjusted; Perip. Imm., peripheral immune cells; PFC, probabilistic fold change;
1208 PYCARD, PYD and CARD domain containing; SEM, standard error of the mean; SORBS3, sorbin and SH3
1209 domain containing 3; ST, spatial transcriptomics; TLR7, toll-like receptor 7; TMS1/ASC, apoptosis-associated

1210 speck-like protein containing a CARD; TYROBP, TYRO protein tyrosine kinase-binding protein; UBB, ubiquitin

1211 B; UMAP, uniform manifold approximation and projection.

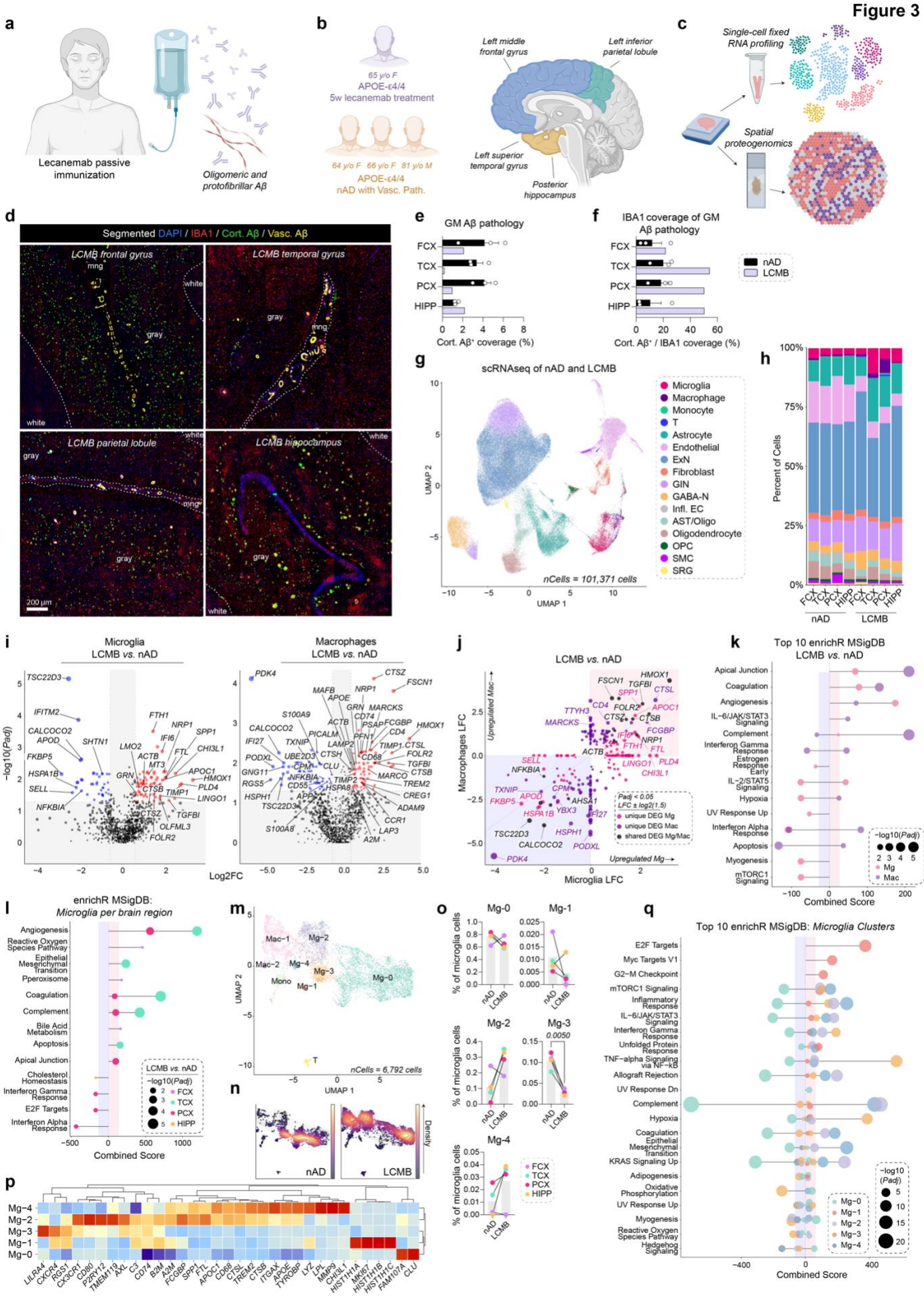
Figure 3
a
Lecanemab passive immunization
Oligomeric and protofibrillar Aβ
b
65 y/o F
APOE-ε4/4
5w lecanemab treatment
64 y/o F 66 y/o F 81 y/o M
APOE-ε4/4
nAD with Vasc. Path.
Left middle frontal gyrus
Left inferior parietal lobule
Left superior temporal gyrus
Posterior hippocampus
c
Single-cell fixed RNA profiling
Spatial proteogenomics
d
Segmented DAPI / IBA1 / Cort. Aβ / Vasc. Aβ
LCMB frontal gyrus
LCMB temporal gyrus
LCMB parietal lobule
LCMB hippocampus
200 µm
e
GM Aβ pathology
Cort. Aβ⁺ coverage (%)
f
IBA1 coverage of GM Aβ pathology
Cort. Aβ⁺ / IBA1 coverage (%)
nAD
LCMB
g
scRNAseq of nAD and LCMB
nCells = 101,371 cells
UMAP 1
UMAP 2
Microglia
Macrophage
Monocyte
T
Astrocyte
Endothelial
ExN
Fibroblast
GIN
GABA-N
Infl. EC
AST/Oligo
Oligodendrocyte
OPC
SMC
SRG
h
Percent of Cells
nAD
LCMB
i
Microglia LCMB vs. nAD
Macrophages LCMB vs. nAD
−log10(Padj)
Log2FC
j
LCMB vs. nAD
Macrophages LFC
Microglia LFC
Upregulated Mac
Upregulated Mg
Padj < 0.05
LFC ± log2(1.5)
unique DEG Mg
unique DEG Mac
shared DEG Mg/Mac
k
Top 10 enrichR MSigDB
LCMB vs. nAD
Combined Score
−log10(Padj)
Mg
Mac
l
enrichR MSigDB:
Microglia per brain region
LCMB vs. nAD
−log10(Padj)
FCX
TCX
PCX
HIPP
Combined Score
m
nCells = 6,792 cells
UMAP 1
UMAP 2
n
nAD
LCMB
Density
o
Mg-0
Mg-1
Mg-2
Mg-3
Mg-4
% of microglia cells
0.0050
FCX
TCX
PCX
HIPP
p
q
Top 10 enrichR MSigDB: Microglia Clusters
Combined Score
−log10 (Padj)
Mg-0
Mg-1
Mg-2
Mg-3
Mg-4

1213 **Fig. 3: Microglial transcriptomic alterations associated with Aβ clearance in an AD patient treated with**
1214 **lecanemab**. **a**, Lecanemab binds oligomeric and protofibrillar Aβ to promote Aβ clearance from the brain. **b**,
1215 Study subjects included a 65-year-old female AD patient treated with lecanemab and three nAD controls: a 64-
1216 year-old female AD patient, a 66-year-old female AD patient, and an 81-year-old male AD patient, all with CAA
1217 and AD pathology, and *APOE* ε4/ε4 genotype. Tissues analyzed included cortical areas and hippocampus. **c**,
1218 Tissues were analyzed by scRNAseq and spatial proteogenomics. **d**, Representative confocal images showing
1219 segmented Aβ burden and microgliosis in regions of the lecanemab-treated patient's brain. A random forest
1220 ensemble learning algorithm was used to distinguish cortical from vascular Aβ. **e**, Percentage of cortical Aβ
1221 coverage in brain regions from lecanemab case and nAD controls. **f**, Percentage of cortical Aβ covered by Iba1.
1222 **g**, UMAP showing annotated cell-types. **h**, Barplot showing percentages of each cell-type for each brain region
1223 between nAD controls and lecanemab case. **i**, Volcano plot of DEGs in microglia (left) and macrophages (right)
1224 comparing lecanemab to nAD. **j**, LFC plots comparing DEGs in microglia and macrophages (lecanemab vs.
1225 nAD). **k**, Pathway enrichment analysis (top 10) of DEGs in microglia and macrophages (lecanemab vs. nAD).
1226 **l**, Pathway enrichment analysis of DEGs in microglia from FCX, TCX, PCX, and HIPP (lecanemab vs. nAD).
1227 **m**, Clustering of microglia from scRNAseq of the lecanemab case and nAD controls. **n**, UMAP density plots
1228 showing microglial cluster distribution for the lecanemab case and nAD controls. **o**, Percentages of microglial
1229 clusters in the lecanemab case vs. nAD controls. **p**, Marker genes for each microglial cluster. **q**, Pathway
1230 enrichment analysis (top 10) of marker genes defining microglial states. AD, Alzheimer's disease; APOE,
1231 apolipoprotein E; AST, astrocyte; CAA, cerebral amyloid angiopathy; Cort., cortical; DEGs, differentially
1232 expressed genes; ExN, excitatory neuron; FCX, frontal cortex; GABA-N, GABAergic neuron; GIN, GABA-ergic
1233 interneuron; HIPP, hippocampus; Iba1, ionized calcium-binding adapter molecule 1; Infl. EC, inflamed
1234 endothelial cells; LCMB, lecanemab; LFC, log fold-change; Mac, macrophages; Mg, microglia; mng, meninges;
1235 MSigDB, Molecular Signatures Database; nAD, non-immunized Alzheimer's disease; Oligo, oligodendrocyte;
1236 OPC, oligodendrocyte precursor cell; *P*-adj, *P*-value adjusted; PCX, parietal cortex; scRNAseq, single-cell fixed
1237 RNA sequencing; SMC, smooth muscle cell; SRG, stress-responsive glia cells; TCX, temporal cortex; UMAP,
1238 uniform manifold approximation and projection; Vasc, vascular.

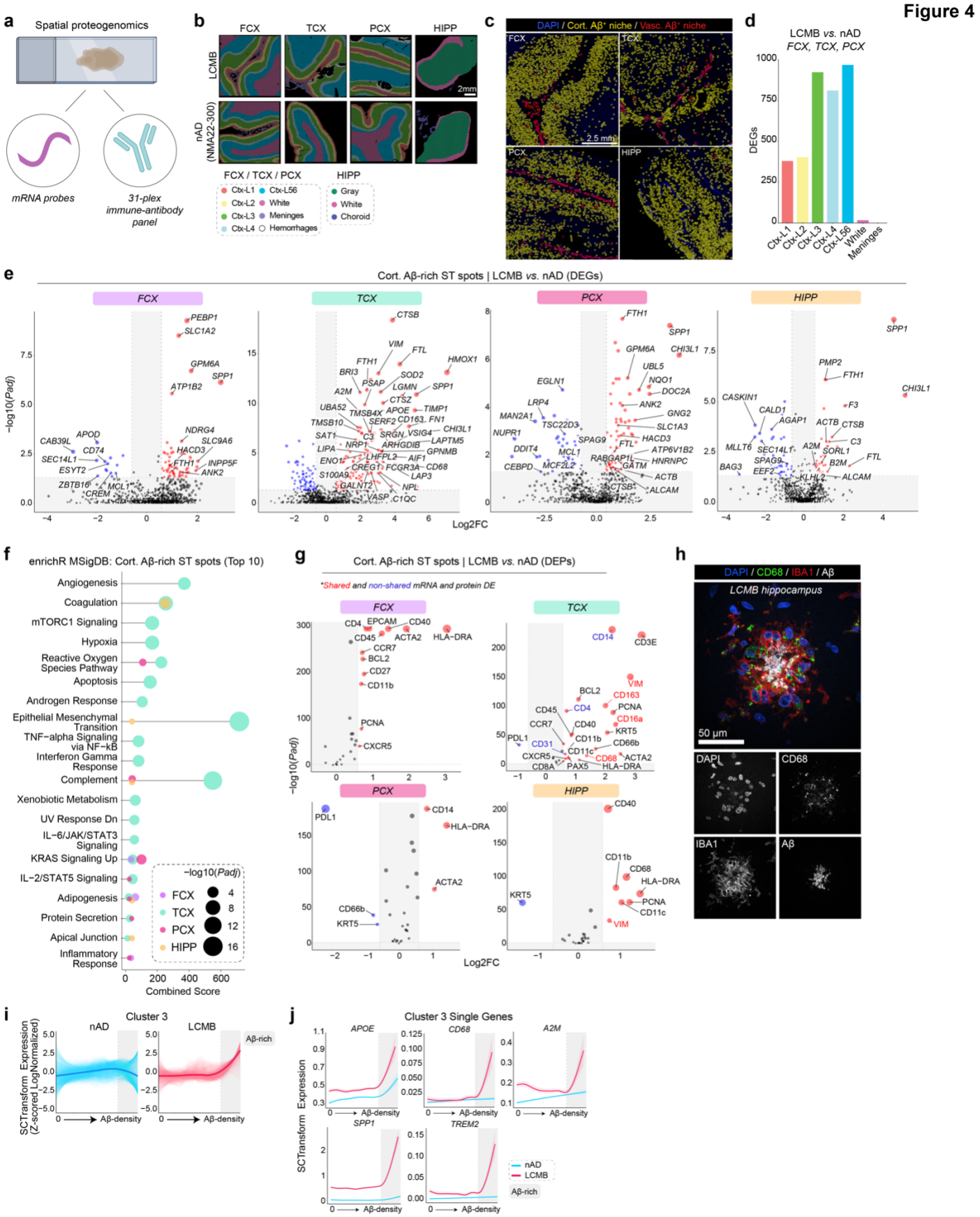

Fig. 4: Microglia recruited to the Aβ niche upregulate *SPP1* following lecanemab treatment. **a**, Proteogenomics allowed for the simultaneous profiling of RNA and protein from lecanemab-treated and nAD

1242 controls. **b**, Manual annotations of brain regions analyzed. **c**, Representative images showing distinction of
1243 segmented cortical and vascular Aβ in brain regions from the lecanemab case. **d**, Bar plots showing the number
1244 of DEGs for each comparison across manually annotated areas. **e**, Volcano plot of DEGs from Aβ-rich gray
1245 matter ST spots (lecanemab vs. nAD) in FCX (top left), TCX (top right), PCX (bottom left), and HIPP (bottom
1246 right). **f**, Top 10 pathway enrichment analysis of DEGs in Aβ-rich gray matter ST spots for each brain region
1247 (lecanemab vs. nAD). **g**, DEPs associated with cortical Aβ ST spots from each brain region (lecanemab vs.
1248 CAA control), with red indicating shared DEGs, blue indicating no shared DEGs, and black indicating low
1249 expression levels not meeting DEG criteria. **h**, Confocal images showing $CD68^{+}Iba1^{+}$ myeloid cells surrounding
1250 Aβ deposits in the hippocampus of the lecanemab-treated patient. **i**, LOESS plot of cluster 3 predictions in nAD
1251 (left) and lecanemab (right) relative to Aβ density. **j**, LOESS plots of selected genes in LOESS cluster 3. CAA,
1252 cerebral amyloid angiopathy; CD68, cluster of differentiation 68; Cort., cortical; DEGs, differentially expressed
1253 genes; DEP, differentially expressed protein; DEPs, differentially expressed proteins; FCX, frontal cortex; HIPP,
1254 hippocampus; Iba1, ionized calcium-binding adapter molecule 1; LCMB, lecanemab; LOESS, locally estimated
1255 scatterplot smoothing; MSigDB, Molecular Signatures Database; nAD, non-immunized Alzheimer's disease; *P*-
1256 adj, *P*-value adjusted; PCX, parietal cortex; ST, spatial transcriptomics; TCX, temporal cortex; Vasc., vascular.

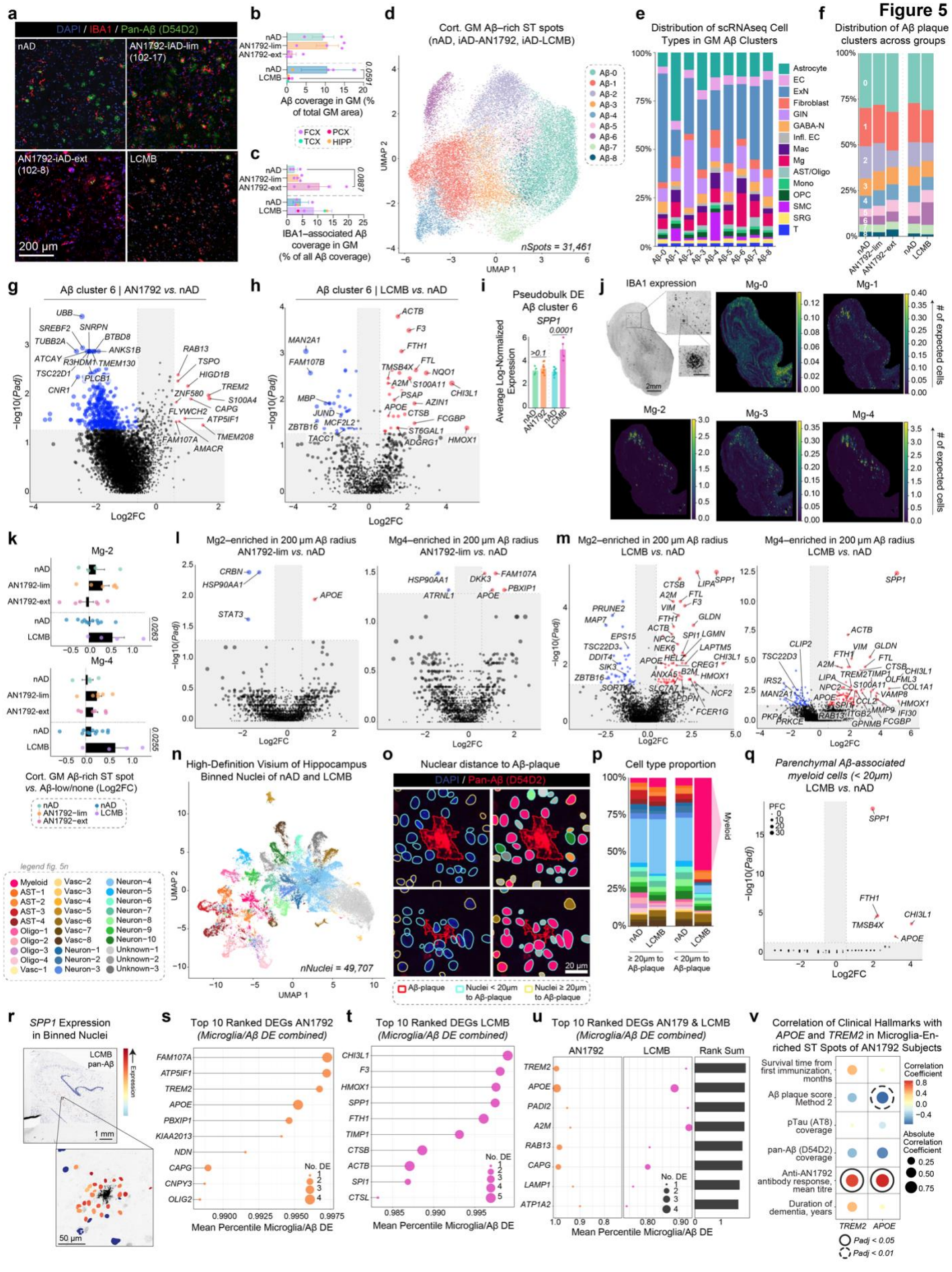
Figure 5
a
DAPI / IBA1 / Pan-Aβ (D54D2)
nAD
AN1792-iAD-lim (102-17)
AN1792-iAD-ext (102-8)
LCMB
200 µm
b
Aβ coverage in GM (% of total GM area)
FCX
PCX
TCX
HIPP
c
IBA1–associated Aβ coverage in GM (% of all Aβ coverage)
d
Cort. GM Aβ–rich ST spots (nAD, iAD-AN1792, iAD-LCMB)
UMAP 1
UMAP 2
nSpots = 31,461
e
Distribution of scRNAseq Cell Types in GM Aβ Clusters
Astrocyte
EC
ExN
Fibroblast
GIN
GABA-N
Infl. EC
Mac
Mg
AST/Oligo
Mono
OPC
SMC
SRG
T
f
Distribution of Aβ plaque clusters across groups
g
Aβ cluster 6 | AN1792 vs. nAD
Log2FC
h
Aβ cluster 6 | LCMB vs. nAD
i
Pseudobulk DE Aβ cluster 6
SPP1
Average Log-Normalized Expression
j
IBA1 expression
Mg-0
Mg-1
Mg-2
Mg-3
Mg-4
# of expected cells
k
Mg-2
Mg-4
Cort. GM Aβ-rich ST spot vs. Aβ-low/none (Log2FC)
l
Mg2–enriched in 200 µm Aβ radius AN1792-lim vs. nAD
Mg4–enriched in 200 µm Aβ radius AN1792-lim vs. nAD
m
Mg2–enriched in 200 µm Aβ radius LCMB vs. nAD
Mg4–enriched in 200 µm Aβ radius LCMB vs. nAD
n
High-Definition Visium of Hippocampus Binned Nuclei of nAD and LCMB
nNuclei = 49,707
legend fig. 5n
o
Nuclear distance to Aβ-plaque
DAPI / Pan-Aβ (D54D2)
20 µm
Aβ-plaque
Nuclei < 20µm to Aβ-plaque
Nuclei ≥ 20µm to Aβ-plaque
p
Cell type proportion
Myeloid
≥ 20µm to Aβ-plaque
< 20µm to Aβ-plaque
q
Parenchymal Aβ-associated myeloid cells (< 20µm) LCMB vs. nAD
r
SPP1 Expression in Binned Nuclei
LCMB pan-Aβ
Expression
1 mm
50 µm
s
Top 10 Ranked DEGs AN1792 (Microglia/Aβ DE combined)
Mean Percentile Microglia/Aβ DE
t
Top 10 Ranked DEGs LCMB (Microglia/Aβ DE combined)
u
Top 10 Ranked DEGs AN179 & LCMB (Microglia/Aβ DE combined)
AN1792
LCMB
Rank Sum
v
Correlation of Clinical Hallmarks with APOE and TREM2 in Microglia-Enriched ST Spots of AN1792 Subjects
Survival time from first immunization, months
Aβ plaque score Method 2
pTau (AT8) coverage
pan-Aβ (D54D2) coverage
Anti-AN1792 antibody response, mean titre
Duration of dementia, years
Correlation Coefficient
Absolute Correlation Coefficient
Padj < 0.05
Padj < 0.01

1257

1258 **Fig. 5: Transcriptomics reveals a shared microglial gene signature between active and passive Aβ**
1259 **immunization. a**, Representative confocal images showing pan-Aβ and Iba1 in frontal cortex brain regions of
1260 nAD, AN1792-lim, AN1792-ext, and lecanemab-treated subjects. **b**, Percentage of cortical Aβ coverage in
1261 cortical and hippocampal regions of AN1792, nAD, and the lecanemab case. **c**, Percentage of cortical Aβ
1262 covered by Iba1 in cortical and hippocampal regions of AN1792, nAD, and the lecanemab case. **d**, Clustering
1263 of Aβ-rich cortical gray matter spots based on gene expression. **e**, Bar plots showing Cell2Location predictions
1264 of scRNAseq cell types in different Aβ plaque clusters. **f**, Percentages of Aβ-rich clusters in AN1792, nAD, and
1265 the lecanemab case. **g-h**, Volcano plots of DEGs in Aβ-rich cluster 6: **g**, AN1792 vs. nAD; **h**, lecanemab vs.
1266 nAD. **i**, Bar graphs showing pseudobulked *SPP1* expression in Aβ-rich cluster 6. Error bars indicate SEM. *P*-
1267 values are from DESeq2. **j**, Spatial plots showing the abundance of deconvoluted scRNAseq microglia types;
1268 scale bar: 100 μm. **k**, Bar plots showing log2 fold-change in predicted abundance of deconvoluted scRNAseq
1269 microglia types in Aβ-rich ST spots versus the rest in AN1792, nAD, and the lecanemab case. **l-m**, Volcano
1270 plots of DEGs from Mg2-enriched (left) and Mg4-enriched (right) ST spots: **l**, AN1792 vs. nAD; **m**, lecanemab
1271 vs. nAD. **n**, UMAP showing annotated binned nuclei from a high-definition Visium assay. **o**, Spatial plots
1272 indicating the distance of nuclei to D54D2-stained Aβ plaques (left) and their annotations (right). **p**, Bar plot
1273 showing the percentage of each cell type in the high-definition Visium assay at ≥ 20 μm (left) and < 20 μm
1274 (right) from Aβ plaques in nAD and the lecanemab case. q, Volcano plot of DEGs from myeloid nuclei within <
1275 20 μm of Aβ plaques (lecanemab vs. nAD). **r**, Spatial plots showing *SPP1* expression in binned nuclei around
1276 Aβ plaques in the lecanemab hippocampus. **s-t**, Top 10 upregulated response DEGs ranked by the average
1277 percentile across microglia and Aβ DE: **s**, in AN1792; **t**, in lecanemab. **u**, Top 10 combined response genes to
1278 AN1792 and lecanemab by summing average percentiles of gene ranks. **v**, Covariate-adjusted Spearman
1279 correlation between *TREM*2 and *APOE* expression in microglia-enriched gray matter ST spots from AN1792
1280 subjects and clinical hallmarks. Aβ, amyloid-beta; AN1792-ext, AN1792 immunized with extensive Aβ
1281 clearance; AN1792-lim, AN1792 immunized with limited Aβ clearance; APOE, apolipoprotein E; AST, astrocyte;
1282 Cort., cortical; DE, differential expression; DEGs, differentially expressed genes; EC, endothelial cells; ExN,
1283 excitatory neuron; FCX, frontal cortex; GABA-N, GABAergic neuron; GIN, GABAergic interneuron; GM, gray
1284 matter; HIPP, hippocampus; Iba1, ionized calcium-binding adapter molecule 1; Infl. EC, inflamed endothelial
1285 cells; LCMB, lecanemab; Mac, macrophages; Mg, microglia; Mono, monocytes; nAD, non-immunized

Alzheimer's disease; Oligo, oligodendrocyte; OPC, oligodendrocyte precursor cell; P-adj, P-value adjusted; PCX, parietal cortex; scRNAseq, single-cell fixed RNA sequencing; SEM, standard error of the mean; SMC, smooth muscle cell; SRG, stress-responsive glia; ST, spatial transcriptomics; TCX, temporal cortex; TREM2, triggering receptor expressed on myeloid cells 2; UMAP, uniform manifold approximation and projection; Vasc., vascular.

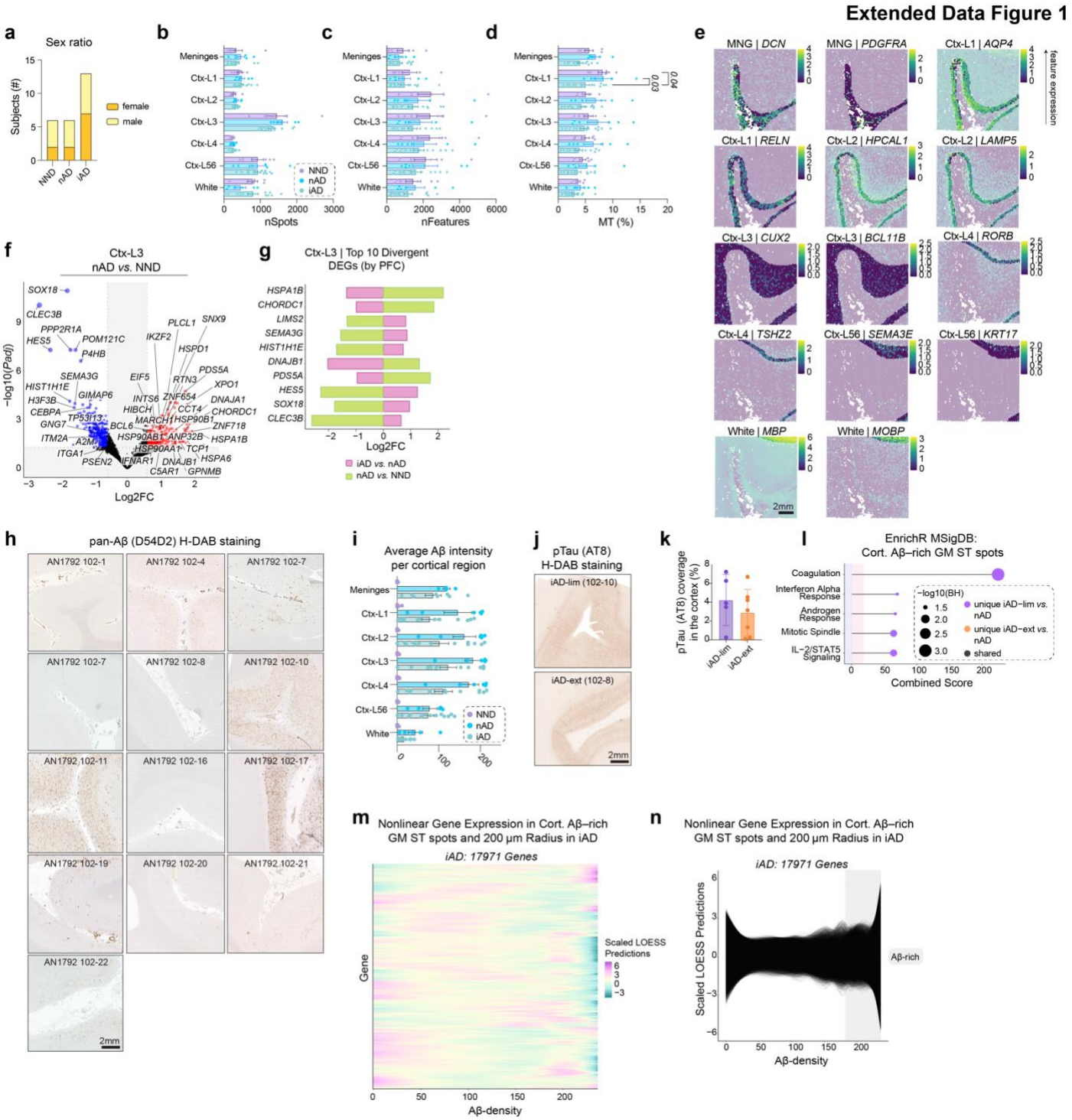

Extended Data Fig. 1: Active Aβ immunization drives a microglial response to Aβ. a, Sex distribution per

1293 group. **b**, Number of ST spots per manually annotated area per donor for all groups. **c**, Average number of
1294 features (genes) per spot per manually annotated area per donor for all groups. **d**, Percentages of mitochondrial
1295 gene expression per spot averaged per manually annotated area per donor for all groups. **e**, Spatial plots
1296 showing expression of brain region-specific genes overlaid on corresponding manually annotated areas
1297 (shaded). **f**, Volcano plot of DEGs in cortical layer III (nAD vs. NND). **g**, Bar plot of the top 10 divergent DEGs
1298 in cortical layer III based on PFC, comparing iAD vs. nAD and nAD vs. NND. **h**, Pan-Aβ (D54D2) H-DAB
1299 staining for AN1792-immunized subjects. **i**, Quantification of average Aβ intensity per cortical region per donor
1300 per group. **j**, Representative pTau (AT8) H-DAB staining for each group. **k**, Quantification of cortical AT8 per
1301 group. **l**, Pathway enrichment analysis of unique and shared DEGs in Aβ-rich gray matter ST spots (iAD-lim vs.
1302 nAD; iAD-ext vs. nAD). **m**, LOESS heatmap showing non-linear gene expression patterns relative to Aβ density
1303 in iAD. **n**, LOESS non-linear trajectories relative to Aβ density in iAD. Aβ, amyloid-beta; AN1792-ext, AN1792
1304 immunized with extensive Aβ clearance; AN1792-lim, AN1792 immunized with limited Aβ clearance; DEGs,
1305 differentially expressed genes; FCX, frontal cortex; GM, gray matter; H-DAB, Hematoxylin-3,3'-
1306 Diaminobenzidine; iAD, immunized Alzheimer's disease; LCMB, lecanemab; LOESS, locally estimated
1307 scatterplot smoothing; MSigDB, Molecular Signatures Database; MT, mitochondrial; nAD, non-immunized
1308 Alzheimer's disease; nFeatures, number of features; nSpots, number of spatial transcriptomic spots; NND,
1309 non-neurologic disease; *P*-adj, *P*-value adjusted; PFC, probabilistic fold change; pTau, phosphorylated tau; ST,
1310 spatial transcriptomics.

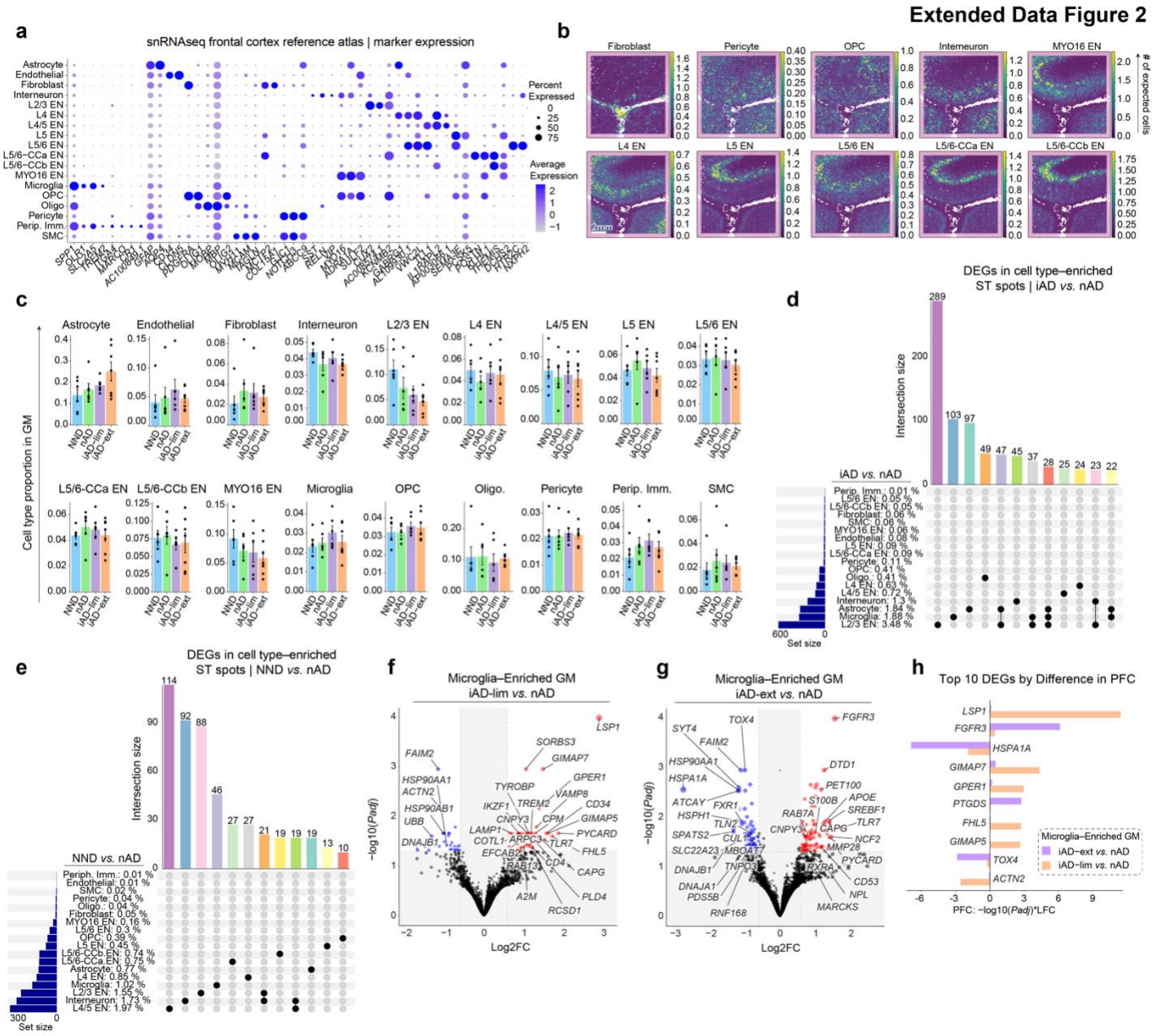

Extended Data Fig. 2: Inflammatory and neuroprotective microglial responses distinguish levels of Aβ clearance in actively immunized AD patient brains. a, Bubble plot heatmap showing top markers expressed by cell types in the reference atlas[39, 40]. **b**, Spatial plots displaying the abundance of deconvoluted cell types. **c**, Bar graphs showing the proportion of deconvoluted cell types in gray matter per donor, per group. **d**, UpSet plot indicating unique and shared DEGs in deconvoluted cell types for iAD vs. nAD. **e**, UpSet plot showing unique and shared DEGs in deconvoluted cell types for NND vs. nAD. **f-g**, Volcano plot of DEGs in microglia-enriched spots in: **f**, iAD-lim vs. nAD; and **g**, iAD-ext vs. nAD. **h**, Bar plot of the top 10 most divergent DEGs in microglia-enriched ST spots based on PFC, comparing iAD-lim vs. nAD and iAD-ext vs. nAD. Aβ, amyloid-beta; AD, Alzheimer's disease; AN1792-ext, AN1792 immunized with extensive Aβ clearance; AN1792-lim, AN1792

1321 immunized with limited Aβ clearance; DEGs, differentially expressed genes; DLPFC, dorsolateral prefrontal
1322 cortex; EN, excitatory neuron; GM, gray matter; iAD, immunized Alzheimer's disease; L, layer; LCMB,
1323 lecanemab; nAD, non-immunized Alzheimer's disease; NND, non-neurologic disease; oliog., oligodendrocyte;
1324 OPC, oligodendrocyte precursor cell; *P*-adj, *P*-value adjusted; periph. imm., peripheral immune cell; PFC,
1325 probabilistic fold change; SEM, standard error of the mean; SMC, smooth muscle cell; snRNA-seq, single-
1326 nucleus RNA sequencing; ST, spatial transcriptomics.

Extended Data Figure 3

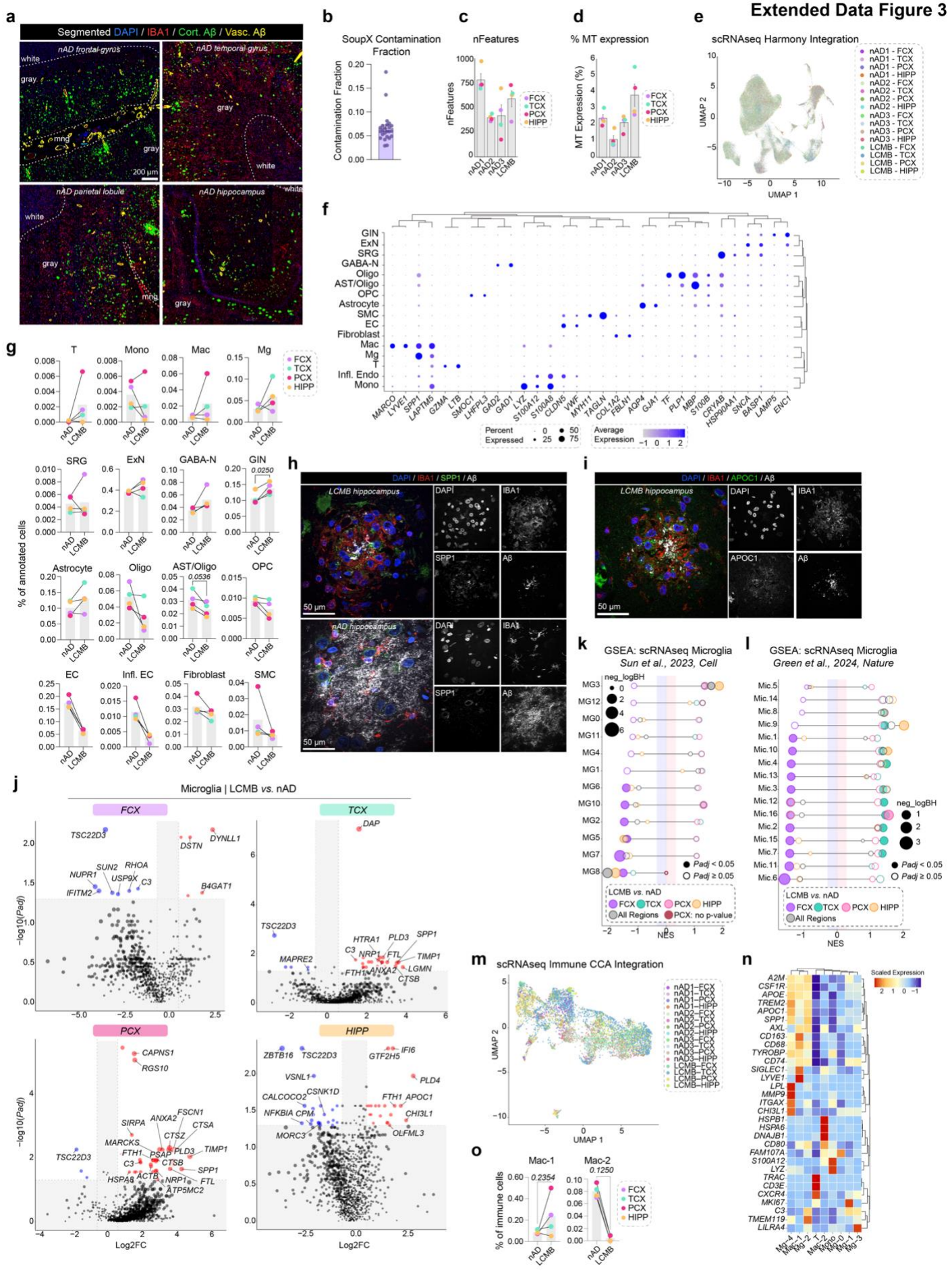

1327

1328 **Extended Data Fig. 3: Microglial transcriptomic alterations associated with Aβ clearance in an AD**
1329 **patient treated with lecanemab**. **a**, Representative confocal images showing segmented Aβ burden and
1330 microgliosis in regions of the nAD control patient's brain. A random forest ensemble learning algorithm was
1331 used to distinguish cortical from vascular Aβ. **b**, SoupX contamination fraction for each scRNAseq sample. **c**,
1332 Average number of features (genes) per cell per donor. **d**, Percentages of mitochondrial gene per cell averaged
1333 per donor. **e**, Integrated scRNAseq dataset showing all analyzed cells from nAD controls and lecanemab case.
1334 **f**, Bubble plot heatmap of top markers expressed by cell types in the scRNAseq dataset. **g**, Changes in
1335 percentages of total annotated cells for each cell type. **h**, Confocal images showing $SPP1^{+}Iba1^{+}$ myeloid cells
1336 surrounding Aβ deposits in the hippocampus of the lecanemab-treated patient, absent in the nAD control. **i**,
1337 Confocal images showing $APOC1^{+}Iba1^{+}$ myeloid cells surrounding Aβ deposits in the hippocampus of the
1338 lecanemab-treated patient. **j**, Volcano plot of DEGs from scRNAseq microglia (lecanemab vs. nAD) in FCX (top
1339 left), TCX (top right), PCX (bottom left), and HIPP (bottom right). **k-l**, Pathway enrichment analysis of predefined
1340 microglial states from **k**, Sun et al., 2023, and **l**, Green et al., 2024, using genes ranked by PFC in scRNAseq
1341 regional microglia (lecanemab vs. nAD). **m**, UMAP showing reintegrated scRNAseq immune cells for each
1342 brain region in the lecanemab case and nAD controls. **n**, Marker genes for each immune cell cluster. **o**,
1343 Percentages of each macrophage cluster. Aβ, amyloid-beta; AD, Alzheimer's disease; APOC1, apolipoprotein
1344 C1; AST, astrocyte; CCA, canonical correlation analysis; DEGs, differentially expressed genes; EC, endothelial
1345 cells; ExN, excitatory neuron; FCX, frontal cortex; GABA-N, GABAergic neuron; GIN, GABAergic interneuron;
1346 HIPP, hippocampus; Iba1, ionized calcium-binding adapter molecule 1; Infl. EC, inflamed endothelial cells;
1347 LCMB, lecanemab; Mac, macrophages; Mg, microglia; Mono, monocytes; MT, mitochondrial; nAD, non-
1348 immunized Alzheimer's disease; nFeatures, number of features; Oligo, oligodendrocyte; OPC, oligodendrocyte
1349 precursor cell; *P*-adj, *P*-value adjusted; PCX, parietal cortex; PFC, probabilistic fold change; scRNAseq, single-
1350 cell fixed RNA sequencing; SEM, standard error of the mean; SMC, smooth muscle cell; SPP1, secreted
1351 phosphoprotein 1; SRG, stress-responsive glia; ST, spatial transcriptomics; TCX, temporal cortex; UMAP,
1352 uniform manifold approximation and projection; Vasc., vascular.

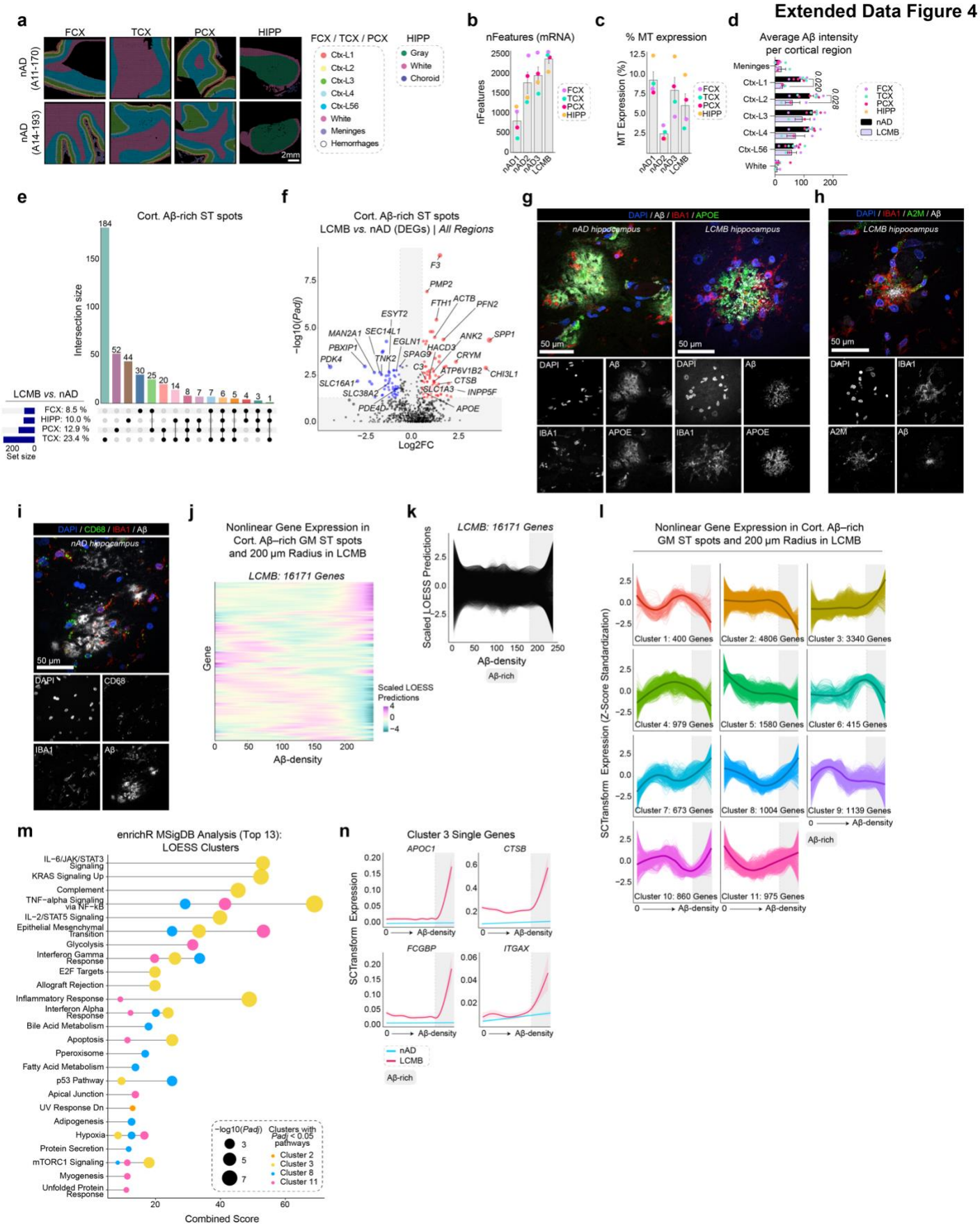

Extended Data Fig. 4: Microglia recruited to the Aβ niche upregulate *SPP1* following lecanemab treatment. **a,** Manual annotations of analyzed brain regions. **b**, Average number of features (genes) per spot

per manually annotated area per donor. **c**, Percentages of mitochondrial gene expression per spot averaged per manually annotated area per donor. **d**, Quantification of average Aβ intensity per cortical region per donor per group. **e**, UpSet plot indicating unique and shared DEGs in cortical Aβ-rich ST spots in FCX, TCX, PCX and HIPP for lecanemab vs. nAD. **f**, Volcano plot of DEGs from Aβ-rich gray matter ST spots (lecanemab vs. nAD) across all regions. **g**, Confocal images showing Iba1$^+$ myeloid cells surrounding Aβ deposits that colocalize with APOE in the hippocampus of the lecanemab-treated patient, with reduced Iba1$^+$ recruitment in the nAD control. **h**, Confocal images showing A2M$^+$Iba1$^+$ myeloid cells surrounding Aβ deposits in the hippocampus of the lecanemab-treated patient. **i**, Confocal images showing CD68$^+$Iba1$^+$ myeloid cells surrounding Aβ deposits in the hippocampus of the nAD control. **j**, LOESS heatmap showing non-linear gene expression patterns relative to Aβ density in lecanemab. **k**, LOESS non-linear trajectories relative to Aβ density in lecanemab. **l**, LOESS plots showing clusters of non-linear gene expression patterns relative to Aβ density in lecanemab. **m**, Pathway enrichment analysis of genes in non-linear expression clusters associated with Aβ density in lecanemab. **n**, LOESS plots of selected genes in LOESS cluster 3. A2M, alpha-2-macroglobulin; Aβ, amyloid-beta; AD, Alzheimer's disease; APO, apolipoprotein; APOC1, apolipoprotein C1; APOE, apolipoprotein E; CD68, cluster of differentiation 68; Cort., cortical; Ctx, cortex; CTSB, cathepsin B; DEGs, differentially expressed genes; FCGBP, Fc fragment of IgG binding protein; GM, gray matter; Iba1, ionized calcium-binding adapter molecule 1; ITGAX, integrin subunit alpha X; L, layer; LCMB, lecanemab; LOESS, locally estimated scatterplot smoothing; MSigDB, Molecular Signatures Database; MT, mitochondrial; nAD, non-immunized Alzheimer's disease; nFeatures, number of features; *P*-adj, *P*-value adjusted; SPP1, secreted phosphoprotein 1; ST, spatial transcriptomics.

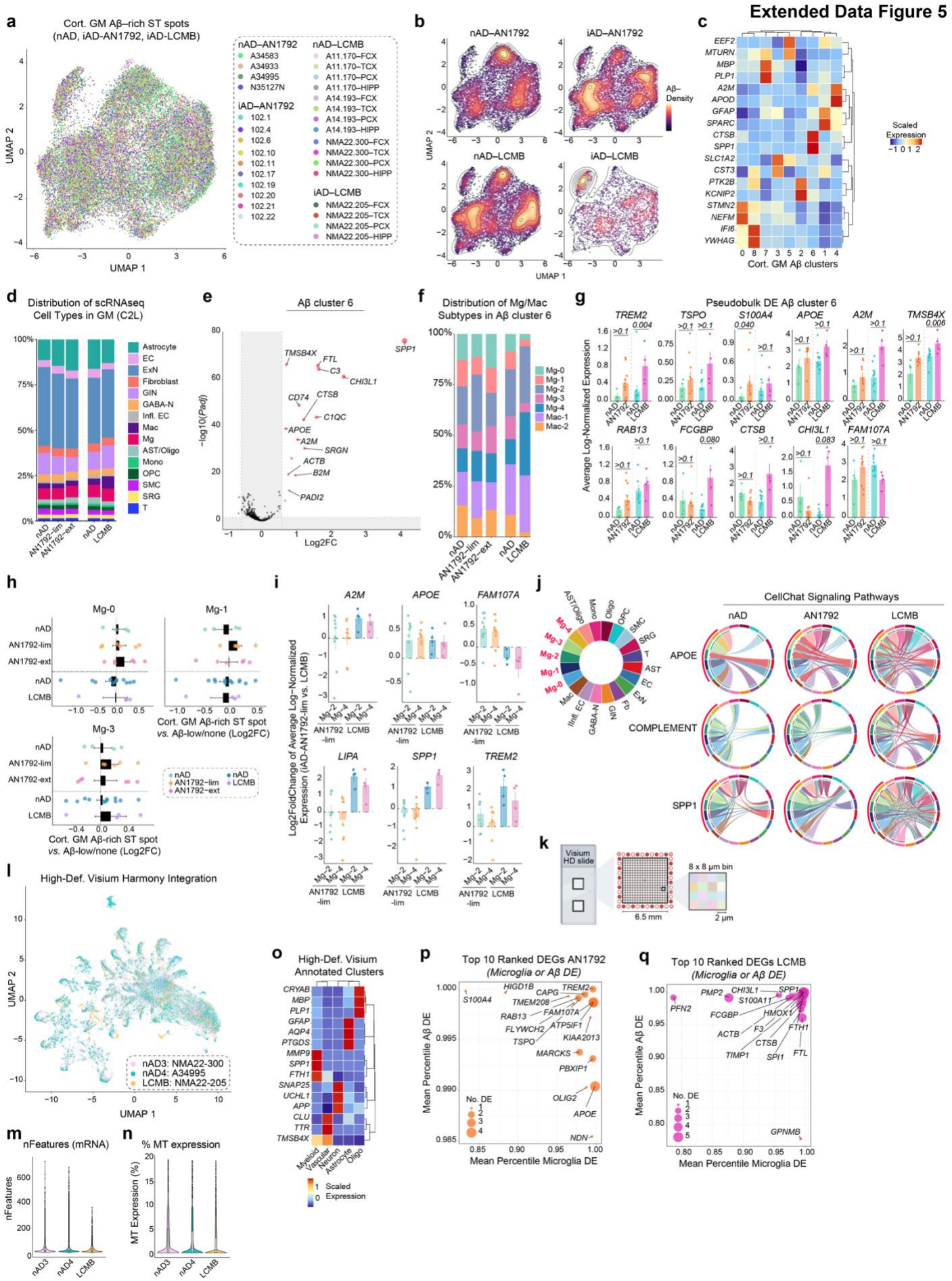
Extended Data Figure 5
a
Cort. GM Aβ–rich ST spots
(nAD, iAD-AN1792, iAD-LCMB)
UMAP 1
UMAP 2
nAD–AN1792
A34583
A34933
A34995
N35127N
iAD–AN1792
102.1
102.4
102.6
102.10
102.11
102.17
102.19
102.20
102.21
102.22
nAD–LCMB
A11.170–FCX
A11.170–TCX
A11.170–PCX
A11.170–HIPP
A14.193–FCX
A14.193–TCX
A14.193–PCX
A14.193–HIPP
NMA22.300–FCX
NMA22.300–TCX
NMA22.300–PCX
NMA22.300–HIPP
iAD–LCMB
NMA22.205–FCX
NMA22.205–TCX
NMA22.205–PCX
NMA22.205–HIPP
b
nAD–AN1792
iAD–AN1792
nAD–LCMB
iAD–LCMB
Aβ–Density
UMAP 1
UMAP 2
c
EEF2
MTURN
MBP
PLP1
A2M
APOD
GFAP
SPARC
CTSB
SPP1
SLC1A2
CST3
PTK2B
KCNIP2
STMN2
NEFM
IFI6
YWHAG
Scaled Expression
Cort. GM Aβ clusters
d
Distribution of scRNAseq Cell Types in GM (C2L)
Astrocyte
EC
ExN
Fibroblast
GIN
GABA-N
Infl. EC
Mac
Mg
AST/Oligo
Mono
OPC
SMC
SRG
T
nAD
AN1792–lim
AN1792–ext
nAD
LCMB
e
Aβ cluster 6
TMSB4X
FTL
C3
CHI3L1
SPP1
CD74
CTSB
C1QC
APOE
A2M
SRGN
ACTB
B2M
PADI2
−log10(Padj)
Log2FC
f
Distribution of Mg/Mac Subtypes in Aβ cluster 6
Mg-0
Mg-1
Mg-2
Mg-3
Mg-4
Mac-1
Mac-2
nAD
AN1792–lim
AN1792–ext
nAD
LCMB
g
Pseudobulk DE Aβ cluster 6
TREM2
TSPO
S100A4
APOE
A2M
TMSB4X
RAB13
FCGBP
CTSB
CHI3L1
FAM107A
Average Log-Normalized Expression
h
Mg-0
Mg-1
Mg-3
nAD
AN1792-lim
AN1792-ext
nAD
LCMB
Cort. GM Aβ-rich ST spot vs. Aβ-low/none (Log2FC)
i
A2M
APOE
FAM107A
LIPA
SPP1
TREM2
Log2FoldChange of Average Log−Normalized Expression (iAD-AN1792-lim vs. LCMB)
AN1792 -lim
LCMB
j
CellChat Signaling Pathways
nAD
AN1792
LCMB
APOE
COMPLEMENT
SPP1
k
Visium HD slide
6.5 mm
8 x 8 µm bin
2 µm
l
High-Def. Visium Harmony Integration
nAD3: NMA22-300
nAD4: A34995
LCMB: NMA22-205
UMAP 1
UMAP 2
m
nFeatures (mRNA)
nFeatures
nAD3
nAD4
LCMB
n
% MT expression
MT Expression (%)
nAD3
nAD4
LCMB
o
High-Def. Visium Annotated Clusters
CRYAB
MBP
PLP1
GFAP
AQP4
PTGDS
MMP9
SPP1
FTH1
SNAP25
UCHL1
APP
CLU
TTR
TMSB4X
Myeloid
Vascular
Neuron
Astrocyte
Oligo
Scaled Expression
p
Top 10 Ranked DEGs AN1792
(Microglia or Aβ DE)
HIGD1B
S100A4
CAPG
TREM2
TMEM208
RAB13
FAM107A
FLYWCH2
ATP5IF1
TSPO
KIAA2013
MARCKS
PBXIP1
OLIG2
APOE
NDN
No. DE
Mean Percentile Aβ DE
Mean Percentile Microglia DE
q
Top 10 Ranked DEGs LCMB
(Microglia or Aβ DE)
PMP2
CHI3L1
SPP1
S100A11
PFN2
FCGBP
HMOX1
FTH1
ACTB
F3
CTSB
TIMP1
SPI1
FTL
GPNMB
No. DE
Mean Percentile Aβ DE
Mean Percentile Microglia DE

1376

1377 **Extended Data Fig. 5: Transcriptomics reveals a shared microglial gene signature between active and**
1378 **passive Aβ immunization. a**, UMAP showing cortical Aβ-rich ST spots based on gene and protein expression,
1379 colored by brain region and donor. **b**, UMAP density plots for each group. **c**, Top two marker genes for each
1380 cortical Aβ-rich cluster. **d**, Bar plots showing cell2location predictions of scRNAseq cell types proportionally in
1381 the gray matter per group. **e**, Volcano plot showing DEGs distinguishing cortical Aβ-rich cluster 6 from all other
1382 cortical Aβ-rich clusters. **f**, Bar plots showing cell2location predictions of scRNAseq microglia and macrophage
1383 subtypes proportionally in Aβ-rich cluster 6 per group. **g**, Bar graphs showing pseudobulked *TREM2*, *TSPO*,
1384 *S100A4*, *APOE*, *A2M*, *TMSB4X*, *RAB13*, *FCGBP*, *CTSB*, *CHI3L1*, and *FAM107A* expression in Aβ-rich cluster
1385 6. Error bars indicate SEM. *P*-values are from DESeq2. **h**, Bar plots showing log2 fold-change in predicted
1386 abundance of deconvoluted scRNAseq microglia types in Aβ-rich ST spots versus the rest in AN1792, nAD,
1387 and the lecanemab case. **i**, Bar plots showing log2 fold-change in pseudobulked expression of *A2M*, *APOE*,
1388 *FAM107A*, *LIPA*, *SPP1*, and *TREM2* in Mg2-enriched and Mg4-enriched ST spots compared to the nAD control
1389 group for AN1792 and the lecanemab case. **j**, Chord plots showing inferred CellChat cell-cell communication
1390 of APOE, complement, and SPP1 signaling pathways among different scRNAseq cell types. The width of the
1391 chords reflects the strength of interaction or communication probability, with thicker chords indicating stronger
1392 signaling. **k**, Visium HD ST method. **l**, UMAP showing annotated binned nuclei from a high-definition Visium
1393 assay, colored by donor. **m**, Number of features (genes) per binned nuclei in high-definition ST data per donor.
1394 **n**, Percentage of mitochondrial genes per binned nuclei in high-definition ST data per donor. **o**, Top three marker
1395 genes for overarching cell types annotated in the high-definition ST data. **p-q**, Top 10 upregulated response
1396 DEGs in microglia or Aβ DE ranked by their average percentile in Aβ (Y-axis) and microglia (X-axis) DE: **o**, in
1397 AN1792; **r**, in lecanemab. A2M, alpha-2-macroglobulin; Aβ, amyloid-beta; AD, Alzheimer's disease; APOC1,
1398 apolipoprotein C1; APOE, apolipoprotein E; CD68, cluster of differentiation 68; Cort., cortical; Ctx, cortex;
1399 CTSB, cathepsin B; DEGs, differentially expressed genes; FCGBP, Fc fragment of IgG binding protein; GM,
1400 gray matter; HD, high-definition; Iba1, ionized calcium-binding adapter molecule 1; ITGAX, integrin subunit
1401 alpha X; L, layer; LCMB, lecanemab; LOESS, locally estimated scatterplot smoothing; MSigDB, Molecular
1402 Signatures Database; MT, mitochondrial; nAD, non-immunized Alzheimer's disease; nFeatures, number of
1403 features; *P*-adj, *P*-value adjusted; SPP1, secreted phosphoprotein 1; ST, spatial transcriptomics.
1404

References

1. Karran E, Hardy J. Antiamyloid therapy for Alzheimer's disease--are we on the right road? N Engl J Med. 2014;370(4):377-8. doi: 10.1056/NEJMe1313943. PubMed PMID: 24450897.
2. Holmes C, Boche D, Wilkinson D, Yadegarfar G, Hopkins V, Bayer A, Jones RW, Bullock R, Love S, Neal JW, Zotova E, Nicoll JA. Long-term effects of Abeta42 immunisation in Alzheimer's disease: follow-up of a randomised, placebo-controlled phase I trial. Lancet. 2008;372(9634):216-23. doi: 10.1016/S0140-6736(08)61075-2. PubMed PMID: 18640458.
3. Schenk D, Barbour R, Dunn W, Gordon G, Grajeda H, Guido T, Hu K, Huang J, Johnson-Wood K, Khan K, Kholodenko D, Lee M, Liao Z, Lieberburg I, Motter R, Mutter L, Soriano F, Shopp G, Vasquez N, Vandevert C, Walker S, Wogulis M, Yednock T, Games D, Seubert P. Immunization with amyloid-beta attenuates Alzheimer-disease-like pathology in the PDAPP mouse. Nature. 1999;400(6740):173-7. doi: 10.1038/22124. PubMed PMID: 10408445.
4. Games D, Bard F, Grajeda H, Guido T, Khan K, Soriano F, Vasquez N, Wehner N, Johnson-Wood K, Yednock T, Seubert P, Schenk D. Prevention and reduction of AD-type pathology in PDAPP mice immunized with A beta 1-42. Ann N Y Acad Sci. 2000;920:274-84. doi: 10.1111/j.1749-6632.2000.tb06936.x. PubMed PMID: 11193164.
5. Janus C, Pearson J, McLaurin J, Mathews PM, Jiang Y, Schmidt SD, Chishti MA, Horne P, Heslin D, French J, Mount HT, Nixon RA, Mercken M, Bergeron C, Fraser PE, St George-Hyslop P, Westaway D. A beta peptide immunization reduces behavioural impairment and plaques in a model of Alzheimer's disease. Nature. 2000;408(6815):979-82. doi: 10.1038/35050110. PubMed PMID: 11140685.
6. Morgan D, Diamond DM, Gottschall PE, Ugen KE, Dickey C, Hardy J, Duff K, Jantzen P, DiCarlo G, Wilcock D, Connor K, Hatcher J, Hope C, Gordon M, Arendash GW. A beta peptide vaccination prevents memory loss in an animal model of Alzheimer's disease. Nature. 2000;408(6815):982-5. doi: 10.1038/35050116. PubMed PMID: 11140686.
7. Orgogozo JM, Gilman S, Dartigues JF, Laurent B, Puel M, Kirby LC, Jouanny P, Dubois B, Eisner L, Flitman S, Michel BF, Boada M, Frank A, Hock C. Subacute meningoencephalitis in a subset of patients with AD after Abeta42 immunization. Neurology. 2003;61(1):46-54. doi: 10.1212/01.wnl.0000073623.84147.a8. PubMed PMID: 12847155.
8. Gilman S, Koller M, Black RS, Jenkins L, Griffith SG, Fox NC, Eisner L, Kirby L, Rovira MB, Forette F, Orgogozo JM, Team ANS. Clinical effects of Abeta immunization (AN1792) in patients with AD in an interrupted trial. Neurology. 2005;64(9):1553-62. doi: 10.1212/01.WNL.0000159740.16984.3C. PubMed PMID: 15883316.
9. Bayer AJ, Bullock R, Jones RW, Wilkinson D, Paterson KR, Jenkins L, Millais SB, Donoghue S. Evaluation of the safety and immunogenicity of synthetic Abeta42 (AN1792) in patients with AD. Neurology. 2005;64(1):94-101. doi: 10.1212/01.WNL.0000148604.77591.67. PubMed PMID: 15642910.
10. Nicoll JA, Wilkinson D, Holmes C, Steart P, Markham H, Weller RO. Neuropathology of human Alzheimer disease after immunization with amyloid-beta peptide: a case report. Nat Med. 2003;9(4):448-52. Epub 20030317. doi: 10.1038/nm840. PubMed PMID: 12640446.
11. Ferrer I, Boada Rovira M, Sanchez Guerra ML, Rey MJ, Costa-Jussa F. Neuropathology and pathogenesis of encephalitis following amyloid-beta immunization in Alzheimer's disease. Brain Pathol. 2004;14(1):11-20. doi: 10.1111/j.1750-3639.2004.tb00493.x. PubMed PMID: 14997933; PMCID: PMC8095815.
12. Nicoll JAR, Buckland GR, Harrison CH, Page A, Harris S, Love S, Neal JW, Holmes C, Boche D. Persistent neuropathological effects 14 years following amyloid-beta immunization in Alzheimer's disease. Brain. 2019;142(7):2113-26. doi: 10.1093/brain/awz142. PubMed PMID: 31157360; PMCID: PMC6598630.
13. Nicoll JA, Barton E, Boche D, Neal JW, Ferrer I, Thompson P, Vlachouli C, Wilkinson D, Bayer A, Games D, Seubert P, Schenk D, Holmes C. Abeta species removal after abeta42 immunization. J Neuropathol Exp Neurol. 2006;65(11):1040-8. doi: 10.1097/01.jnen.0000240466.10758.ce. PubMed PMID: 17086100.
14. Zotova E, Holmes C, Johnston D, Neal JW, Nicoll JA, Boche D. Microglial alterations in human Alzheimer's disease following Abeta42 immunization. Neuropathol Appl Neurobiol. 2011;37(5):513-24. doi: 10.1111/j.1365-2990.2010.01156.x. PubMed PMID: 21166690.
15. Englund H, Sehlin D, Johansson AS, Nilsson LN, Gellerfors P, Paulie S, Lannfelt L, Pettersson FE. Sensitive ELISA detection of amyloid-beta protofibrils in biological samples. J Neurochem. 2007;103(1):334-45. Epub 20070710. doi: 10.1111/j.1471-4159.2007.04759.x. PubMed PMID: 17623042.
16. van Dyck CH, Swanson CJ, Aisen P, Bateman RJ, Chen C, Gee M, Kanekiyo M, Li D, Reyderman L, Cohen S, Froelich L, Katayama S, Sabbagh M, Vellas B, Watson D, Dhadda S, Irizarry M, Kramer LD, Iwatsubo T. Lecanemab in Early Alzheimer's Disease. N Engl J Med. 2023;388(1):9-21. Epub 20221129. doi: 10.1056/NEJMoa2212948. PubMed PMID: 36449413.

17. Reish NJ, Jamshidi P, Stamm B, Flanagan ME, Sugg E, Tang M, Donohue KL, McCord M, Krumpelman C, Mesulam MM, Castellani R, Chou SH. Multiple Cerebral Hemorrhages in a Patient Receiving Lecanemab and Treated with t-PA for Stroke. N Engl J Med. 2023;388(5):478-9. Epub 20230104. doi: 10.1056/NEJMc2215148. PubMed PMID: 36599061; PMCID: PMC10228637.
18. Castellani RJ, Shanes ED, McCord M, Reish NJ, Flanagan ME, Mesulam MM, Jamshidi P. Neuropathology of Anti-Amyloid-beta Immunotherapy: A Case Report. J Alzheimers Dis. 2023;93(2):803-13. doi: 10.3233/JAD-221305. PubMed PMID: 37125554.
19. Corder EH, Saunders AM, Strittmatter WJ, Schmechel DE, Gaskell PC, Small GW, Roses AD, Haines JL, Pericak-Vance MA. Gene dose of apolipoprotein E type 4 allele and the risk of Alzheimer's disease in late onset families. Science. 1993;261(5123):921-3. doi: 10.1126/science.8346443. PubMed PMID: 8346443.
20. Strittmatter WJ, Saunders AM, Schmechel D, Pericak-Vance M, Enghild J, Salvesen GS, Roses AD. Apolipoprotein E: high-avidity binding to beta-amyloid and increased frequency of type 4 allele in late-onset familial Alzheimer disease. Proc Natl Acad Sci U S A. 1993;90(5):1977-81. doi: 10.1073/pnas.90.5.1977. PubMed PMID: 8446617; PMCID: PMC46003.
21. Butler AW, Ng MY, Hamshere ML, Forabosco P, Wroe R, Al-Chalabi A, Lewis CM, Powell JF. Meta-analysis of linkage studies for Alzheimer's disease--a web resource. Neurobiol Aging. 2009;30(7):1037-47. Epub 20090411. doi: 10.1016/j.neurobiolaging.2009.03.013. PubMed PMID: 19362756.
22. Guerreiro R, Wojtas A, Bras J, Carrasquillo M, Rogaeva E, Majounie E, Cruchaga C, Sassi C, Kauwe JS, Younkin S, Hazrati L, Collinge J, Pocock J, Lashley T, Williams J, Lambert JC, Amouyel P, Goate A, Rademakers R, Morgan K, Powell J, St George-Hyslop P, Singleton A, Hardy J, Alzheimer Genetic Analysis G. TREM2 variants in Alzheimer's disease. N Engl J Med. 2013;368(2):117-27. Epub 20121114. doi: 10.1056/NEJMoa1211851. PubMed PMID: 23150934; PMCID: PMC3631573.
23. Krasemann S, Madore C, Cialic R, Baufeld C, Calcagno N, El Fatimy R, Beckers L, O'Loughlin E, Xu Y, Fanek Z, Greco DJ, Smith ST, Tweet G, Humulock Z, Zrzavy T, Conde-Sanroman P, Gacias M, Weng Z, Chen H, Tjon E, Mazaheri F, Hartmann K, Madi A, Ulrich JD, Glatzel M, Worthmann A, Heeren J, Budnik B, Lemere C, Ikezu T, Heppner FL, Litvak V, Holtzman DM, Lassmann H, Weiner HL, Ochando J, Haass C, Butovsky O. The TREM2-APOE Pathway Drives the Transcriptional Phenotype of Dysfunctional Microglia in Neurodegenerative Diseases. Immunity. 2017;47(3):566-81 e9. doi: 10.1016/j.immuni.2017.08.008. PubMed PMID: 28930663; PMCID: PMC5719893.
24. Keren-Shaul H, Spinrad A, Weiner A, Matcovitch-Natan O, Dvir-Szternfeld R, Ulland TK, David E, Baruch K, Lara-Astaiso D, Toth B, Itzkovitz S, Colonna M, Schwartz M, Amit I. A Unique Microglia Type Associated with Restricting Development of Alzheimer's Disease. Cell. 2017;169(7):1276-90 e17. Epub 2017/06/13. doi: 10.1016/j.cell.2017.05.018. PubMed PMID: 28602351.
25. Gerrits E, Brouwer N, Kooistra SM, Woodbury ME, Vermeiren Y, Lambourne M, Mulder J, Kummer M, Moller T, Biber K, Dunnen W, De Deyn PP, Eggen BJL, Boddeke E. Distinct amyloid-beta and tau-associated microglia profiles in Alzheimer's disease. Acta Neuropathol. 2021;141(5):681-96. Epub 20210220. doi: 10.1007/s00401-021-02263-w. PubMed PMID: 33609158; PMCID: PMC8043951.
26. Nguyen AT, Wang K, Hu G, Wang X, Miao Z, Azevedo JA, Suh E, Van Deerlin VM, Choi D, Roeder K, Li M, Lee EB. APOE and TREM2 regulate amyloid-responsive microglia in Alzheimer's disease. Acta Neuropathol. 2020;140(4):477-93. Epub 20200825. doi: 10.1007/s00401-020-02200-3. PubMed PMID: 32840654; PMCID: PMC7520051.
27. Hartl FU, Bracher A, Hayer-Hartl M. Molecular chaperones in protein folding and proteostasis. Nature. 2011;475(7356):324-32. Epub 20110720. doi: 10.1038/nature10317. PubMed PMID: 21776078.
28. Murshid A, Prince TL, Lang B, Calderwood SK. Role of Heat Shock Factors in Stress-Induced Transcription. Methods Mol Biol. 2018;1709:23-34. doi: 10.1007/978-1-4939-7477-1_2. PubMed PMID: 29177648; PMCID: PMC7370818.
29. Tan C, Lu NN, Wang CK, Chen DY, Sun NH, Lyu H, Korbelin J, Shi WX, Fukunaga K, Lu YM, Han F. Endothelium-Derived Semaphorin 3G Regulates Hippocampal Synaptic Structure and Plasticity via Neuropilin-2/PlexinA4. Neuron. 2019;101(5):920-37 e13. Epub 20190123. doi: 10.1016/j.neuron.2018.12.036. PubMed PMID: 30685224.
30. Wang L, Pan Y, Chen D, Xiao Z, Xi Z, Xiao F, Wang X. Tetranectin is a potential biomarker in cerebrospinal fluid and serum of patients with epilepsy. Clin Chim Acta. 2010;411(7-8):581-3. Epub 20100125. doi: 10.1016/j.cca.2010.01.022. PubMed PMID: 20102706.
31. Wang ES, Sun Y, Guo JG, Gao X, Hu JW, Zhou L, Hu J, Jiang CC. Tetranectin and apolipoprotein A-I in cerebrospinal fluid as potential biomarkers for Parkinson's disease. Acta Neurol Scand. 2010;122(5):350-9. doi: 10.1111/j.1600-0404.2009.01318.x. PubMed PMID: 20085559.

32. Tanisawa K, Arai Y, Hirose N, Shimokata H, Yamada Y, Kawai H, Kojima M, Obuchi S, Hirano H, Yoshida H, Suzuki H, Fujiwara Y, Ihara K, Sugaya M, Arai T, Mori S, Sawabe M, Sato N, Muramatsu M, Higuchi M, Liu YW, Kong QP, Tanaka M. Exome-wide Association Study Identifies CLEC3B Missense Variant p.S106G as Being Associated With Extreme Longevity in East Asian Populations. J Gerontol A Biol Sci Med Sci. 2017;72(3):309-18. doi: 10.1093/gerona/glw074. PubMed PMID: 27154906; PMCID: PMC5861862.
33. Kolicheski A, Walton RL, Soto-Beasley AI, Heckman MG, Uitti RJ, Parfitt F, Graff-Radford MR, Wszolek ZK, Graff-Radford NR, Ross OA. CLEC3B p.S106G Mutant in a Caucasian Population of Successful Neurological Aging. J Gerontol A Biol Sci Med Sci. 2020;75(9):1618-23. doi: 10.1093/gerona/glz213. PubMed PMID: 31570938; PMCID: PMC7494029.
34. Serrano-Pozo A, Mielke ML, Muzitansky A, Gomez-Isla T, Growdon JH, Bacskai BJ, Betensky RA, Frosch MP, Hyman BT. Stable size distribution of amyloid plaques over the course of Alzheimer disease. J Neuropathol Exp Neurol. 2012;71(8):694-701. doi: 10.1097/NEN.0b013e31825e77de. PubMed PMID: 22805771; PMCID: PMC3407299.
35. Finak G, McDavid A, Yajima M, Deng J, Gersuk V, Shalek AK, Slichter CK, Miller HW, McElrath MJ, Prlic M, Linsley PS, Gottardo R. MAST: a flexible statistical framework for assessing transcriptional changes and characterizing heterogeneity in single-cell RNA sequencing data. Genome Biol. 2015;16:278. Epub 20151210. doi: 10.1186/s13059-015-0844-5. PubMed PMID: 26653891; PMCID: PMC4676162.
36. Hasegawa H, Nakai M, Tanimukai S, Taniguchi T, Terashima A, Kawamata T, Fukunaga K, Miyamoto E, Misaki K, Mukai H, Tanaka C. Microglial signaling by amyloid beta protein through mitogen-activated protein kinase mediating phosphorylation of MARCKS. Neuroreport. 2001;12(11):2567-71. doi: 10.1097/00001756-200108080-00055. PubMed PMID: 11496150.
37. Schmidt MV, Schulke JP, Liebl C, Stiess M, Avrabos C, Bock J, Wochnik GM, Davies HA, Zimmermann N, Scharf SH, Trumbach D, Wurst W, Zieglgansberger W, Turck C, Holsboer F, Stewart MG, Bradke F, Eder M, Muller MB, Rein T. Tumor suppressor down-regulated in renal cell carcinoma 1 (DRR1) is a stress-induced actin bundling factor that modulates synaptic efficacy and cognition. Proc Natl Acad Sci U S A. 2011;108(41):17213-8. Epub 20111003. doi: 10.1073/pnas.1103318108. PubMed PMID: 21969592; PMCID: PMC3193257.
38. Kleshchevnikov V, Shmatko A, Dann E, Aivazidis A, King HW, Li T, Elmentaite R, Lomakin A, Kedlian V, Gayoso A, Jain MS, Park JS, Ramona L, Tuck E, Arutyunyan A, Vento-Tormo R, Gerstung M, James L, Stegle O, Bayraktar OA. Cell2location maps fine-grained cell types in spatial transcriptomics. Nat Biotechnol. 2022;40(5):661-71. Epub 20220113. doi: 10.1038/s41587-021-01139-4. PubMed PMID: 35027729.
39. Fujita M, Gao Z, Zeng L, McCabe C, White CC, Ng B, Green GS, Rozenblatt-Rosen O, Phillips D, Amir-Zilberstein L, Lee H, Pearse RV, 2nd, Khan A, Vardarajan BN, Kiryluk K, Ye CJ, Klein HU, Wang G, Regev A, Habib N, Schneider JA, Wang Y, Young-Pearse T, Mostafavi S, Bennett DA, Menon V, De Jager PL. Cell subtype-specific effects of genetic variation in the Alzheimer's disease brain. Nat Genet. 2024. Epub 20240321. doi: 10.1038/s41588-024-01685-y. PubMed PMID: 38514782.
40. Green GS, Fujita M, Yang HS, Taga M, Cain A, McCabe C, Comandante-Lou N, White CC, Schmidtner AK, Zeng L, Sigalov A, Wang Y, Regev A, Klein HU, Menon V, Bennett DA, Habib N, De Jager PL. Cellular communities reveal trajectories of brain ageing and Alzheimer's disease. Nature. 2024;633(8030):634-45. Epub 20240828. doi: 10.1038/s41586-024-07871-6. PubMed PMID: 39198642.
41. Venegas C, Kumar S, Franklin BS, Dierkes T, Brinkschulte R, Tejera D, Vieira-Saecker A, Schwartz S, Santarelli F, Kummer MP, Griep A, Gelpi E, Beilharz M, Riedel D, Golenbock DT, Geyer M, Walter J, Latz E, Heneka MT. Microglia-derived ASC specks cross-seed amyloid-beta in Alzheimer's disease. Nature. 2017;552(7685):355-61. doi: 10.1038/nature25158. PubMed PMID: 29293211.
42. Planells-Ferrer L, Urresti J, Coccia E, Galenkamp KM, Calleja-Yague I, Lopez-Soriano J, Carriba P, Barneda-Zahonero B, Segura MF, Comella JX. Fas apoptosis inhibitory molecules: more than death-receptor antagonists in the nervous system. J Neurochem. 2016;139(1):11-21. Epub 20160803. doi: 10.1111/jnc.13729. PubMed PMID: 27385439.
43. Noda M, Takii K, Parajuli B, Kawanokuchi J, Sonobe Y, Takeuchi H, Mizuno T, Suzumura A. FGF-2 released from degenerating neurons exerts microglial-induced neuroprotection via FGFR3-ERK signaling pathway. J Neuroinflammation. 2014;11:76. Epub 20140416. doi: 10.1186/1742-2094-11-76. PubMed PMID: 24735639; PMCID: PMC4022102.
44. Haure-Mirande JV, Audrain M, Ehrlich ME, Gandy S. Microglial TYROBP/DAP12 in Alzheimer's disease: Transduction of physiological and pathological signals across TREM2. Mol Neurodegener. 2022;17(1):55. Epub 20220824. doi: 10.1186/s13024-022-00552-w. PubMed PMID: 36002854; PMCID: PMC9404585.

45. Maxeiner S, Shi N, Schalla C, Aydin G, Hoss M, Vogel S, Zenke M, Sechi AS. Crucial role for the LSP1-myosin1e bimolecular complex in the regulation of Fcgamma receptor-driven phagocytosis. Mol Biol Cell. 2015;26(9):1652-64. Epub 20150225. doi: 10.1091/mbc.E14-05-1005. PubMed PMID: 25717183; PMCID: PMC4436777.
46. Su F, Yang S, Wang H, Qiao Z, Zhao H, Qu Z. CIRBP Ameliorates Neuronal Amyloid Toxicity via Antioxidative and Antiapoptotic Pathways in Primary Cortical Neurons. Oxid Med Cell Longev. 2020;2020:2786139. Epub 20200226. doi: 10.1155/2020/2786139. PubMed PMID: 32184914; PMCID: PMC7063194.
47. Lujan DA, Ochoa JL, Hartley RS. Cold-inducible RNA binding protein in cancer and inflammation. Wiley Interdiscip Rev RNA. 2018;9(2). Epub 20180111. doi: 10.1002/wrna.1462. PubMed PMID: 29322631; PMCID: PMC5886743.
48. Sun N, Victor MB, Park YP, Xiong X, Scannail AN, Leary N, Prosper S, Viswanathan S, Luna X, Boix CA, James BT, Tanigawa Y, Galani K, Mathys H, Jiang X, Ng AP, Bennett DA, Tsai LH, Kellis M. Human microglial state dynamics in Alzheimer's disease progression. Cell. 2023;186(20):4386-403 e29. doi: 10.1016/j.cell.2023.08.037. PubMed PMID: 37774678; PMCID: PMC10644954.
49. Wyss-Coray T, Yan F, Lin AH, Lambris JD, Alexander JJ, Quigg RJ, Masliah E. Prominent neurodegeneration and increased plaque formation in complement-inhibited Alzheimer's mice. Proc Natl Acad Sci U S A. 2002;99(16):10837-42. Epub 20020715. doi: 10.1073/pnas.162350199. PubMed PMID: 12119423; PMCID: PMC125059.
50. Montine TJ, Phelps CH, Beach TG, Bigio EH, Cairns NJ, Dickson DW, Duyckaerts C, Frosch MP, Masliah E, Mirra SS, Nelson PT, Schneider JA, Thal DR, Trojanowski JQ, Vinters HV, Hyman BT, National Institute on A, Alzheimer's A. National Institute on Aging-Alzheimer's Association guidelines for the neuropathologic assessment of Alzheimer's disease: a practical approach. Acta Neuropathol. 2012;123(1):1-11. Epub 20111120. doi: 10.1007/s00401-011-0910-3. PubMed PMID: 22101365; PMCID: PMC3268003.
51. Arzt M, Deschamps J, Schmied C, Pietzsch T, Schmidt D, Tomancak P, Haase R, Jug F. LABKIT: Labeling and Segmentation Toolkit for Big Image Data. Frontiers in Computer Science. 2022;4. doi: 10.3389/fcomp.2022.777728.
52. Young MD, Behjati S. SoupX removes ambient RNA contamination from droplet-based single-cell RNA sequencing data. Gigascience. 2020;9(12). doi: 10.1093/gigascience/giaa151. PubMed PMID: 33367645; PMCID: PMC7763177.
53. McQuade A, Kang YJ, Hasselmann J, Jairaman A, Sotelo A, Coburn M, Shabestari SK, Chadarevian JP, Fote G, Tu CH, Danhash E, Silva J, Martinez E, Cotman C, Prieto GA, Thompson LM, Steffan JS, Smith I, Davtyan H, Cahalan M, Cho H, Blurton-Jones M. Gene expression and functional deficits underlie TREM2-knockout microglia responses in human models of Alzheimer's disease. Nat Commun. 2020;11(1):5370. Epub 20201023. doi: 10.1038/s41467-020-19227-5. PubMed PMID: 33097708; PMCID: PMC7584603.
54. Lawrence AR, Canzi A, Bridlance C, Olivie N, Lansonneur C, Catale C, Pizzamiglio L, Kloeckner B, Silvin A, Munro DAD, Fortoul A, Boido D, Zehani F, Cartonnet H, Viguier S, Oller G, Squarzoni P, Candat A, Helft J, Allet C, Watrin F, Manent JB, Paoletti P, Thieffry D, Cantini L, Pridans C, Priller J, Gelot A, Giacobini P, Ciobanu L, Ginhoux F, Thion MS, Lokmane L, Garel S. Microglia maintain structural integrity during fetal brain morphogenesis. Cell. 2024;187(4):962-80 e19. Epub 20240202. doi: 10.1016/j.cell.2024.01.012. PubMed PMID: 38309258; PMCID: PMC10869139.
55. Huang Y, Happonen KE, Burrola PG, O'Connor C, Hah N, Huang L, Nimmerjahn A, Lemke G. Microglia use TAM receptors to detect and engulf amyloid beta plaques. Nat Immunol. 2021;22(5):586-94. Epub 20210415. doi: 10.1038/s41590-021-00913-5. PubMed PMID: 33859405; PMCID: PMC8102389.
56. Jin S, Guerrero-Juarez CF, Zhang L, Chang I, Ramos R, Kuan CH, Myung P, Plikus MV, Nie Q. Inference and analysis of cell-cell communication using CellChat. Nat Commun. 2021;12(1):1088. Epub 20210217. doi: 10.1038/s41467-021-21246-9. PubMed PMID: 33597522; PMCID: PMC7889871.
57. Schmidt U, Weigert M, Broaddus C, Myers G, editors. Cell Detection with Star-Convex Polygons2018; Cham: Springer International Publishing.
58. Salloway S, Chalkias S, Barkhof F, Burkett P, Barakos J, Purcell D, Suhy J, Forrestal F, Tian Y, Umans K, Wang G, Singhal P, Budd Haeberlein S, Smirnakis K. Amyloid-Related Imaging Abnormalities in 2 Phase 3 Studies Evaluating Aducanumab in Patients With Early Alzheimer Disease. JAMA Neurol. 2022;79(1):13-21. doi: 10.1001/jamaneurol.2021.4161. PubMed PMID: 34807243; PMCID: PMC8609465.
59. Sims JR, Zimmer JA, Evans CD, Lu M, Ardayfio P, Sparks J, Wessels AM, Shcherbinin S, Wang H, Monkul Nery ES, Collins EC, Solomon P, Salloway S, Apostolova LG, Hansson O, Ritchie C, Brooks DA, Mintun M, Skovronsky DM, Investigators T-A. Donanemab in Early Symptomatic Alzheimer Disease: The TRAILBLAZER-ALZ 2 Randomized Clinical Trial. JAMA. 2023;330(6):512-27. doi: 10.1001/jama.2023.13239. PubMed PMID: 37459141; PMCID: PMC10352931.
60. Wang S, Mustafa M, Yuede CM, Salazar SV, Kong P, Long H, Ward M, Siddiqui O, Paul R, Gilfillan S, Ibrahim A, Rhinn H, Tassi I, Rosenthal A, Schwabe T, Colonna M. Anti-human TREM2 induces microglia proliferation and reduces

1612 pathology in an Alzheimer's disease model. J Exp Med. 2020;217(9). doi: 10.1084/jem.20200785. PubMed PMID:
1613 32579671; PMCID: PMC7478730.
1614 61. van Lengerich B, Zhan L, Xia D, Chan D, Joy D, Park JI, Tatarakis D, Calvert M, Hummel S, Lianoglou S, Pizzo ME, Prorok
1615 R, Thomsen E, Bartos LM, Beumers P, Capell A, Davis SS, de Weerd L, Dugas JC, Duque J, Earr T, Gadkar K, Giese T,
1616 Gill A, Gnorich J, Ha C, Kannuswamy M, Kim DJ, Kunte ST, Kunze LH, Lac D, Lechtenberg K, Leung AW, Liang CC, Lopez
1617 I, McQuade P, Modi A, Torres VO, Nguyen HN, Pesamaa I, Propson N, Reich M, Robles-Colmenares Y, Schlepckow K,
1618 Slemann L, Solanoy H, Suh JH, Thorne RG, Vieira C, Wind-Mark K, Xiong K, Zuchero YJY, Diaz D, Dennis MS, Huang F,
1619 Scearce-Levie K, Watts RJ, Haass C, Lewcock JW, Di Paolo G, Brendel M, Sanchez PE, Monroe KM. A TREM2-activating
1620 antibody with a blood-brain barrier transport vehicle enhances microglial metabolism in Alzheimer's disease models.
1621 Nat Neurosci. 2023;26(3):416-29. Epub 20230112. doi: 10.1038/s41593-022-01240-0. PubMed PMID: 36635496;
1622 PMCID: PMC9991924.
1623 62. Alzforum. AL002: Alzforum; 2023 [06 Nov 2023]. Available from: https://www.alzforum.org/therapeutics/al002.
1624 63. Baik SH, Kang S, Lee W, Choi H, Chung S, Kim JI, Mook-Jung I. A Breakdown in Metabolic Reprogramming Causes
1625 Microglia Dysfunction in Alzheimer's Disease. Cell Metab. 2019;30(3):493-507 e6. Epub 20190627. doi:
1626 10.1016/j.cmet.2019.06.005. PubMed PMID: 31257151.
1627 64. Solopova E, Romero-Fernandez W, Harmsen H, Ventura-Antunes L, Wang E, Shostak A, Maldonado J, Donahue MJ,
1628 Schultz D, Coyne TM, Charidimou A, Schrag M. Fatal iatrogenic cerebral beta-amyloid-related arteritis in a woman
1629 treated with lecanemab for Alzheimer's disease. Nat Commun. 2023;14(1):8220. Epub 20231212. doi:
1630 10.1038/s41467-023-43933-5. PubMed PMID: 38086820; PMCID: PMC10716177.
1631 65. Li Y, Macyczko JR, Liu CC, Bu G. ApoE4 reduction: An emerging and promising therapeutic strategy for Alzheimer's
1632 disease. Neurobiol Aging. 2022;115:20-8. Epub 20220322. doi: 10.1016/j.neurobiolaging.2022.03.011. PubMed
1633 PMID: 35453035; PMCID: PMC9133097.
1634 66. Pornnoppadol G, Bond LG, Lucas MJ, Zupancic JM, Kuo YH, Zhang B, Greineder CF, Tessier PM. Bispecific antibody
1635 shuttles targeting CD98hc mediate efficient and long-lived brain delivery of IgGs. Cell Chem Biol. 2024;31(2):361-72
1636 e8. Epub 20231026. doi: 10.1016/j.chembiol.2023.09.008. PubMed PMID: 37890480; PMCID: PMC10922565.
1637 67. Bennett DA, Buchman AS, Boyle PA, Barnes LL, Wilson RS, Schneider JA. Religious Orders Study and Rush Memory
1638 and Aging Project. J Alzheimers Dis. 2018;64(s1):S161-S89. doi: 10.3233/JAD-179939. PubMed PMID: 29865057;
1639 PMCID: PMC6380522.
1640 68. Kuleshov MV, Jones MR, Rouillard AD, Fernandez NF, Duan Q, Wang Z, Koplev S, Jenkins SL, Jagodnik KM, Lachmann
1641 A, McDermott MG, Monteiro CD, Gundersen GW, Ma'ayan A. Enrichr: a comprehensive gene set enrichment analysis
1642 web server 2016 update. Nucleic Acids Res. 2016;44(W1):W90-7. Epub 20160503. doi: 10.1093/nar/gkw377.
1643 PubMed PMID: 27141961; PMCID: PMC4987924.